Springer Theses
Recognizing Outstanding Ph.D. Research

Fei Gao

Multi-wave Electromagnetic-Acoustic Sensing and Imaging

Springer

Springer Theses

Recognizing Outstanding Ph.D. Research

Aims and Scope

The series "Springer Theses" brings together a selection of the very best Ph.D. theses from around the world and across the physical sciences. Nominated and endorsed by two recognized specialists, each published volume has been selected for its scientific excellence and the high impact of its contents for the pertinent field of research. For greater accessibility to non-specialists, the published versions include an extended introduction, as well as a foreword by the student's supervisor explaining the special relevance of the work for the field. As a whole, the series will provide a valuable resource both for newcomers to the research fields described, and for other scientists seeking detailed background information on special questions. Finally, it provides an accredited documentation of the valuable contributions made by today's younger generation of scientists.

Theses are accepted into the series by invited nomination only and must fulfill all of the following criteria

- They must be written in good English.
- The topic should fall within the confines of Chemistry, Physics, Earth Sciences, Engineering and related interdisciplinary fields such as Materials, Nanoscience, Chemical Engineering, Complex Systems and Biophysics.
- The work reported in the thesis must represent a significant scientific advance.
- If the thesis includes previously published material, permission to reproduce this must be gained from the respective copyright holder.
- They must have been examined and passed during the 12 months prior to nomination.
- Each thesis should include a foreword by the supervisor outlining the significance of its content.
- The theses should have a clearly defined structure including an introduction accessible to scientists not expert in that particular field.

More information about this series at http://www.springer.com/series/8790

Fei Gao

Multi-wave Electromagnetic-Acoustic Sensing and Imaging

Doctoral Thesis accepted by
Nanyang Technological University, Singapore

Springer

Author
Dr. Fei Gao
School of Electrical and Electronic Engineering
Nanyang Technological University
Singapore
Singapore

Supervisor
Prof. Yuanjin Zheng
Nanyang Technological University
Singapore
Singapore

ISSN 2190-5053 ISSN 2190-5061 (electronic)
Springer Theses
ISBN 978-981-10-3715-3 ISBN 978-981-10-3716-0 (eBook)
DOI 10.1007/978-981-10-3716-0

Library of Congress Control Number: 2016963645

Printed on acid-free paper

This Springer imprint is published by Springer Nature
The registered company is Springer Nature Singapore Pte Ltd.
The registered company address is: 152 Beach Road, #22-06/08 Gateway East, Singapore 189721, Singapore

Supervisor's Foreword

This thesis describes the scientific achievements of Dr. Fei Gao, which were made during his doctoral program in the School of Electrical and Electronic Engineering, Nanyang Technological University, Singapore. His research work covers a wide range of interdisciplinary topics about electromagnetic-acoustic (EM-acoustic) sensing and imaging mainly from three aspects: fundamental physics, critical biomedical applications, and sensing/imaging system designs.

From the fundamental physics perspective, Dr. Gao proposed several quite interesting EM-acoustic sensing and imaging methods, such as the equivalent circuit modeling of EM-acoustic effect; EM-acoustic phasoscopy; EM-acoustic resonance effect; EM-acoustic elastic oscillation; coherent EM-acoustic correlation and imaging; micro-Doppler EM-acoustic detection. These methods are highly potential to provide higher sensitivity, multi-contrast capability, and better imaging performance with lower distortion.

From the biomedical applications perspective, Dr. Gao also proposed useful techniques addressing some challenging biomedical applications, which include correlated microwave-acoustic imaging for breast cancer detection; single-wavelength oxygen saturation sensing for early stroke detection; photoacoustic-guided depth-resolved Raman spectroscopy for skin cancer detection; multistatic photoacoustic classification of tumor malignancy. All of the above methods are specifically designed to solve those critical applications, showing rich contrast, higher sensitivity and finer spatial resolution. Both phantom and ex vivo experiments have been performed in this Ph.D. thesis, and in vivo validations are in progress towards real clinical application scenarios.

From the sensing and imaging system design perspective, Dr. Gao developed several sensing/imaging prototypes that enables the above scientific explorations. These systems include photoacoustic microscopy for 3D imaging; multi-channel EM-acoustic imaging and miniaturized photoacoustic receiver in palm. Although these prototypes are still in their infant stage, Dr. Gao has also proposed methods that could further push these systems towards real products and commercialization,

such as replacing high-cost laser with portable laser diodes, integrating transmitting and data recording on single board.

Exploring at the boundary of interdisciplinary research domains is always most challenging but rewarding. Dr. Gao is willing to embrace multidisciplinary research fields and explore the interesting topics bridging physics, engineering and biomedicine. This excellent thesis is a collection of his research outcome that was previous published in various scientific journals and conference papers. Without a doubt, his research works open up new perspectives on tackling some interesting issues in the broad field of EM-acoustic sensing and imaging.

Singapore
October 2016

Prof. Yuanjin Zheng

Parts of this thesis have been published in the following journal articles:

1. **Fei Gao**, Qiwen Peng, Xiaohua Feng, Bo Gao, and Yuanjin Zheng, "Single-wavelength blood oxygen saturation sensing combining optical scattering and absorption", ***IEEE Sensors Journal***, 16, 1943–1948 (2016).
2. **Fei Gao**, Xiaohua Feng and Yuanjin Zheng, "Micro-Doppler photoacoustic effect and sensing by ultrasound radar", ***IEEE Journal of Selected Topics on Quantum Electronics,*** 22, 681806, 1–6 (2016).
3. **Fei Gao**, Xiaohua Feng, Yuanjin Zheng, "Photoacoustic elastic oscillation and characterization", ***Optics Express***, 23, 20617–20628 (2015).
4. **Fei Gao**, Xiaohua Feng, Yuanjin Zheng, "Photoacoustic Phasoscopy Super-Contrast Imaging", ***Applied Physics Letters***, 104, 213701 (2014).
5. **Fei Gao**, Xiaohua Feng, Yuanjin Zheng, "Coherent photoacoustic-ultrasound correlation and imaging", ***IEEE Transactions on Biomedical Engineering***, 61, 2507–2512 (2014).
6. **Fei Gao**, Qian Zheng, Yuanjin Zheng "Circuit Modeling and Analysis of Microwave Acoustic Interaction with Biological Tissues", ***Medical Physics***, 41, 053302 (2014).
7. **Fei Gao**, Yuanjin Zheng, Xiaohua Feng, and Claus-Dieter Ohl, "Thermoacoustic resonance effect and circuit modelling of biological tissue," ***Applied Physics Letters*** 102, 063702 (2013).
8. **Fei Gao**, Yuanjin Zheng, and Dongfang Wang, "Microwave-acoustic phasoscopy for tissue characterization," ***Applied Physics Letters*** 101, 043702 (2012).

Acknowledgements

Firstly, I would like to express my heartfelt thanks and appreciation to my supervisor, Prof. Yuanjin Zheng, for his unconditional help, constant guidance, and constructive comments throughout my research work. Most importantly, under his mentoring, I have gained valuable research and critical thinking skills.

I would like to thank Prof. Claus-Diter Ohl (SPMS, NTU), Prof. Quan Liu (SCBE, NTU), Prof. Yufeng Zhou (MAE, NTU), Prof. Yanli Zhao (SPMS, NTU), Dr. Linyi Bai (SPMS, NTU), Dr. Bo Gao (Sichuan University), Dr. Dongfang Wang (Xi'an University of Technology), Dr. Leong (NUHS), Mr. Isa (Ngee Ann Poly) for their valuable advice and comments on my research work.

Many thanks to our group members: Dr. Xiaohua Feng, Dr. Qiwen Peng, Dr. Gaoming Li, Dr. Ran Ding, Mr. Ganesh, Mr. Rahul, Mr. Supeng Liu, Ms. Yao Zhu, Mr. Siyu Liu, Ms. Ruochong Zhang, and lab staff Mr. Vincent, Ms. Gek Eng Tan, and all my good friends: Yong Wang, Fanyi Meng, Shanshan Xu, Tianwei Deng, Yihu Li, Chang Liang and so on, and all the technician/staff in the VIRTUS IC design center, for their kind assistance, cooperation and services. It is my great pleasure to know all these fine people during my studies at Nanyang Technological University.

My special thanks go to my family and my wife Lisha, who has been a constant source of unconditional love and support throughout my Ph.D. study.

Last but not least, I would also like to thank Nanyang Technological University for providing me the scholarship and NMRC for the research funding.

Contents

List of Figures

List of Tables

Summary

Single-wave electromagnetic (EM) sensing and imaging has attracted tremendous research interest for many real-life applications, ranging from high-frequency optical imaging (e.g. confocal microscopy, coherence optical tomography), microwave imaging (e.g. radar, THz imaging), to low-frequency magnetic imaging (e.g. MRI). On the other hand, single-wave acoustic sensing and imaging have also found many applications in sonar system, medical ultrasound imaging, non-destructive testing (NDT), etc. Unfortunately, these single-wave sensing and imaging techniques suffer from either low imaging contrast or spatial resolution due to the nature of single-wave diffusion and/or diffraction.

In recent decades, multi-wave EM-acoustic sensing and imaging have shown significant potential in biomedical applications by "listening to the sound of EM wave" based on photoacoustic/thermoacoustic effect, i.e. acoustic generation due to transient EM energy absorption and thermoelastic expansion. Bridging the beauty of the two worlds, multi-wave EM-acoustic imaging could break through the diffusion and diffraction limit of EM wave by detecting the induced acoustic wave with 1000 times less scattering, enhancing the spatial resolution with deep penetration and simultaneously maintaining the high contrast/specificity of EM sensing and imaging. To further advance the multi-wave EM-acoustic sensing and imaging techniques, this Ph.D. thesis comprehensively investigates several novel aspects of this area, covering fundamental methods, biomedical applications and system implementations.

In the first part of the thesis, several novel aspects of EM-acoustic fundamental methods are proposed and discussed in detail. In Sect. 2.1, it introduces an electrical circuit modeling approach of microwave-acoustic interaction with biological tissue for quantitative analysis and bio-circuit co-simulation. In Sect. 2.2, a new concept "phasoscopy" is introduced correlating EM scattering and absorption to achieve super sensitivity and contrast for biological tissue characterization and imaging. In Sects. 2.3 and 2.4, EM-acoustic resonance and oscillation effect are observed, modeled and utilized for tissue characterization and imaging, fusing optical absorption and mechanical resonance. In Sect. 2.5, the coherent correlation between EM-acoustic and ultrasound is explored for super-contrast imaging. In Sect. 2.6,

the micro-Doppler EM-acoustic effect is predicted and observed experimentally, which could potentially achieve sensitive EM-acoustic detection.

In the second part of the thesis, several interesting applications of the EM-acoustic sensing and imaging are introduced with innovative approaches. In Sect. 3.1, a correlated microwave-acoustic imaging approach is proposed by fusing scattered microwave and thermoacoustic image to deliver higher image contrast for early-stage breast cancer detection, which is proved with numerical simulation results. In Sect. 3.2, a novel single-wavelength approach is proposed to detect the blood oxygen saturation (SO_2), where both scattered optical wave and photoacoustic wave are collected and correlated. Phantom studies are performed to validate its feasibility. In Sect. 3.3, a photoacoustic-guided depth-resolved Raman spectroscopy approach is proposed for skin cancer diagnosis, which is experimentally validated on multi-layer phantom. In Sect. 3.4, a multistatic photoacoustic classification approach is proposed to characterize malignant and benign tumors, which is challenging for conventional photoacoustic tomography for deep tissue imaging.

In the third part of the thesis, several EM-acoustic systems for biomedical sensing and imaging are introduced. In Sect. 4.1, a photoacoustic microscopy system is designed and implemented for 3D imaging, which has been proved on phantom study and will be used for ex vivo and in vivo experiments. In Sect. 4.2, a multi-channel microwave-acoustic imaging system is designed, together with a multi-channel photoacoustic receiver system including a linear-array ultrasound probe and multi-channel data acquisition card. In Sect. 4.3, a miniaturized photoacoustic receiver is designed, prototyped and demonstrated with dramatically reduced compact size in palm for photoacoustic sensing applications.

In summary, this thesis comprehensively investigates the fundamental physics, biomedical applications and system implementations of the emerging EM-acoustic sensing and imaging technique. It introduces some interesting concepts, which could potentially solve some important biomedical problems and inspire in-depth thought to develop an advanced multi-wave EM-acoustic imaging system.

Chapter 1
Multi-wave EM-Acoustic Introduction

In this chapter, a brief introduction of the conventional single-wave imaging and emerging multi-wave imaging modalities is provided to show the state-of-art in Sect. 1.1. Single-wave imaging modalities include optical imaging, microwave imaging and magnetic imaging spreading the whole EM spectrum, as well as ultrasound imaging, elastography, etc. Emerging multi-wave imaging modalities include laser-induced photoacoustic imaging, microwave-induced thermoacoustic imaging, magnetically mediated thermoacoustic imaging, etc. Then the research motivation and major contribution of this thesis is introduced in Sect. 1.2.

1.1 Background

In this section, background about both single-wave and multi-wave biomedical imaging modalities is briefly introduced to give an overview of this research area.

1.1.1 Single-Wave Sensing and Imaging

Single-wave sensing and imaging modalities refer to the imaging techniques that utilize only one kind of physical wave, mainly including EM wave (Gamma-ray PET, X-ray CT, optical imaging, microwave radar imaging, magnetic resonance imaging) and acoustic wave (B-mode ultrasound, Doppler color ultrasound, elastography). Single-wave imaging modalities have dominated the biomedical diagnostic research and industry for more than one century since first X-ray picture taken in 1895. Although tremendous progress has been achieved, there are still some fundamental limits about the single-wave imaging modalities, e.g. wave diffraction and diffusion. Here several major single-wave imaging modalities are introduced below to show their advantages and disadvantages.

F. Gao, *Multi-wave Electromagnetic-Acoustic Sensing and Imaging*,
Springer Theses, DOI 10.1007/978-981-10-3716-0_1

1.1.1.1 Optical Imaging

Optical imaging refers to the imaging using light ranging from ultraviolet, visible to infrared light [1]. Optical imaging could provide high spatial resolution for surface investigation due to the tight optical focusing limited by optical diffraction, and high specificity due to distinct optical absorption spectra of different types of molecules. Unfortunately, accurate optical focusing inside deep scattering medium (e.g. biological tissues) is a long-standing challenge due to the optical diffusion limit, limiting its major applications to surface investigation (<1 mm depth). Although some emerging optical imaging modalities (e.g. multi-photon optical microscopy, optical coherence tomography, diffusion optical tomography) are pushing the image depth to cm range, they are still suffering high complexity, high cost and degraded spatial resolution in deep tissue.

1.1.1.2 Microwave Imaging

Microwave imaging originates from the military radar system, which is based on transmitting short pulse (∼ns) microwave signal and receiving the reflected microwave signal from the object. Its potential for biomedical imaging applications have been explored in recent years majorly for breast cancer detection [2]. Microwave imaging is probing the dielectric properties of the biological tissues in several hundreds of MHz to several GHz spectrum range, within which the cancerous tumor exhibits significantly different permittivity and conductivity (>5 times) than normal tissues [3]. Although microwave could penetrate much deeper than light, its longer wavelength limits its spatial resolution to mm range even after applying advanced beamforming techniques.

1.1.1.3 Ultrasound Imaging

Ultrasound imaging is based on ultrasound wave with hundreds of kHz to several MHz frequency [4], rather than EM wave in optical and microwave imaging. B-mode ultrasound imaging explores the acoustic impedance mismatch by transmitting pulse ultrasound signal and receiving pulse-echo reflected signal. High resolution image in deep tissue could be acquired due to the much less (1000 times) acoustic scattering compared with optical imaging. However, ultrasound imaging suffers low image contrast and no molecular specificity, which limits its applications to anatomical imaging with no functional information.

1.1.1.4 Other Kinds of Single-Wave Imaging

Beyond the three kinds of single-wave imaging modalities introduced above, there are some other types of imaging modalities, such as magnetic resonance imaging

(MRI) that transmits and receives alternating magnetic field, elastography that images the stiffness of the biological tissues, and positron emission tomography (PET) that detects pairs of gamma rays. All these single-wave imaging modalities are exploring the property of one type of physical wave, which cannot meet the stringent requirements (high spatial resolution, high image contrast, deep penetration, molecular specificity, real time, low cost, etc.) in modern biomedical imaging applications.

1.1.2 Multi-wave Sensing and Imaging

Multi-wave sensing and imaging modalities refer to the imaging techniques that utilize two or more different types of physical waves, typically EM wave and acoustic wave, to achieve superior imaging performance by combining the merits of them. Multi-wave imaging modalities, mainly including photoacoustic imaging, microwave/magnetic-induced thermoacoustic imaging, ultrasound-optic tomography and so on, have attracted dramatically increasing research interest in recent years. By taking advantages of the high specificity of EM wave and high spatial resolution of acoustic wave in depth, these multi-wave imaging modalities have been explored in many promising biomedical applications to provide both anatomical and functional information in deep tissue. Here several typical multi-wave imaging modalities will be introduced below.

1.1.2.1 Light-Induced Thermoacoustic Imaging (Photoacoustic Imaging)

Light-induced thermoacoustic imaging, usually called photoacoustic imaging, is a emerging multi-wave imaging modality based on photoacoustic effect [5]. Pulsed (or intensity modulated) laser light in visible and near infrared range is guided to illuminate on the sample, leading to optical absorption, heating and thermoelastic expansion, which launch the acoustic wave propagating outwards. Ultrasound transducer (or transducer array) is employed to receive the photoacoustic signal for image reconstruction. Based on different system configurations and applications, photoacoustic imaging could be mainly classified into photoacoustic microscopy (PAM), photoacoustic computed tomography (PAT), and photoacoustic endoscopy (PAE). Due to the conversion from light to sound, photoacoustic imaging is able to break through the optical diffusion limit to reach several cm imaging depth, maintaining high spatial resolution of ultrasound wave. Significant research progress on photoacoustic imaging has been achieved, covering fundamental methodology, engineering development, and biomedical applications [6–25].

1.1.2.2 Microwave-Induced Thermoacoustic Imaging

Similar with photoacoustic imaging mentioned above, microwave-induced thermoacoustic imaging (MITAI) is based on pulsed (or intensity modulated) microwave illumination in the range of hundreds of MHz to several GHz. After absorption of the microwave energy, thermoacoustic wave is induced and detected by ultrasound transducer for image reconstruction. MITAI integrates the high image contrast of dielectric properties based on microwave absorption and high spatial resolution based on acoustic detection, showing promise in some biomedical applications, such as breast cancer and brain imaging [26–33].

1.1.2.3 Magnetically Medicated Thermoacoustic Imaging

Inspired by the laser and microwave induced thermoacoustic imaging above, it is expected that thermoacoustic signal should also be induced by pulsed magnetic illumination, which is firstly reported by Feng et al. of our group in 2013 [34]. By pumping large AC current into a resonance coil, AC magnetic field is induced around the coil, which could further induce electrical field in a conductor (e.g. a metal strip). Then joule heating inside the conductor could generate acoustic wave based on thermoelastic expansion. Magnetically mediated thermoacoustic imaging could provide deeper penetration than laser and microwave induction, showing the potential for human whole-body imaging like MRI.

1.1.2.4 Other Kinds of Multi-wave Imaging

Except the imaging modalities mentioned above, there are some other multi-wave imaging modalities, such as Ultrasound-optic tomography (UOT) based on ultrasound modulation of light scattering, magnetoacoustic tomography with magnetic induction (MATMI) based on Lorenz force generated acoustic wave under permanent magnet, magnetic resonance elastography (MRE) based on MRI tracking of mechanical shear wave, and so on. All these multi-wave imaging techniques are combining the merits of two kinds of physical wave to achieve better image performance.

1.2 Research Motivation

Although there has been dramatic research progress in the multi-wave imaging domain, some limitations are still to be solved to further push these emerging techniques for real clinical applications:

The first limitation of the existing multi-wave imaging is: they are only exploring single image contrast, e.g. photoacoustic imaging for optical absorption contrast,

microwave-induced thermoacoustic imaging for dielectric contrast, magnetic resonance elastography for elasticity contrast. It is highly desired to develop a multi-wave multi-contrast imaging techniques to further improve the imaging specificity and reliability.

The second limitation is the sensitivity of multi-wave imaging modalities. Due to the low conversion efficiency from EM wave to acoustic wave, the acoustic signal is suffering low signal-to-noise ratio (SNR), which requires low-noise detection and data averaging. Improvement on the system sensitivity is highly demanded to develop a commercial imaging device.

The third limitation is the complexity and cost of the existing multi-wave imaging modalities. To enable a portable and low cost multi-wave imaging device, a compact system design is required utilizing advanced integration technology.

1.3 Major Contribution

To overcome these limitations, this thesis conducts a comprehensive study on three aspects: fundamental methods, biomedical applications and system developments:

Fundamental methods: In Sect. 2.1, it introduces an electrical circuit modeling approach of microwave-acoustic interaction with biological tissue for quantitative analysis and bio-circuit co-simulation. In Sect. 2.2, a new concept "phasoscopy" is introduced correlating EM scattering and absorption to achieve super sensitivity and contrast for biological tissue characterization and imaging. In Sects. 2.3 and 2.4, EM-acoustic resonance and oscillation effect are observed, modelled and utilized for tissue characterization and imaging, fusing optical absorption and mechanical resonance. In Sect. 2.5, the coherent correlation between EM-acoustic and ultrasound is explored for super-contrast imaging. In Sect. 2.6, the micro-Doppler EM-acoustic effect is predicted and observed experimentally, which could potentially achieve sensitive EM-Acoustic detection.

Biomedical applications: In Sect. 3.1, a correlated microwave-acoustic imaging approach is proposed by fusing scattered microwave and thermoacoustic image to deliver higher image contrast for early-stage breast cancer detection, which is proved with numerical simulation results. In Sect. 3.2, a novel single-wavelength approach is proposed to detect the blood oxygen saturation (SO_2), where both scattered optical wave and photoacoustic wave are collected and correlated. Phantom studies are performed to validate its feasibility. In Sect. 3.3, a photoacoustic-guided depth-resolved Raman spectroscopy approach is proposed for skin cancer diagnosis, which is experimentally validated on multi-layer phantom. In Sect. 3.4, a multistatic photoacoustic classification approach is proposed to characterize malignant and benign tumors, which is challenging for conventional photoacoustic tomography for deep tissue imaging.

System development: In Sect. 4.1, a photoacoustic microscopy system is designed and implemented for 3D imaging, which has been proved on phantom study and will be used for ex vivo and in vivo experiments. In Sect. 4.2, a

multi-channel microwave-acoustic imaging system is designed, together with a multi-channel photoacoustic receiver system including a linear-array ultrasound probe and multi-channel data acquisition card. In Sect. 4.3, a miniaturized photoacoustic receiver is designed, prototyped and demonstrated with dramatically reduced compact size in palm for photoacoustic sensing applications.

References

1. Wang LV, Wu HI (2007) Biomedical optics: principles and imaging. Wiley
2. Fear EC, Meaney PM, Stuchly MA (2003) Microwaves for breast cancer detection? Potentials, IEEE 22:12–18
3. Lazebnik M, Popovic D, McCartney L, Watkins CB, Lindstrom MJ, Harter J et al (2007) A large-scale study of the ultrawideband microwave dielectric properties of normal, benign and malignant breast tissues obtained from cancer surgeries. Phys Med Biol 52:6093–6115
4. Fatemi M, Greenleaf JF (1998) Ultrasound-stimulated vibro-acoustic spectrography. Science 280:82–85
5. Tam AC (1986) Applications of photoacoustic sensing techniques. Rev Mod Phys 58:381–431
6. Zhang HF, Maslov K, Sivaramakrishnan M, Stoica G, Wang LHV (2007) Imaging of hemoglobin oxygen saturation variations in single vessels in vivo using photoacoustic microscopy. Appl Phys Lett 90
7. Kim C, Favazza C, Wang LHV (2010) In vivo photoacoustic tomography of chemicals: high-resolution functional and molecular optical imaging at new depths. Chem Rev 110:2756–2782
8. Ntziachristos V, Razansky D (2010) Molecular imaging by means of multispectral optoacoustic tomography (MSOT). Chem Rev 110:2783–2794
9. Wang XD, Pang YJ, Ku G, Xie XY, Stoica G, Wang LHV (2003) Noninvasive laser-induced photoacoustic tomography for structural and functional in vivo imaging of the brain. Nat Biotechnol 21:803–806
10. Zhang HF, Maslov K, Stoica G, Wang LHV (2006) Functional photoacoustic microscopy for high-resolution and noninvasive in vivo imaging. Nat Biotechnol 24:848–851
11. Wilson K, Homan K, Emelianov S (2012) Biomedical photoacoustics beyond thermal expansion using triggered nanodroplet vaporization for contrast-enhanced imaging. Nat Commun 3
12. Kircher MF, de la Zerda A, Jokerst JV, Zavaleta CL, Kempen PJ, Mittra E et al (2012) A brain tumor molecular imaging strategy using a new triple-modality MRI-photoacoustic-Raman nanoparticle. Nat Med 18:829-U235
13. Yang JM, Favazza C, Chen RM, Yao JJ, Cai X, Maslov K et al (2012) Simultaneous functional photoacoustic and ultrasonic endoscopy of internal organs in vivo. Nat Med 18:1297
14. De La Zerda A, Zavaleta C, Keren S, Vaithilingam S, Bodapati S, Liu Z et al (2008) Carbon nanotubes as photoacoustic molecular imaging agents in living mice. Nat Nanotechnol 3:557–562
15. Galanzha EI, Shashkov EV, Kelly T, Kim JW, Yang L, Zharov VP (2009) In vivo magnetic enrichment and multiplex photoacoustic detection of circulating tumour cells. Nat Nanotechnol 4:855–860
16. Graham-Rowe D (2009) Sounding out photons. Nat Photonics 3:123–125
17. Razansky D, Distel M, Vinegoni C, Ma R, Perrimon N, Koster RW et al (2009) Multispectral opto-acoustic tomography of deep-seated fluorescent proteins in vivo. Nat Photonics 3:412–417

18. Wang LV (2009) Multiscale photoacoustic microscopy and computed tomography. Nat Photonics 3:503–509
19. Zhang HF, Maslov K, Wang LHV (2007) In vivo imaging of subcutaneous structures using functional photoacoustic microscopy. Nat Protoc 2:797–804
20. Hu S, Maslov K, Wang LV (2011) Second-generation optical-resolution photoacoustic microscopy with improved sensitivity and speed. Opt Lett 36:1134–1136
21. Li CH, Wang LHV (2009) Photoacoustic tomography and sensing in biomedicine. Phys Med Biol 54:R59–R97
22. Emelianov SY, Li PC, O'donnell M (2009) Photoacoustics for molecular imaging and therapy. Physics Today 62:34–39
23. Wang LHV, Hu S (2012) Photoacoustic tomography. In vivo imaging from organelles to organs. Science 335:1458–1462
24. Xiang LZ, Wang B, Ji LJ, Jiang HB (2013) 4-D photoacoustic tomography. Scientific Reports 3
25. Mallidi S, Luke GP, Emelianov S (2011) Photoacoustic imaging in cancer detection, diagnosis, and treatment guidance. Trends Biotechnol 29:213–221
26. Kruger RA, Kopecky KK, Aisen AM, Reinecke DR, Kruger GA, Kiser WL (1999) Thermoacoustic CT with radio waves: a medical imaging paradigm. Radiology 211:275–278
27. Minghua X, Wang LV (2002) Time-domain reconstruction for thermoacoustic tomography in a spherical geometry. IEEE Trans Med Imag 21:814–822
28. Yuan X, Dazi F, Wang LV (2002) Exact frequency-domain reconstruction for thermoacoustic tomography. I. Planar geometry. IEEE Trans Med Imag 21:823–828
29. Yuan X, Minghua X, Wang LV (2002) Exact frequency-domain reconstruction for thermoacoustic tomography. II. Cylindrical geometry. IEEE Trans Med Imag 21:829–833
30. Minghua X, Yuan X, Wang LV (2003) Time-domain reconstruction algorithms and numerical simulations for thermoacoustic tomography in various geometries. IEEE Trans Biomed Eng 50:1086–1099
31. Yuan X, Wang LV (2006) Rhesus monkey brain imaging through intact skull with thermoacoustic tomography. IEEE Trans Ultrasonics, Ferroelectrics Frequency Control 53:542–548
32. Yao X, Bin G, Jian L, Geng K, Wang LV (2008) Adaptive and Robust Methods of Reconstruction (ARMOR) for thermoacoustic tomography. IEEE Trans Biomed Eng 55:2741–2752
33. Guangran Z, Popovic M, Qianqian F (2009) Microwave-Induced thermoacoustics: assisting microwave tomography. IEEE Trans Magn 45:1654–1657
34. Feng XH, Gao F, Zheng YJ (2013) Magnetically mediated thermoacoustic imaging toward deeper penetration. Appl Phys Lett 103

Chapter 2
Multi-wave EM-Acoustic Methods

In this chapter, several novel aspects of EM-Acoustic fundamental methodologies research are proposed and discussed in detail. In Sect. 2.1, it introduces a circuit modeling approach of microwave-acoustic interaction with biological tissue for quantitative analysis and bio-circuit co-simulation. In Sect. 2.2, a new concept "phasoscopy" is introduced correlating EM scattering and absorption to achieve super sensitivity and contrast for biological tissue characterization and imaging. In Sects. 2.3 and 2.4, EM-acoustic resonance and oscillation effect are observed, modelled and utilized for tissue characterization and imaging, fusing optical absorption and mechanical resonance. In Sect. 2.5, the coherent correlation between EM-acoustic and ultrasound is explored for super-contrast imaging. In Sect. 2.6, the micro-Doppler EM-acoustic effect is predicted and observed experimentally, which could potentially achieve sensitive EM-Acoustic detection.

2.1 Circuit Modeling of EM-Acoustic Interaction

In this section, an electrical circuit modeling of the EM-acoustic interaction with biological tissue will be introduced by modeling tissue as a 2-port network described by pseudo S-parameters. Take microwave-acoustic interaction as an example, the model includes microwave scattering, microwave absorption and thermoacoustic expansion at each point. By building the 2D circuit network incorporating acoustic scatterer and channel model, it enables the 2D simulation of microwave-acoustic interaction with tissue for image reconstruction. Preliminary simulation and experimental results are provided to prove the feasibility of the proposed circuit model. The results of this section has been published on *Medical Physics* [1].

F. Gao, *Multi-wave Electromagnetic-Acoustic Sensing and Imaging*,
Springer Theses, DOI 10.1007/978-981-10-3716-0_2

2.1.1 Motivation

For both microwave imaging (such as microwave tomography and confocal microwave imaging) and microwave-induced thermoacoustic imaging, microwave signal is transmitted into biological tissues and interacting with the tumor. The scattered microwave signal is received by the antenna placed around the biological tissues for microwave imaging, and the acoustic signal induced by microwave absorption and thermal expansion is detected by ultrasound transducers for thermoacoustic imaging, as shown in Fig. 2.1. Finite difference time domain (FDTD) analysis is widely used to solve the Maxwell's equation for simulating EM and acoustic propagation and interaction in the biological tissues when studying these microwave acoustic imaging modalities, providing accurate wideband and time-domain simulation for beamforming and image reconstruction. However, FDTD simulation is time-consuming when simulating long time duration, and separated simulation is needed for EM and acoustic field in microwave-induced thermoacoustic imaging research. In addition, as a numerical simulation method, it is not capable of evaluating the imaging system performance quantitatively. To our best knowledge, there is no uniform model and simulation approach integrating the numerical simulation for microwave acoustic bio-effect with circuit simulation for microwave acoustic imaging hardware development.

2.1.2 Circuit Model of Microwave-Acoustic Interaction with Tumor Tissue

For microwave acoustic imaging modality, a microwave signal is transmitted into biological tissues from outside and undergoes the following four biophysical interactions: microwave reflection due to the dielectric contrast between tumor and healthy tissues; EM energy absorption and heating due to higher conductivity of the tumor tissue; tumor vibration and acoustic generation due to the thermo-elastic

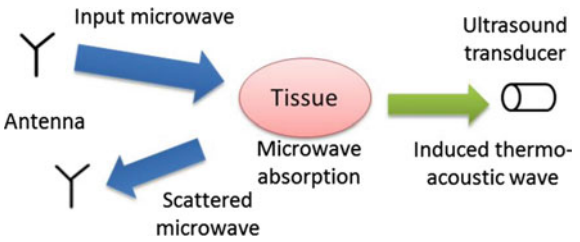

Fig. 2.1 Microwave acoustic interaction with biological tissues, including microwave scattering, EM energy absorption followed by the thermoacoustic effect and acoustic wave generation. Reprinted from Ref. [2] with permission from American Association of Physicists in Medicine

effect; and acoustic reflection due to the acoustic impedance mismatch. The overall equivalent circuit model is shown in Fig. 2.2 and described in detail in the following parts.

2.1.2.1 Microwave Scattering

In order to simplify the complicated numerical simulation for microwave scattering in the biological tissues, we utilize the planar tissue model to demonstrate the reflection and transmission phenomenon at the interface of two mediums with different intrinsic impedance Z_{tissue} shown in Fig. 2.3a:

$$Z_{tissue} = \sqrt{\frac{\mu}{\varepsilon}} = \sqrt{\frac{\mu}{\varepsilon_r - j\frac{\sigma}{\omega\varepsilon_0}}} \tag{2.1}$$

where μ is the permeability, ε is the complex permittivity of tissue, expressed by the permittivity of free space ε_0, the relative permittivity of tissue ε_r, the conductivity σ, and the angular frequency ω. The reflection and transmission coefficients are derived by:

$$R_{microwave} = \left|\frac{Z_{tumor} - Z_{tissue}}{Z_{tumor} + Z_{tissue}}\right| \tag{2.2}$$

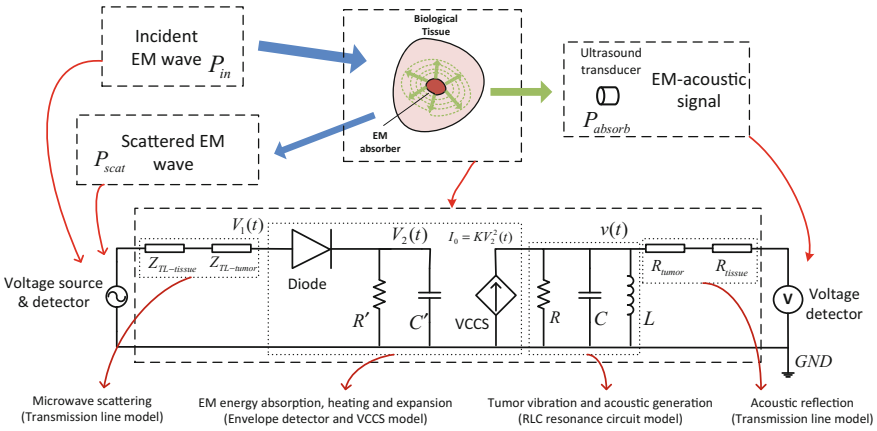

Fig. 2.2 The overall equivalent circuit modeling of microwave acoustic interaction with the biological tissues. Four biophysical interactions are separated by the *dotted lines* and modeled as transmission line mismatch, envelope detector, voltage-controlled current source (VCCS), and parallel RLC resonance circuit. Tumor and surrounding healthy tissues are noted at the *bottom*. Reprinted from Ref. [2] with permission from American Association of Physicists in Medicine

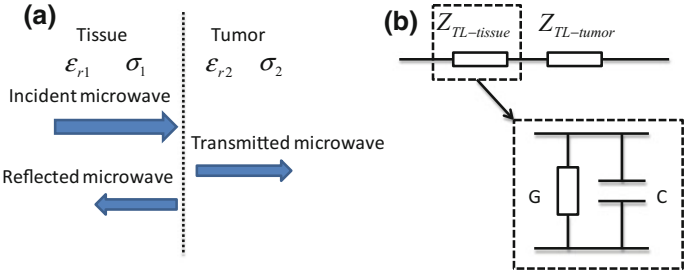

Fig. 2.3 **a** Planar model for tumor and healthy tissue with different dielectric constant and **b** its equivalent circuit model represented by *transmission line*

$$T_{microwave} = \left| \frac{2Z_{tumor}}{Z_{tumor} + Z_{tissue}} \right|. \tag{2.3}$$

Similarly, microwave propagation in transmission line also follows above equations, where the tissue's intrinsic impedance Z_{tissue} is equivalent to the characteristic impedance of transmission line $Z_{TL-tissue}$ in Fig. 2.3b. So we propose:

$$Z_{TL-tissue} = Z_{tissue}. \tag{2.4}$$

By modeling the transmission line as a lumped capacitance and conductance in parallel, the characteristic impedance of transmission line is further expressed as:

$$Z_{TL-tissue} = \frac{1}{G + j\omega C}. \tag{2.5}$$

Substitute Eqs. (2.1) and (2.5) into Eq. (2.4):

$$\frac{1}{G + j\omega C} = \sqrt{\frac{\mu}{\varepsilon_r - j\frac{\sigma}{\omega\varepsilon_0}}} \tag{2.6}$$

then, we have:

$$\mu(G + j\omega C)^2 = \varepsilon_r - j\frac{\sigma}{\omega\varepsilon_0}. \tag{2.7}$$

To obtain the relationship between tissue dielectric parameters (permittivity, conductivity) and transmission line parameters (conductance, capacitance), we equalize the real and imaginary parts of Eq. (2.7) respectively:

$$\mu(G^2 - \omega^2 C^2) = \varepsilon_r \tag{2.8}$$

$$j\mu 2G\omega C = -j\frac{\sigma}{\omega\varepsilon_0} \tag{2.9}$$

then we have:

$$\mu\omega^2 C^2 = \mu G^2 - \varepsilon_r \tag{2.10}$$

$$\mu 2G\omega^2 C = -\frac{\sigma}{\varepsilon_0}. \tag{2.11}$$

By solving Eqs. (2.10) and (2.11), we obtain the expressions of lumped capacitance and conductance of the transmission line in terms of tissues' permittivity and conductivity:

$$C^2 = \frac{-\varepsilon_r + \sqrt{\varepsilon_r^2 + \frac{\sigma^2}{\omega^2\varepsilon_0^2}}}{2\mu\omega^2} \tag{2.12}$$

$$G^2 = \frac{\varepsilon_r + \sqrt{\varepsilon_r^2 + \frac{\sigma^2}{\omega^2\varepsilon_0^2}}}{2\mu}. \tag{2.13}$$

Now the transmission line model of biological tissues for microwave scattering is established and linked with dielectric parameters determined by tissues' permittivity and conductivity using Eqs. (2.12) and (2.13).

2.1.2.2 EM Energy Absorption, Tissue Heating and Expansion

Apart from microwave scattering at the interface of tumor and healthy tissues, EM energy absorption also exists inside the tumor, where conductivity is larger than the surrounding tissues due to higher water content. Following the tissue heating and thermal expansion, initial acoustic pressure $p_0(\vec{r}, t)$ is induced by a pulsed microwave illumination, expressed as:

$$p_0(\vec{r}, t) = \Gamma(\vec{r})A(\vec{r})I(t) \tag{2.14}$$

where $\Gamma(\vec{r}) = \beta c^2/C_P$ is the Gruneisen coefficient at position $\vec{r}$, β is the isobaric volume expansion coefficient, C_P is the specific heat and c is the acoustic velocity propagating in the tissue. $A(\vec{r})$ is the EM energy absorbed by a unit volume tissue at the position $\vec{r}$, and $I(t)$ is the envelope of the microwave pulse. $H(\vec{r}, t) = A(\vec{r})I(t)$ is the heating function, the heating source of initial acoustic pressure. Then we introduce the specific absorption rate (SAR) expressed as: $SAR(\vec{r}, t) = \sigma(\vec{r})|E(\vec{r}, t)|^2/2\rho(\vec{r})$, where $\sigma(\vec{r})$ is the conductivity, $\rho(\vec{r})$ is the tissue density, and $|E(\vec{r}, t)|$ is the temporal envelope of electric field at the position $\vec{r}$. Heating function can also be expressed as $H(\vec{r}, t) = \rho(\vec{r})SAR(\vec{r}, t)$, then we have:

$$p_0(\vec{r},t) = \Gamma(\vec{r})H(\vec{r},t) = \Gamma(\vec{r})\frac{\sigma(\vec{r})}{2}|E(\vec{r},t)|^2. \tag{2.15}$$

In order to model the above process of converting temporal microwave energy to mechanical energy (initial pressure), an envelope detector circuit is proposed to extract the temporal envelope of the electrical field $E(\vec{r},t)$, followed by a voltage-controlled current source (VCCS), which converts the EM energy $|E(\vec{r},t)|^2$ to the initial acoustic pressure $p_0(\vec{r},t)$ linking the parameters in Eq. (2.15).

Shown in Fig. 2.2, a typical envelope detector circuit structure is chosen with a diode, capacitor and resistor. The value of capacitor and resistor is carefully selected to make sure that the output $V_2(t)$ of the envelope detector accurately follows the envelope of input signal:

$$V_2(t) = |E(\vec{r},t)|. \tag{2.16}$$

To represent the energy transformation from the EM wave to the initial acoustic wave, a voltage-controlled current source (VCCS) is introduced converting from voltage to current with a conversion ratio K. By this way, the electric field intensity and initial pressure are expressed by the voltage $V_2(t) = |E(\vec{r},t)|$ and the current $I_0(t) = p_0(\vec{r},t)$ respectively. According to Eqs. (2.15) and (2.16), the VCCS is formulated by:

$$I_0(t) = p_0(\vec{r},t) = KV_2(t)^2 \tag{2.17}$$

$$K = \frac{1}{2}\Gamma(\vec{r})\sigma(\vec{r}). \tag{2.18}$$

Up to now, the initial acoustic pressure has been modeled as $I_0(t)$ that is pumped by a voltage-controlled current source (VCCS).

2.1.2.3 Tumor Vibration and Acoustic Generation

Starting from the radiative transport equation and Navier-Stokes equation, a general wave equation is obtained for the photoacoustic pressure in a tissue medium [2, 3]:

$$\begin{aligned}\frac{1}{c^2}\frac{\partial^2}{\partial t^2}p(\vec{r},t) = \nabla^2 p(\vec{r},t) + \frac{\xi+\frac{4}{3}\eta}{\rho(\vec{r})c^2}\frac{\partial}{\partial t}\nabla^2 p(\vec{r},t) \\ -\frac{\xi+\frac{4}{3}\eta}{\rho(\vec{r})c^2}\Gamma(\vec{r})\nabla^2 H(\vec{r},t) + \frac{\Gamma(\vec{r})}{c^2}\frac{\partial H(\vec{r},t)}{\partial t}\end{aligned} \tag{2.19}$$

where η is the shear viscosity, ξ is the bulk viscosity, c is the acoustic velocity, $\rho(\vec{r})$ is the tissue density, and $H(\vec{r},t)$ is the heat function. For thermoacoustic effect that

we are interested here, the heating source is a pulsed microwave with heat function expressed as:

$$H(\vec{r},t)=\frac{\sigma(\vec{r})}{2}|E(\vec{r},t)|^2. \tag{2.20}$$

Firstly we consider homogeneous small-size tumor model as a point source with the constant $\sigma(\vec{r})$ and $|E(\vec{r},t)|$ along spatial dimension (extension analysis to imaging will be discussed later), we have:

$$\nabla^2 H(\vec{r},t)=0. \tag{2.21}$$

Then substituting Eqs. (2.15) and (2.21) into Eq. (2.19) achieves:

$$\frac{\partial^2}{\partial t^2}p(\vec{r},t)=c^2\nabla^2 p(\vec{r},t)+\frac{\xi+\frac{4}{3}\eta}{\rho(\vec{r})}\frac{\partial}{\partial t}\nabla^2 p(\vec{r},t)+\frac{\partial p_0(\vec{r},t)}{\partial t}. \tag{2.22}$$

Assume that the acoustic pressure at position $\vec{r}$ could be expressed as $p(\vec{r},t)=e^{iar}p(t)$ [3], where a is the wave number, so that the pressure $p(t)$ is simplified to be only from a point source at a specific position r, where the spatial distribution of pressure $p(r)$ is not considered. Then Eq. (2.22) is simplified to:

$$\frac{\partial^2}{\partial t^2}p(t)+\frac{\xi+\frac{4}{3}\eta}{\rho(\vec{r})}\frac{\partial}{\partial t}p(t)+c^2 p(t)=\frac{1}{a^2}\frac{\partial p_0(\vec{r},t)}{\partial t}. \tag{2.23}$$

To accurately model the above second order differential pressure equation, a parallel RLC structure shown in Fig. 2.2 is brought in the circuit model. Interestingly, in this parallel RLC circuit pumped by the current source modeled as VCCS mentioned above, the source current and output voltage also follow the similar second order differential equation shown below:

$$\frac{\partial^2}{\partial t^2}v(t)+\frac{1}{RC}\frac{\partial}{\partial t}v(t)+\frac{1}{LC}v(t)=\frac{1}{C}\frac{\partial I_0(t)}{\partial t}. \tag{2.24}$$

Comparing Eqs. (2.23) and (2.24), it is intuitive to equalize $v(t)=p(t)$ and $I_0(t)=p(\vec{r},t)$, then we map the parameters in these two equations one by one:

$$\begin{aligned}\frac{1}{a^2}&=\frac{1}{C}\\ \frac{\xi+\frac{4}{3}\eta}{\rho(\vec{r})}&=\frac{1}{RC}\\ c^2&=\frac{1}{LC}.\end{aligned} \tag{2.25}$$

Solving Eq. (2.25), we have:

$$\begin{aligned} C &= a^2 \\ L &= \frac{1}{c^2} \\ R &= \frac{\rho(\vec{r})}{(\xi + \frac{4}{3}\eta)}. \end{aligned} \tag{2.26}$$

According to Eq. (2.26), the value of each circuit element is obtained from biological parameters in terms of acoustic velocity, tissue density, propagation phase constant and viscosity. In order to analytically solve the second order differential Eq. (2.24), The current source term $\partial I_0(t)/\partial t$ of the parallel RLC circuit is expressed as $Q_0\delta(t)$, where $\delta(t)$ is impulse function, then the explicit solution is derived as:

$$v(t) = \frac{Q_0}{C}\frac{\omega_0}{\omega_\mathrm{d}}\exp(-\alpha t)cos\left(\omega_d t + \tan^{-1}\left(\frac{\alpha}{\omega_d}\right)\right) \tag{2.27}$$

where $Q_0 = |I_0|$ is the amplitude of the impulse source, and

$$\omega_0 = \sqrt{\frac{1}{LC}} = c \tag{2.28}$$

$$\alpha = \frac{1}{2RC} = \frac{\xi + \frac{4}{3}\eta}{2\rho(\vec{r})} \tag{2.29}$$

$$\omega_d = \sqrt{\omega_0^2 - \alpha^2} = \sqrt{c^2 - \left(\frac{\xi + \frac{4}{3}\eta}{2\rho(\vec{r})}\right)^2}. \tag{2.30}$$

Then substitute Eqs. (2.28)–(2.30) into Eq. (2.27), we obtain the amplitude of Eq. (2.27) expressed by $|v(t)|$ in terms of biological parameters:

$$|v(t)| = |I_0|\frac{1}{\sqrt{1 - (\frac{\xi + \frac{4}{3}\eta}{2c\rho(\vec{r})})^2}}\exp(-\frac{\xi + \frac{4}{3}\eta}{2\rho(\vec{r})}t). \tag{2.31}$$

Now the microwave-induced thermoacoustic signal $p(t)$ is modeled as $v(t)$ shown in Fig. 2.2 by Eqs. (2.27)–(2.31).

2.1.2.4 Acoustic Reflection

Similar with microwave propagation in biological tissues, the acoustic signal reflection also exists at the interface of two biological tissues (tumor and healthy

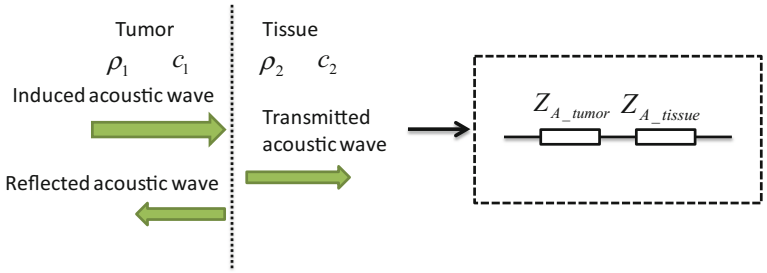

Fig. 2.4 Planar model for tumor and healthy tissues with different acoustic impedance represented by *transmission line* in circuit modeling

tissue) with different acoustic impedance R_{tumor} and R_{tissue} shown in Fig. 2.4. Equivalent to Eqs. (2.2)–(2.4), the reflection and transmission coefficient for acoustic impedance mismatch are:

$$\begin{aligned} R_{acoustic} &= \left| \frac{R_{tumor} - R_{tissue}}{R_{tumor} + R_{tissue}} \right| \\ T_{acoustic} &= \left| \frac{2R_{tumor}}{R_{tumor} + R_{tissue}} \right| \\ R_{tumor} = \rho_1 c_1,\ R_{tissue} &= \rho_2 c_2. \end{aligned} \tag{2.32}$$

Transmission line with same characteristic impedance as tissue's acoustic impedance is used to model the acoustic mismatch.

2.1.3 Characteristic Gain of Microwave-Acoustic Imaging

In this section, we extract the tumor circuit model that is established in the previous section to be a two-port network, to be represented by pseudo S-parameters. Incorporating source and load model together, a transducer gain is derived and proposed as a characteristic gain to evaluate the whole microwave acoustic imaging system.

2.1.3.1 Pseudo S-parameter Extraction

In order to analyze the equivalent circuit model in top level, a two-port network is proposed to represent the tumor circuit model using pseudo S-parameters correlating microwave and acoustic parameters, which has similar formulation but totally

different definition compared with scattering parameter in microwave community. As shown in Fig. 2.5, a microwave signal is reflected at the input port determined by S_{11} due to the dielectric contrast. The induced thermoacoustic wave is generated and reflected at the output port with the transmission coefficient S_{21} and the acoustic reflection coefficient S_{22} due to the acoustic impedance contrast. Because the thermoacoustic effect induced by pulse microwave illumination is irreversible, i.e. microwave cannot be generated by input acoustic pressure, the reverse transmission coefficient S_{12} is zero. In this case, this two-port network of the tumor model is unilateral. Recall Eq. (2.2) for microwave reflection, we have:

$$S_{11} = \left| \frac{\frac{Z_{tumor}}{Z_{tissue}} - 1}{\frac{Z_{tumor}}{Z_{tissue}} + 1} \right|. \tag{2.33}$$

Substitute Eq. (2.1) into Eq. (2.33) using dielectric constant of tumor and healthy tissue $(\varepsilon_1, \varepsilon_2)$, we obtain:

$$S_{11} = \left| \frac{\sqrt{\frac{\varepsilon_1}{\varepsilon_2}} - 1}{\sqrt{\frac{\varepsilon_1}{\varepsilon_2}} + 1} \right|. \tag{2.34}$$

It is clearly shown that S_{11} is determined by the difference of dielectric constant. Similarly, the acoustic reflection coefficient at the output port could be expressed as:

$$S_{22} = \left| \frac{\frac{R_{tumor}}{R_{tissue}} - 1}{\frac{R_{tumor}}{R_{tissue}} + 1} \right| = \left| \frac{\frac{\rho_1 c_1}{\rho_2 c_2} - 1}{\frac{\rho_1 c_1}{\rho_2 c_2} + 1} \right| \tag{2.35}$$

and S_{22} is related with the acoustic impedance mismatch. To derive the transmission coefficient S_{21}, we firstly substitute Eqs. (2.17) and (2.18) into Eq. (2.31):

$$|v(t)| = \frac{1}{2}\Gamma(\vec{r})\sigma(\vec{r})V_2(t)^2 \frac{1}{\sqrt{1 - (\frac{\xi + \frac{4}{3}\eta}{2c\rho(\vec{r})})^2}} \exp(-\frac{\xi + \frac{4}{3}\eta}{2\rho(\vec{r})}t). \tag{2.36}$$

We can calculate S_{21} as the transmission coefficient from the input microwave energy to the induced acoustic pressure due to the conductivity mismatch between the tumor and healthy tissues, then we have:

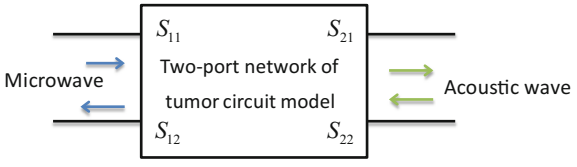

Fig. 2.5 Extracted two-port network of tumor circuit model represented by pseudo S-parameters

$$S_{21} = \frac{|v(t)|}{V_2(t)^2} = \frac{1}{2}\Gamma(\vec{r})|\sigma_2(\vec{r}) - \sigma_1(\vec{r})| \frac{1}{\sqrt{1 - (\frac{\xi + \frac{4}{3}\eta}{2c\rho(\vec{r})})^2}} \exp(-\frac{\xi + \frac{4}{3}\eta}{2\rho(\vec{r})}t). \quad (2.37)$$

From Eq. (2.37), we can easily find that S_{21} is mainly determined by two factors: conductivity $\sigma(\vec{r})$ and viscosity $\xi + 4\eta/3$ of the tumor tissue, which refers to the microwave absorption rate and attenuation term in Eq. (2.37), respectively. Finally the pseudo S-parameters of the proposed two-port network of tumor tissue are summarized in Eq. (2.38).

$$\begin{pmatrix} S_{11} & S_{21} \\ S_{12} & S_{22} \end{pmatrix} = \begin{pmatrix} \left|\frac{\sqrt{\frac{\varepsilon_1}{\varepsilon_2}} - 1}{\sqrt{\frac{\varepsilon_1}{\varepsilon_2}} + 1}\right| & \frac{1}{2}\Gamma(\vec{r})|\sigma_2(\vec{r}) - \sigma_1(\vec{r})| \frac{1}{\sqrt{1 - (\frac{\xi + \frac{4}{3}\eta}{2c\rho(\vec{r})})^2}} \exp(-\frac{\xi + \frac{4}{3}\eta}{2\rho(\vec{r})}t) \\ 0 & \left|\frac{\frac{\rho_1 c_1}{\rho_2 c_2} - 1}{\frac{\rho_1 c_1}{\rho_2 c_2} + 1}\right| \end{pmatrix} \quad (2.38)$$

2.1.3.2 Complete Circuit Model

Added to the 2-port network of tumor circuit model represented by pseudo S-parameters, a more complete circuit model incorporating the impedance mismatch at the generator and load sides is proposed and shown in Fig. 2.6. In this complete circuit model, the surrounding healthy tissue along with skin tissue is modeled as transmission line with characteristic impedance Z_{tissue}. At the input side, source impedance Z_G is brought into model the impedance of the antenna, which is assumed to be attached directly on the skin, and connected to microwave transceiver module (TRX) that is capable of transmitting input microwave and receiving scattered microwave signal. Γ_G is the reflection coefficient at the input side representing the impedance mismatch between the antenna and the skin tissue, and expressed as:

$$\Gamma_G = \left|\frac{Z_G - Z_{tissue}}{Z_G + Z_{tissue}}\right|. \quad (2.39)$$

At the load side, Z_L is used to model the acoustic impedance of ultrasound transducers, and Γ_L is describing the acoustic mismatch between the skin tissue and ultrasound transducers:

$$\Gamma_G = \left|\frac{Z_L - R_{tissue}}{Z_L + R_{tissue}}\right|. \quad (2.40)$$

Acoustic receiver (RX) follows the ultrasound transducers for signal amplification and processing.

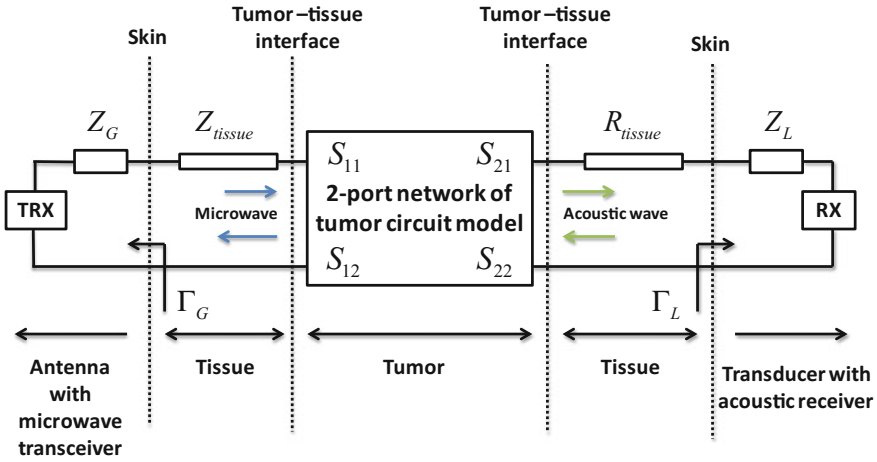

Fig. 2.6 Complete circuit model combining 2-port network of tumor represented by pseudo S-parameters, surrounding healthy tissue impedance Z_{tissue}, antenna and ultrasound transducer impedance Z_G, Z_L for EM and acoustic wave, together with microwave transceiver TRX and acoustic receiver RX. Reflection coefficient Γ_G and Γ_L represent impedance mismatch for microwave and acoustic wave at antenna and transducer sides respectively

2.1.3.3 Transducer Gain as Characteristic Gain

To analyze the complete circuit model, the transducer gain G_T is engaged to be an indicator for tissue characterization and imaging, covering all the parameters in the model:

$$G_T = \frac{\left(1-|\Gamma_G|^2\right)|S_{21}|^2\left(1-|\Gamma_L|^2\right)}{|(1-S_{11}\Gamma_G)(1-S_{22}\Gamma_L)-S_{12}S_{21}\Gamma_G\Gamma_L|^2} \tag{2.41}$$

substitute $S_{12}=0$ into Eq. (2.41), we have:

$$G_T = \frac{\left(1-|\Gamma_G|^2\right)|S_{21}|^2\left(1-|\Gamma_L|^2\right)}{|(1-S_{11}\Gamma_G)(1-S_{22}\Gamma_L)|^2}. \tag{2.42}$$

The transducer gain G_T incorporates S_{11}, S_{22}, S_{21}, Γ_G and Γ_L to fully characterize the complete 2-port network. Equivalently, the microwave scattering (S_{11}), the acoustic reflection (S_{22}), the thermoacoustic effect (S_{21}), the antenna skin mismatch (Γ_G) and the transducer-skin mismatch (Γ_L) are all incorporated into the transducer gain, which is defined as the characteristic gain to quantitatively characterize the microwave acoustic imaging modality.

Up to now, all the analysis above is based on the assumption that the tumor tissue is homogeneous and small enough to be modeled as a point. In order to

extend the equivalent circuit model for real microwave acoustic imaging application, the biological tissue could be partitioned into a number of small grids, within each grid the biological tissue is still eligible to be considered as a point model. By applying the proposed equivalent circuit model to fit each small grid of the biological tissue, similar with FDTD method assigning dielectric constant to each grid cell, it is potential to simulate the whole tissue imaging, which will be discussed in Sect. 2.1.6. Furthermore, functional imaging is also possible by calculating the characteristic gain at each grid cell, which could fully characterize the microwave and acoustic properties of the tissue sample.

2.1.4 Simulation

In order to verify the validity of the equivalent circuit model established in the previous section, both numerical simulation and SPICE circuit simulation are conducted and compared. A Gaussian modulated microwave with 1 GHz central frequency and 0.1 μs pulse width is used to illuminate the biological tissues, shown in Fig. 2.7a. The 2D numerical biological tissue structure for FDTD EM and acoustic simulation is demonstrated in Fig. 2.7b, the homogeneous fat tissue is surrounded by the skin, and the tumor with 0.1 mm diameter (as a point source) is embedded in the center of the field. The microwave transmitter and receiver are placed at the top side and the ultrasound transducer is placed at the other side. The grid size of the FDTD simulation is 0.4 mm for the EM simulation and 0.1 mm for the acoustic simulation due to the much smaller wavelength of acoustic wave. Perfectly matched layer (PML) is utilized to terminate the computational region. In EM simulation, the scattered microwave is recorded by the receiver and the tumor response is calculated by subtracting the calibration signal recorded without the tumor. SAR is calculated at every grid cell and interpolated for the following acoustic simulation. Dielectric properties of tumor, skin and fat at 1 GHz, are listed in Table 2.1, together with other biological parameters for FDTD numerical simulation. Acoustic attenuation coefficient α is related with shear and bulk viscosity by:

$$\alpha = \frac{2f^2\pi^2}{3\rho c^3}\left(\frac{4}{3}\eta + \xi\right). \tag{2.43}$$

Circuit element parameters are calculated based on the established equivalent circuit model and listed in Table 2.2. Some of the circuit parameters are only for tumor modeling and not applicable to other tissues, noted as N.A. R' and C' are selected to extract the envelope of the microwave input properly. C is normalized as unity in the equivalent modeling.

Numerical and circuit simulations are conducted separately using the FDTD and SPICE analysis. Time-domain simulation results are shown in Fig. 2.8a, c, where the acoustic waveforms generated from SPICE and FDTD simulation are in good agreement as N-shape pulse with comparable magnitude. The spectra of acoustic

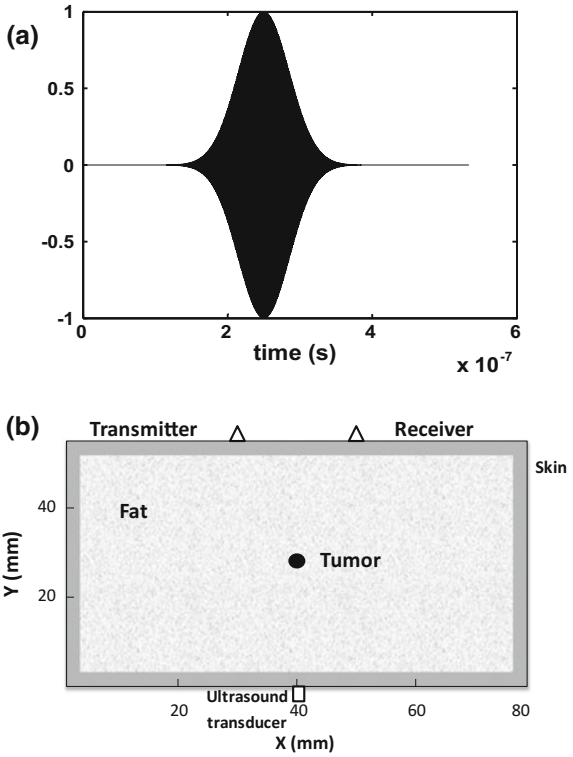

Fig. 2.7 **a** Gaussian modulated microwave source and **b** 2D numerical biological tissue model for EM and acoustic simulation

Table 2.1 Physical parameters of biological tissues [4]

Tissue	Fat	Skin	Tumor
ε_0 (F/m)	8.85×10^{-12}	8.85×10^{-12}	8.85×10^{-12}
ε_r	5.4079	40.936	54.811
μ_0 (H/m)	$4\pi \times 10^{-7}$	$4\pi \times 10^{-7}$	$4\pi \times 10^{-7}$
σ (S/m)	0.0528	0.8818	0.9782
ρ (kg/m^3)	1020	1100	1041
c (m/s)	1510	1537	1580
β (1/°C)	3×10^{-4}	3×10^{-4}	3×10^{-4}
C_P (J/(°C kg))	3550	3550	3510
α (dB/cm)	0.75	3.5	0.57

signals are shown in Fig. 2.8b, d with a similar central frequency and bandwidth. The validity of the equivalent circuit modeling is verified, and the minor difference between them is due to the simplicity of circuit modeling, e.g., the waveform of acoustic signals also depends on the actual size of the tumor, which is not taken into account in the equivalent circuit modeling here.

Table 2.2 Equivalent circuit parameters of three biological tissues [4]

Tissue	Fat	Skin	Tumor
$Z_{TL-tissue}$ (Ω)	4.7660×10^{-4} + j4.1524×10^{-5}	1.6631×10^{-4} + j3.1087×10^{-5}	1.4597×10^{-4} + j2.2851×10^{-5}
$G_{TL-tissue}$ (S)	2082.4	5809.9	6686.8
$C_{TL-tissue}$ (F)	2.8875×10^{-8}	1.7284×10^{-7}	1.6660×10^{-7}
R_3 (Ω)	N.A.	N.A.	1000
C_3 (F)	N.A.	N.A.	10×10^{-12}
K	N.A.	N.A.	3.5804×10^{5}
R (Ω)	N.A.	N.A.	1.1706×10^{10}
L (H)	N.A.	N.A.	4.0058×10^{-7}
C (F)	N.A.	N.A.	1×10^{-6}
R_{tissue} (Ω)	1.5402×10^{6}	1.6907×10^{6}	1.6448×10^{6}

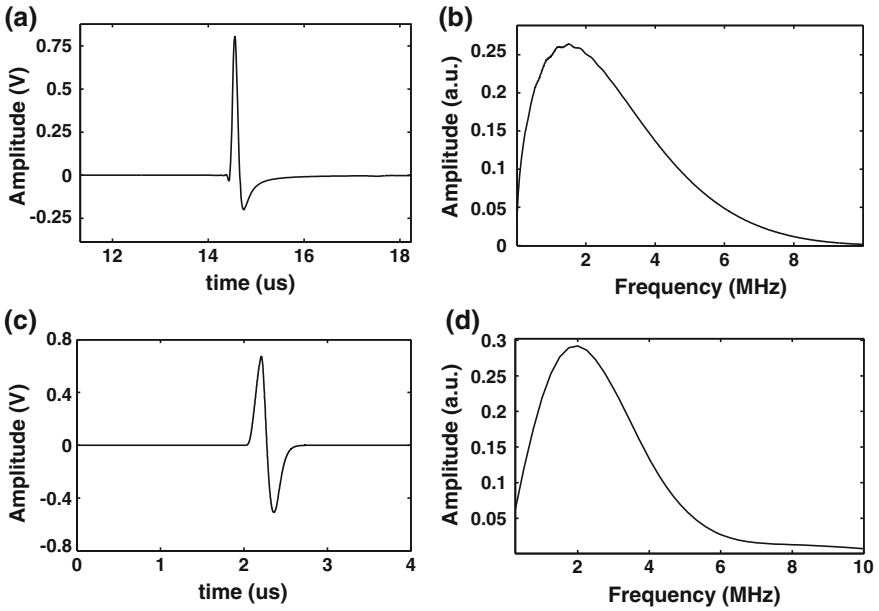

Fig. 2.8 Numerical simulation (**a**, **b**) and circuit simulation (**c**, **d**) results of thermoacoustic signals in both time and frequency domain

In another set of comparable simulations, the dielectric contrast between the tumor tissue and surrounding normal tissues is set to be variable, and summarized in Table 2.3. S_{11} and S_{21} are obtained, as well as the transducer gain G_T, which is defined as the characteristic gain for microwave acoustic imaging system. Shown in

Table 2.3 Summary of ten simulation cases with different dielectric contrast [4]

Dielectric constant of tumor at 1 GHz ε_r = 54.811, σ = 0.9782 S/m			
Case	Normal tissue permittivity	Normal tissue conductivity (S/m)	Dielectric contrast
1	49.828	0.8893	1.1
2	45.676	0.8152	1.2
3	42.162	0.7525	1.3
4	39.151	0.6987	1.4
5	36.541	0.6521	1.5
6	34.257	0.6114	1.6
7	32.242	0.5754	1.7
8	30.451	0.5434	1.8
9	28.848	0.5148	1.9
10	27.406	0.4891	2.0

Fig. 2.9, when the dielectric contrast is increasing for both the numerical and circuit simulation, S_{11} and S_{21} are increasing together with the transducer gain (characteristic gain). The changing trends of the pseudo S-parameter and characteristic gain with dielectric contrast variation are coincident in both simulations, which is compatible with physical principles of microwave acoustic imaging as well.

It is obvious that collecting both S_{11} and S_{21} is appreciated to maximize the characteristic gain. From Fig. 2.9a, b, we see that for the contrast ranging from 1.2

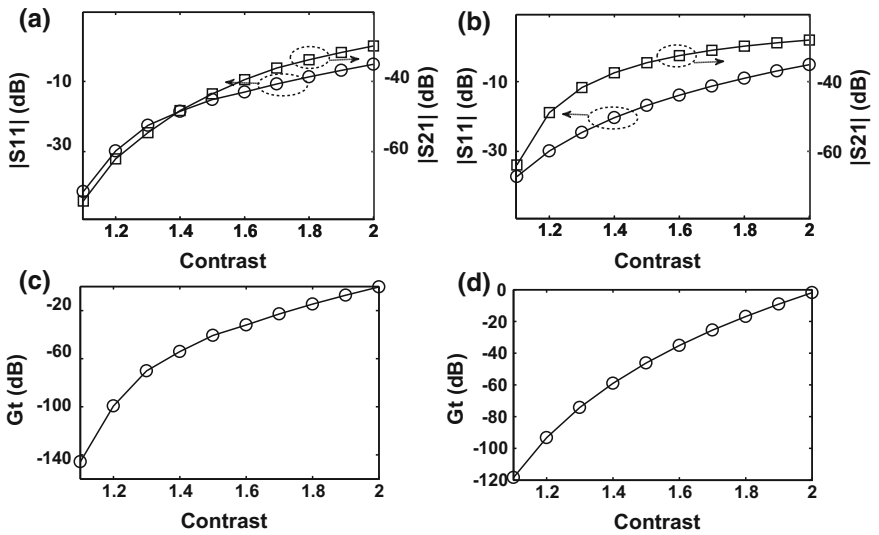

Fig. 2.9 Magnitude of S_{11} and S_{21} of numerical simulation (**a**) and circuit simulation (**b**) and their respective characteristic gain in (**c**, **d**) as a function of dielectric contrasts

to 1.8, about 20 dB (numerical simulation) and 22 dB (circuit simulation) increase are obtained. However, the characteristic gain achieves about 80 and 75 dB respectively, which implies a significant sensitivity enhancement with the characteristic gain than S11 or S21 only. It predicts that the combination of microwave imaging and microwave-induced thermoacoustic imaging is expected to offer enhanced performance, which has been researched by numerical simulations in very recent work for benign and malignant tumor differentiation [5, 6]. Interestingly, according to the expression (2.42) of the transducer gain, it is intuitive to see that S_{11}, S_{21}, and S_{22} are preferred to be large, together with preferred small Γ_G and Γ_L. Combining of photoacoustic or thermoacoustic with ultrasound imaging has also been proposed recently, which is to maximize S_{21} and S_{22} at the same time [7, 8]. To maximize the characteristic gain, a new medical imaging modality, which combines microwave imaging, thermoacoustic imaging and ultrasound imaging together, is supposed to improve the performance further. On the other hand, minimizing Γ_G and Γ_L refers to the minimum reflection at the skin for microwave and acoustic propagation. Antennas attached to the skin is expected to specifically designed for the microwave acoustic imaging modality with high power coupling efficiency, such as in [9]. Meanwhile, ultrasound transducers should also be designed with similar acoustic impedance of the skin to reduce the acoustic reflection at the skin surface [10].

2.1.5 *Experimental Verification*

In order to further verify the validity of the proposed equivalent circuit modeling, we build an experimental setup, which is capable of collecting scattering microwave signals and induced thermoacoustic signals simultaneously. Shown in Fig. 2.10, a microwave generator (SMBV100 A, Rohde & Schwarz) under the amplitude shift keying (ASK) configuration is used to provide Gaussian pulse modulated microwave, which is amplified up to 100 W peak power by a microwave power amplifier (ZHL-100W-GAN+, Mini-Circuits). Due to the power and bandwidth limit (up to 100 W and 500 MHz) of the power amplifier, we choose 440 MHz as carrier frequency and 2 μs pulse width so as to deliver up to 0.2 mJ/pulse into biological tissues. The amplified Gaussian modulated microwave is fed into a custom-designed helical antenna with narrow radiation pattern at the output and operating at 440 MHz, whose measured S11 is plotted in Fig. 2.11. Meanwhile, the scattered microwave signal is received by another helical antenna placed at the other side, and the thermoacoustic signal due to the microwave absorption is also collected by an ultrasound transducer (V323-SU, Olympus) with 2.25 MHz central frequency, followed by an ultrasound preamplifier with 54 dB gain (Model 5662, Olympus). Both the scattered microwave and thermoacoustic signals are recorded with a digital oscilloscope (WaveMaster 8000 A, Lecroy) at 5 G samples/s rate. In the tank, both the microwave antennas and the ultrasound transducer are immersed in mineral oil ($\varepsilon_r = 2.1, \sigma \approx 0$). The tissue sample is

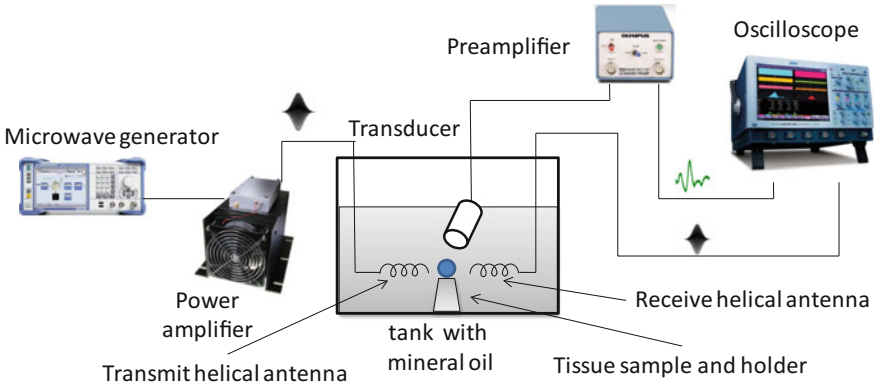

Fig. 2.10 Experimental setup capable of collecting both scattering microwave and induced thermoacoustic wave simultaneously

Fig. 2.11 Measured S_{11} of the custom-designed antenna

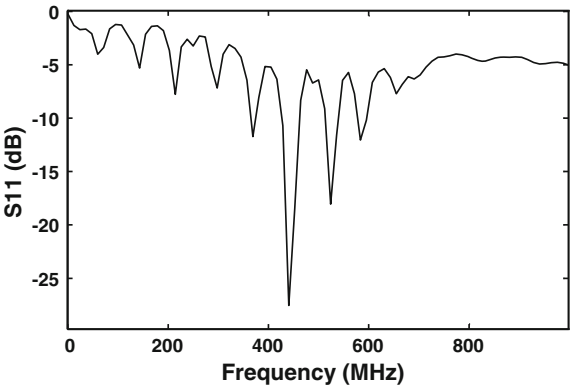

placed near the end of the transmitting helical antenna for maximum microwave illumination.

Four kinds of porcine tissues (kidney, liver, muscle, fat) with different dielectric constants are prepared. Made in small round shape with 5 mm diameter, the tissue is placed close to both the antenna and the transducer. The recorded microwave and thermoacoustic wave of muscle tissue are shown in Fig. 2.12a, b. After low-pass filtering, the thermoacoustic wave in time and frequency domain is shown in Fig. 2.12c, d with green solid lines. To compare the measured results with circuit simulation results based on the equivalent circuit model, we substitute the biological parameters (permittivity and conductivity) of these four tissues in Table 2.4 into the model to obtain the concerned circuit parameters listed in Table 2.5. Stimulated by 440 MHz Gaussian modulated source with 2 μs pulse width, the circuit simulated thermoacoustic signal is shown in time and frequency domain in Fig. 2.12c, d in red

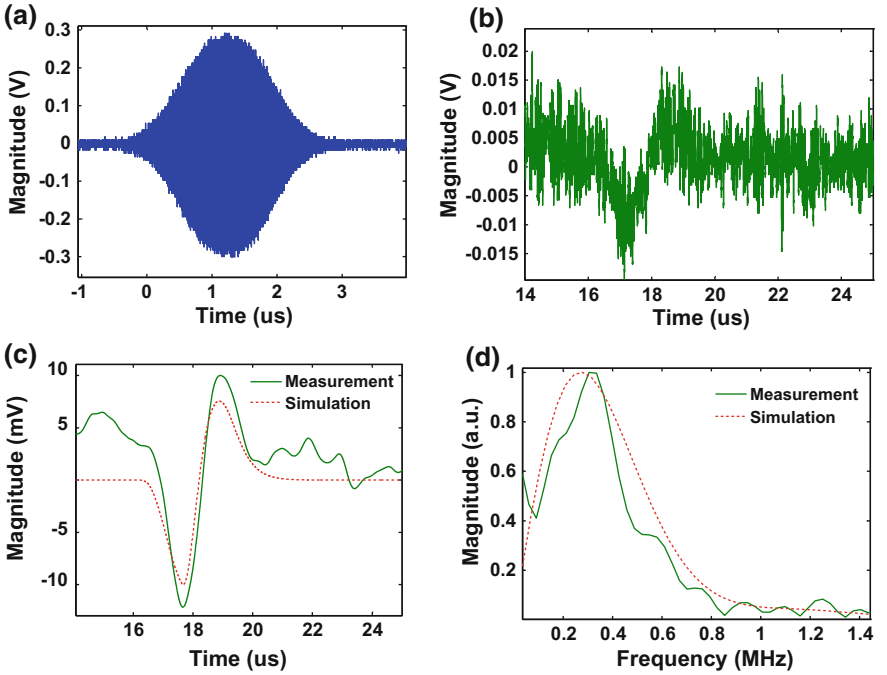

Fig. 2.12 **a** Experiment measured scattering microwave signal and **b** thermoacoustic signal. **c** Low-pass filtered thermoacoustic signal of measurement and circuit simulation in time domain. **d** Thermoacoustic signal spectrum of measurement and circuit simulation

Table 2.4 Dielectric constant of four biological tissues at 440 MHz [4]

Tissue	Fat	Liver	Muscle	Kidney
ε_r	5.5641	50.583	56.823	65.263
σ (S/m)	0.0417	0.6704	0.8066	1.1209

Table 2.5 Concerned circuit parameters of four biological tissues [4]

Tissue	Fat	Liver	Muscle	Kidney
$Z_{TL-tissue}$ (Ω)	4.7204×10^{-4} + j3.1667×10^{-5}	1.5439×10^{-4} + j1.8145×10^{-5}	1.4524×10^{-4} + j1.8246×10^{-5}	1.3412×10^{-4} + j2.0241×10^{-5}
$G_{TL-tissue}$ (S)	2109	6388.8	6778.2	7290.1
$C_{TL-tissue}$ (F)	2.2518×10^{-8}	1.1950×10^{-7}	1.3552×10^{-7}	1.7510×10^{-7}
K	1.3659×10^{4}	2.1960×10^{5}	2.6421×10^{5}	3.6717×10^{5}

dotted lines. Compared with measured waveform in Fig. 2.12c, d in green solid lines, they display comparable time and frequency domain characteristics.

S_{11}, S_{21} and transducer gain G_T are all calculated and shown in Fig. 2.13. Compatible with simulation results in Fig. 2.9, they demonstrate same

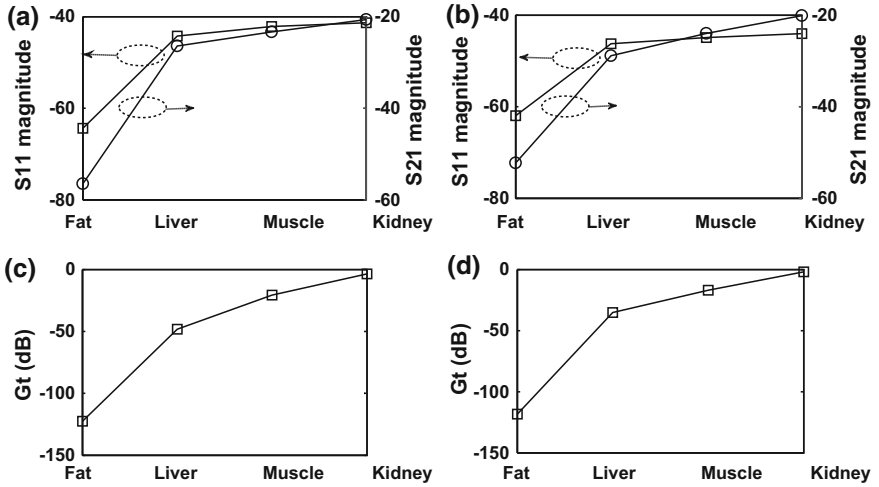

Fig. 2.13 Magnitude of S_{11} and S_{21} of experiment measurement (**a**), circuit simulation (**b**), and their respective transducer gain in (**c**, **d**) for four different biological tissues at 440 MHz

characteristic, i.e., S_{11}, S_{21} and G_T are all increasing with larger dielectric contrast between tissue and mineral oil.

2.1.6 2D Circuit Network Modeling for Heterogeneous Scenarios

In the previous sections, a complete circuit model of the tumor is fully described assuming that the tumor is small enough to be treated as an ideal point source, where no spatial information and heterogeneous situations are included. In this section, the circuit model of an ideal point is extended to a 2D circuit network as shown in Fig. 2.14a, where two main building blocks are the source unit at every grid, and acoustic channel linking the adjacent source unit, which is with the acoustic delay and attenuation characteristics. By assigning each grid with specific parameters for source unit and acoustic channels, it enables the 2D circuit simulation of heterogeneous medium, which is a significant step closer to the real human body situations. The details of the circuit network modeling will be discussed in details as below.

2.1.6.1 Source Unit

To simplify the circuit network modeling, every source unit is only connected with the adjacent four source units in vertical and horizontal directions. Therefore, the

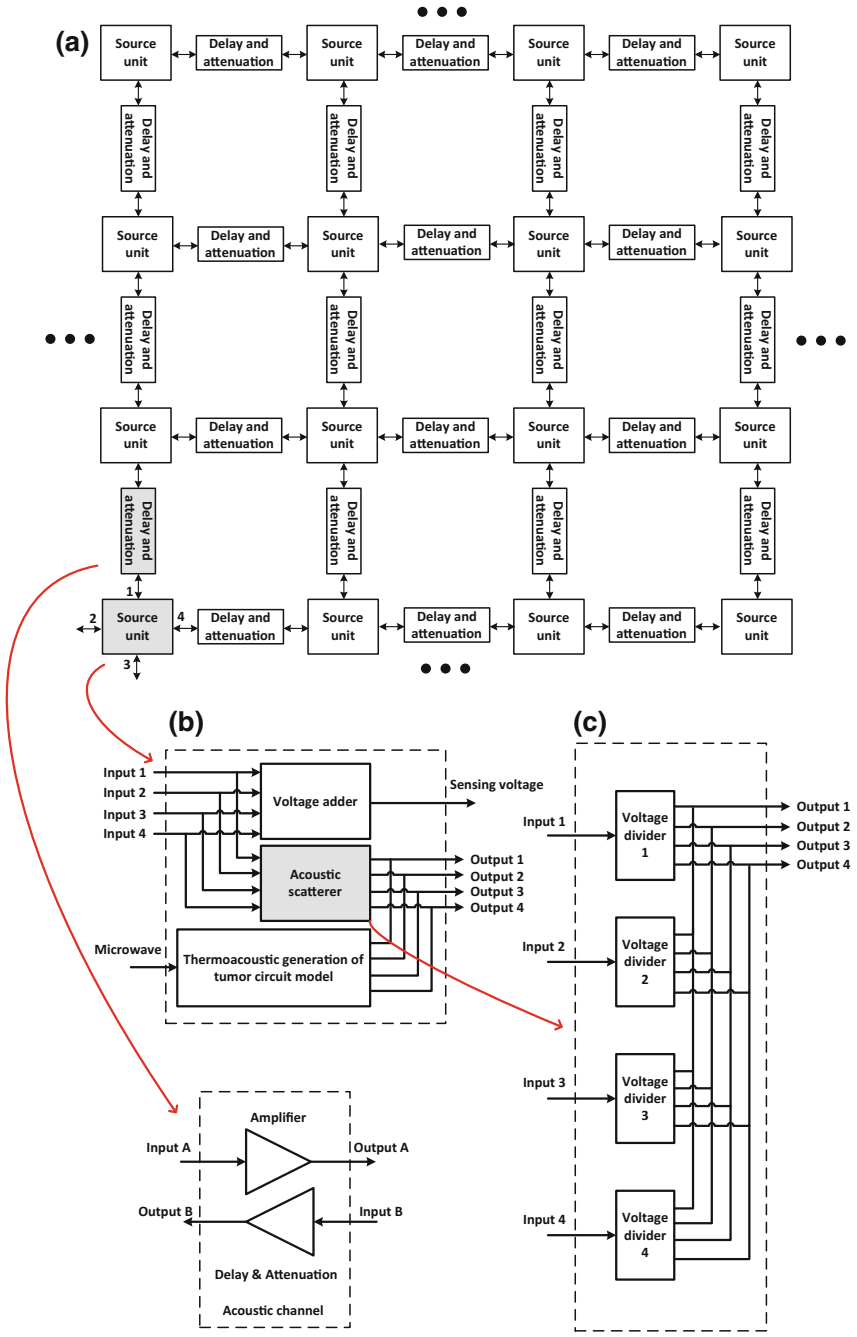
(a)
Source unit
Delay and attenuation
1
2
3
4
(b)
Input 1
Input 2
Input 3
Input 4
Voltage adder
Sensing voltage
Acoustic scatterer
Output 1
Output 2
Output 3
Output 4
Microwave
Thermoacoustic generation of tumor circuit model
Amplifier
Input A
Output A
Output B
Input B
Delay & Attenuation
Acoustic channel
(c)
Input 1
Voltage divider 1
Input 2
Voltage divider 2
Input 3
Voltage divider 3
Input 4
Voltage divider 4
Output 1
Output 2
Output 3
Output 4

◂**Fig. 2.14** **a** 2D circuit network modeling incorporating the spatial information and heterogeneous situations. **b** Circuit structures of the source unit and *acoustic channel blocks*. **c** Circuit structure of the acoustic *scatter block*. Reprinted from Ref. [2] with permission from American Association of Physicists in Medicine

four inputs and four outputs in Fig. 2.14b represent the input and output in the top, left, bottom and right directions of the grid, respectively. The building blocks of the source unit include voltage adder, acoustic scatterer, and the thermoacoustic generation of the tumor circuit model.

The voltage adder performs the summation of the four input voltage signals from four directions, which represent the acoustic propagation towards the source unit. Thus the sensing voltage is used to monitor the acoustic pressure at this source unit:

$$p_{unit} = v_{\text{sensing}} = v_{\text{input 1}} + v_{\text{input 2}} + v_{\text{input 3}} + v_{\text{input 4}}. \tag{2.44}$$

The voltage scatterer performs the acoustic scattering effect during its propagation through each grid and will be discussed later. The thermoacoustic generation of the tumor circuit model is copied from the previous sections, where the microwave comes in, and acoustic wave goes out. One difference is that the tumor model here has four outputs, representing the wave generation and propagation towards all four the directions, which are added with the outputs of the acoustic scatterer to give the final outputs following the acoustic superposition phenomenon.

2.1.6.2 Acoustic Channel

Acoustic channel circuit model is used to model the acoustic wave propagation between adjacent grids, where the delay and attenuations are two key parameters to characterize the acoustic channel. Here two ideal amplifiers with tunable delay and attenuation parameters are employed to model the bi-directional acoustic propagations. To define the two parameters, we assume that the grid size (distance between two adjacent grids) is d_{grid} (mm), and the acoustic attenuation is α_{grid} (dB/mm). Then the delay and gain parameters of the amplifier in the circuit model are obtained by:

$$\begin{aligned} delay &= d_{\text{grid}}/c \ (\mu\text{s}) \\ attenuation &= \alpha_{\text{grid}} d_{\text{grid}} \ (\text{dB}), \end{aligned} \tag{2.45}$$

where c is the acoustic velocity ($\sim$1500 mm/μs in soft tissues). Then the acoustic channel is properly modeled by the circuit blocks with delay and attenuation characteristics.

2.1.6.3 Acoustic Scatterer

The acoustic scatterer in the source unit is used to model the acoustic scattering effect of the incident acoustic wave from all four directions. As shown in Fig. 2.14c, the acoustic scatterer is comprised of four voltage dividers, where each divider is used to divide the input signal from each direction into four output signals. By doing so, acoustic wave coming in from each direction is scattered into four acoustic waves coming out to adjacent grids. Therefore, there are totally 16 scattering coefficients to be defined as $S_{m,n}, 1 \leq m \leq 4, 1 \leq n \leq 4$, where $S_{m,n}$ is the acoustic scattering coefficient from input m to output n, which follows:

$$\sum_{n-1}^{4} S_{m,n} = 1,\ 1 \leq m \leq 4. \tag{2.46}$$

Among all the 16 coefficients, four of them are representing the direct reflection of acoustic wave: $S_{1,1}$, $S_{2,2}$, $S_{3,3}$ and $S_{4,4}$, which are related with the acoustic reflection coefficient in Eq. (2.35) expressed as:

$$S_{m,m} = \left| \frac{\frac{R_{\text{grid}}}{R_{\text{grid}\pm1}} - 1}{\frac{R_{\text{grid}}}{R_{\text{grid}\pm1}} + 1} \right| = \left| \frac{\frac{\rho_{\text{grid}} c_{\text{grid}}}{\rho_{\text{grid}\pm1} c_{\text{grid}\pm1}} - 1}{\frac{\rho_{\text{grid}} c_{\text{grid}}}{\rho_{\text{grid}\pm1} c_{\text{grid}\pm1}} + 1} \right|, \quad 1 \leq m \leq 4, \tag{2.47}$$

where R_{grid} and $R_{\text{grid}\pm1}$ are the acoustic impedances of the scatterer's grid and its adjacent grid, ρ_{grid}, $\rho_{\text{grid}\pm1}$, c_{grid} and $c_{\text{grid}\pm1}$ are the respective densities and acoustic velocities. In homogeneous medium, $S_{m,m} = 0$ at each grid, while in heterogeneous medium $S_{m,m} \neq 0$ determined by the acoustic impedance mismatch.

In addition, another eight acoustic scattering coefficients ($S_{1,2}$, $S_{1,4}$, $S_{2,1}$, $S_{2,3}$, $S_{3,2}$, $S_{3,4}$, $S_{4,1}$, $S_{4,3}$) represent the acoustic scattering effect from one input port to its adjacent two output ports. Similarly, the remaining four acoustic scattering coefficients ($S_{1,3}$, $S_{2,4}$, $S_{3,1}$, $S_{4,2}$) are modeling the direct transmission of acoustic wave through the grid.

2.1.7 2D Simulation Comparison

To validate the 2D circuit network modeling of microwave acoustic interaction with biological tissues, circuit simulation and numerical simulation are conducted and compared in this section for three different scenarios. The simulation model is shown in Fig. 2.15a, where the 30 mm × 30 mm region is segmented by numerous small grids with d_{grid} = 0.15 mm grid size. Gaussian modulated microwave source with 1 GHz central frequency and 0.1 μs pulse-width is assigned to every unit

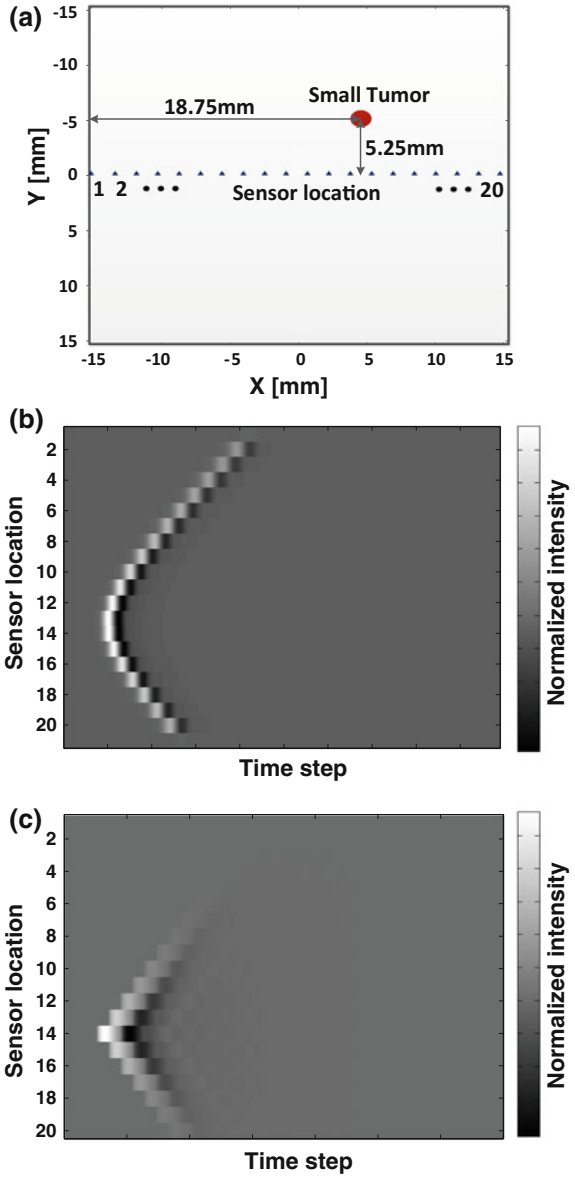

Fig. 2.15 **a** 2D simulation model of a single small tumor for both numerical and circuit simulation approaches. **b** The acoustic signals detected by 20 linear array acoustic sensors using numerical simulation, and **c** circuit simulations

source in the circuit model, assuming the homogeneous microwave illumination on the region of interest. A total amount of 20 acoustic sensors are aligned at $y = 0$ with 1.5 mm spacing. The propagation delay between adjacent grids is obtained by $delay = d_{\text{grid}}/c = 0.1$ μs, and the attenuation is calculated by $\alpha_{\text{grid}} d_{\text{grid}} = 0.01125$ dB in fat tissues.

2.1.7.1 One Tumor Case

In the first simulation case, one small tumor with 1.5 mm diameter is embedded at location (18.75 mm, 5.25 mm) in the homogeneous fat tissues, as shown in Fig. 2.15a. The physical and circuit parameters of the tumor remain same with the previous simulation in Sect. 2.4. The acoustic signals detected by the 20 sensors are shown in Fig. 2.15b, c, simulated by the numerical and circuit approaches. It shows a good agreement in terms of delay and attenuation information: when the sensor is nearer to the tumor source, the acoustic signal has shorter delay and stronger strength due to less attenuation.

2.1.7.2 Two Tumor Case

In the second simulation case, two tumors with different sizes and locations are included. A smaller tumor is located at (8.25 mm, 2.25 mm) with 1.5 mm diameter, and a larger tumor is located at (18.75 mm, 6 mm) with 3 mm diameter, as shown in Fig. 2.16a. The acoustic signals detected by the 20 sensors are shown in Fig. 2.16b, c, simulated by the numerical and circuit approaches. As expected, smaller tumor gives a narrower acoustic pulse width and reaches the sensor #6 in the earliest time with strongest magnitude; larger tumor gives a broader acoustic pulse width and reaches the sensor #14 first with longer delay time and weaker signal strength.

2.1.7.3 Acoustic Scattering Case

In the third simulation case, one tumor and one heterogeneous acoustic scatterer are embedded in the model to mimic the strong acoustic distortion during its propagation, which is shown in Fig. 2.17a. The small tumor is located at (18.75 mm, 5.25 mm) with 1.5 mm diameter, and the scatterer has a rectangular shape with 4.5 mm length and 1 mm width, which is located 2 mm below the small tumor. The acoustic velocity and density of the scatterer are set to be 4 mm/μs and 1500 kg/m^3, which are close to the bone in the human body. The acoustic signals detected by the 20 sensors are shown in Fig. 2.17b, c, simulated by the numerical and circuit approaches. Due to the existence of the strong acoustic scatterer, the acoustic signals detected by the sensors near the scatterer (#12–#16) are severely distorted in both numerical and circuit simulations. In this case, the circuit simulation performs very well when acoustic scatters exist, validating the proposed 2D circuit network to model the heterogeneous medium, which is a significant step closer to the real biological tissues, e.g. human breast.

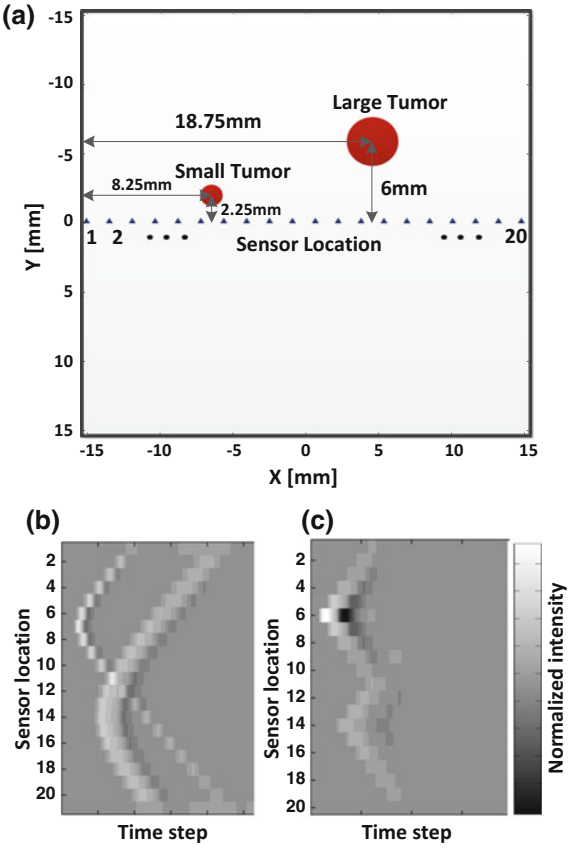

Fig. 2.16 **a** 2D simulation model of two tumors with different sizes for both numerical and circuit simulation approaches. **b** The acoustic signals detected by 20 linear array acoustic sensors using numerical simulation, and **c** circuit simulations

2.1.8 Discussion and Conclusion

As the pioneer attempt to build an electrical circuit model to simulate the microwave acoustic bio-effect, the study of this section provides an alternative simulation approach beyond conventional numerical methods. More importantly, the circuit modeling of the bio-effect enables, for the first time, the co-design and co-simulation of both the microwave acoustic bio-effect and the hardware circuit and system in a uniform circuit simulation environment such as SPICE. The setup of co-design and simulation is shown in Fig. 2.18, where the microwave acoustic bio-effect simulation and hardware simulation are seamlessly combined. By adjusting and optimizing the parameters of the microwave acoustic interaction block and microwave acoustic transceiver block simultaneously, the microwave acoustic imaging system will be developed with optimized performance for possible early-stage cancer detection.

To further enable the proposed circuit model for more realistic simulation scenarios, more complex circuit model will be developed from three aspects below:

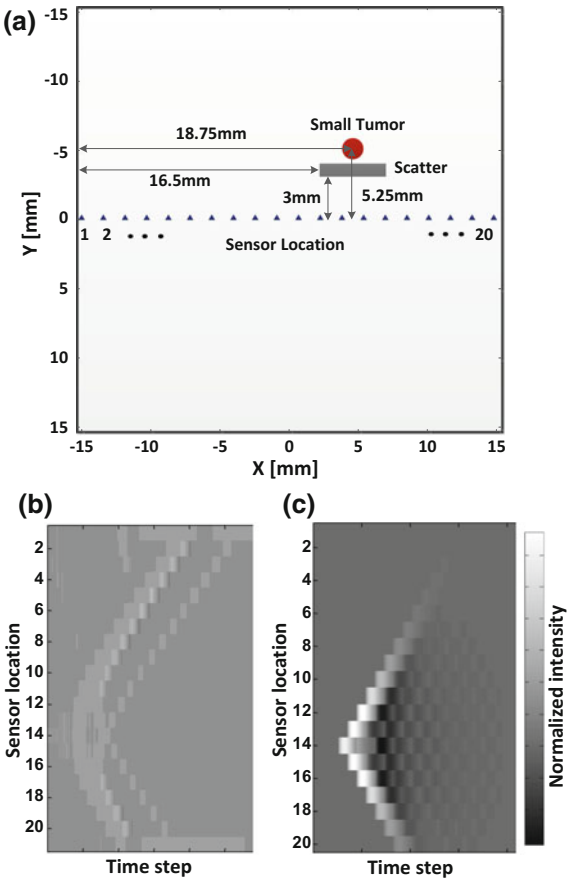

Fig. 2.17 **a** 2D simulation model of one tumor and one acoustic scatterer for both numerical and circuit simulation approaches. **b** The acoustic signals detected by 20 linear array acoustic sensors using numerical simulation, and **c** circuit simulations

1. To include the EM wave propagation and scattering effect, another set of circuit models should be developed to deal with the EM wave equations. Especially in heterogeneous tissue, EM wave diffraction and diffusion will result in uneven EM energy distribution and absorption, which is close to the real biological tissue environment.
2. To include the acoustic wave propagation suggested by the reviewer, more complex circuit structure should be developed to consider the acoustic wave diffraction, nonlinearity and frequency dependent attenuation.
3. To enable the simulation in 3D, the whole simulation structure should be extended in 3D. By doing so, the computational time will be significantly increase, so that more efficient circuit structure should be proposed to achieve fast simulation for complex 3D structure.

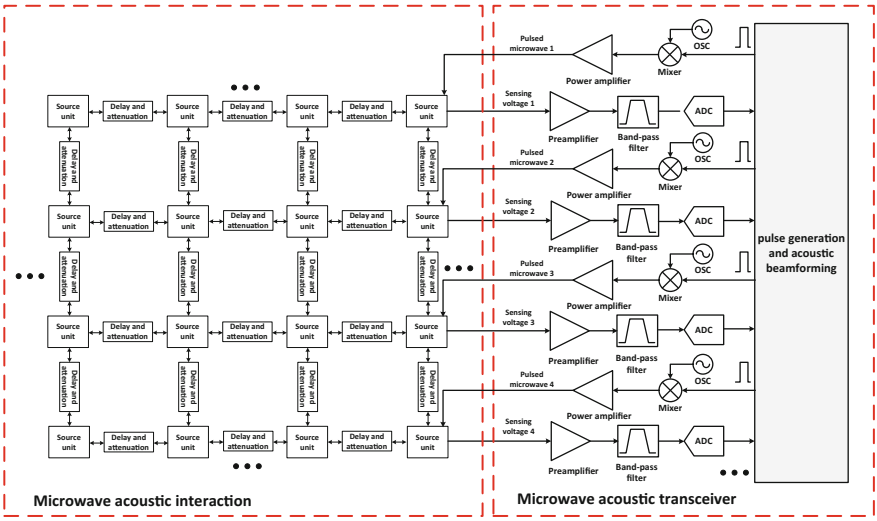

Fig. 2.18 Co-design and simulation of microwave acoustic bio-effect and transceiver circuit for microwave acoustic imaging system development in a uniform circuit simulator. Pulsed microwave is generated by mixing the pulse signal with microwave source from the oscillator, and fed into the microwave input port of the unit source. Sensing voltage from the unit source is acquired by the preamplifier, bank-pass filter and ADC to perform the image reconstruction in digital domain. Reprinted from Ref. [2] with permission from American Association of Physicists in Medicine

In this section we have proposed an equivalent circuit model to simulate the microwave acoustic interaction with biological tissues, a faster system-level simulation using SPICE is enabled. Then based on the circuit model, a characteristic gain to quantitatively evaluate the performance of microwave acoustic imaging system is proposed, utilizing the transducer gain derived from the equivalent circuit modeling. This characteristic gain is also a more sensitive indicator than microwave scattering related S_{11} and microwave absorption related S_{21} alone in characterizing the tumor tissues even when in their early stage. It is easy to derive the design guideline for the optimization of a microwave acoustic imaging system for cancer detection. Numerical simulation and experimental measurement are conducted to verify the validity of the equivalent circuit model. To extend the proposed circuit simulation approach for a more realistic situation to consider acoustic heterogeneity, a 2D circuit network is further proposed comprising source unit and acoustic channel blocks. Simulation results of numerical and circuit approaches agree well for tumors with different sizes and strong acoustic scattering cases. In summary, with the proposed 2D circuit network model, co-simulation fusing microwave acoustic bio-effect and hardware development is becoming possible in a uniform circuit simulator. Hence global optimization becomes feasible for the integrated circuit (IC) implementation of the microwave acoustic imaging system for earlier-stage cancer detection.

2.2 EM-Acoustic Phasoscopy Sensing and Imaging

In this section, a new concept "phasoscopy" will be introduced to correlate scattered EM wave and EM absorption induced acoustic wave based on energy conservation principle. The EM-acoustic phasoscopy fuses the contrast of EM scattering imaging (microwave imaging, optical imaging, etc.) and EM-acoustic imaging (Thermoacoustic/Phtoacoustic imaging) to achieve super-contrast performance. Firstly the microwave-acoustic phasoscopy is analyzed in detail for 4 kinds of porcine tissue characterization. Then photoacoustic phasoscopy super-contrast imaging is demonstrated on phantom and ex vivo tissues based on raster scanning. The phasoscopy imaging and tomography could potentially be a powerful imaging modality to fuse EM scattering imaging and EM-acoustic imaging. The results of this section have been published in *Applied Physics Letters* [11, 12].

2.2.1 *Microwave-Acoustic Phasoscopy for Tissue Characterization*

Shown in Fig. 2.19a, the interactions between microwave and biological tissue include microwave scattering at the interface due to dielectric property difference, and microwave energy absorption in the lossy tissue with high electrical conductivity leading to thermal expansion and acoustic wave generation. For the sake of simplicity, the following analysis is based on the plane wave model, propagating in one direction, and assuming that tissue is a block of materials with thickness d_0 and cross-sectional area p, shown in Fig. 2.13b. It has specific complex permittivity $\varepsilon_r = \varepsilon' - j\varepsilon''$, where ε', ε'' are the real and imaginary parts of the complex

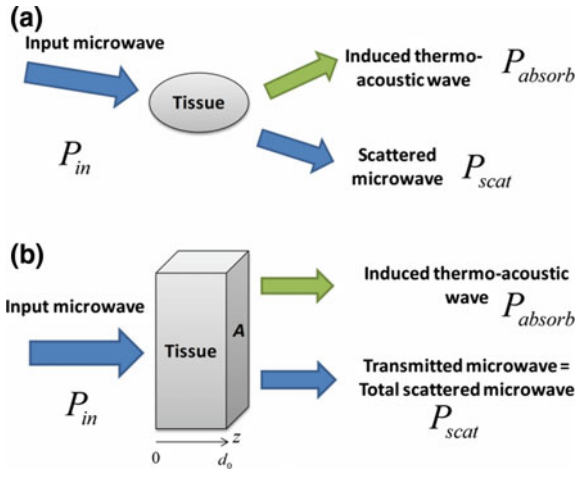

Fig. 2.19 **a** Physical principle of microwave scattering and absorption interaction with biological tissue and **b** simplified planar model for analysis

permittivity. The total scattered microwave signal is represented by the transmitted microwave signal in the simplified planar model. Starting from Maxwell equation, the wave equation to be solved is:

$$\nabla^2 E + \gamma^2 E = 0, \tag{2.48}$$

E is electrical field and:

$$\gamma^2 = \omega^2 \mu \varepsilon' (1 - j \tan\theta), \tag{2.49}$$

where ω is the angular frequency, μ is permeability, and $\tan\theta$ is loss tangent expressed as $\tan\theta = \sigma/\omega\varepsilon'$ with conductivity σ . A solution to Eq. (2.48) is $E = E_0 e^{-j\gamma z}$ with input electrical intensity E_0. Assuming the complex parameter $\gamma = \beta - j\alpha$ where $\alpha = \omega\sqrt{\mu\varepsilon'}\sqrt{\frac{1-\cos\theta}{2\cos\theta}}$ and $\beta = \omega\sqrt{\mu\varepsilon'}\sqrt{\frac{1+\cos\theta}{2\cos\theta}}$, the electrical field can be expressed as:

$$E = E_0 e^{-\alpha z} e^{-j\beta z}, \tag{2.50}$$

and the magnetic field can be found from $\nabla \times E = -j\omega\mu H$:

$$H = \frac{\beta - j\alpha}{\omega\mu} E_0 e^{-\alpha z} e^{-j\beta z}. \tag{2.51}$$

Then the existing and absorbed microwave power could be expressed as:

$$P_e = \frac{1}{2}\iint_S (E \times H^*) \cdot ds = \frac{1}{2}\iint_S E_0^2 \frac{\beta + j\alpha}{\omega\mu} e^{-2az} \cdot ds, \tag{2.52}$$

$$P_{absorb} = \frac{1}{2}\iiint_V \sigma |E|^2 dv = \frac{1}{2}\iiint_V \sigma E_0^2 e^{-2\alpha z} dv. \tag{2.53}$$

Thus the input microwave power (real) is the existing power at $z = 0$:

$$P_{in} = Re[P_e|_{z=0}] = \frac{A}{2} E_0^2 \frac{\beta}{\omega\mu}. \tag{2.54}$$

The scattered (transmitted) microwave power (real) is the existing power at $z = d_0$:

$$P_{scat} = Re[P_e|_{z=0}] = \frac{A}{2} E_0^2 \frac{\beta}{\omega\mu} e^{-2\alpha d_0}, \tag{2.55}$$

and the power absorbed by the tissue is:

$$P_{absorb} = \frac{1}{2}\iiint_V \sigma E_0^2 e^{-2\alpha z} dv = \frac{A}{4\alpha}\sigma E_0^2 (1 - e^{-2\alpha d_0}). \tag{2.56}$$

Then, energy conservation is verified and shown below represented by averaged powers:

$$\begin{aligned} \frac{P_{in} - P_{scat}}{P_{absorb}} &= \frac{\frac{A}{2}E_0^2\frac{\beta}{\omega\mu} - \frac{A}{2}E_0^2\frac{\beta}{\omega\mu}e^{-2\alpha d_0}}{\frac{A}{4\alpha}\sigma E_0^2(1 - e^{-2\alpha d_0})} = \frac{\frac{A}{2}E_0^2\frac{\beta}{\omega\mu}(1 - e^{-2\alpha d_0})}{\frac{A}{4\alpha}\sigma E_0^2(1 - e^{-2\alpha d_0})} \\ &= \frac{2\alpha\beta}{\sigma\omega\mu} = \frac{2\omega^2\mu\varepsilon'\frac{\sqrt{1-\cos^2\theta}}{2\cos\theta}}{\sigma\omega\mu} = \frac{\omega\varepsilon'\tan\theta}{\sigma} = 1, \\ \therefore \bar{P}_{in} &= \bar{P}_{scat} + \bar{P}_{absorb}, \end{aligned} \tag{2.57}$$

indicating that the summation of averaged scattered and absorbed microwave power equals to the constant input microwave power, where $\bar{P}$ represents the averaged power. Furthermore, acoustic signal could be induced through microwave energy absorption of the tissue, following localized heating and thermo-elastic expansion. When heating time is treated as a delta function $\delta(t)$, the initial acoustic pressure of the homogeneous tissue could be expressed as [13]:

$$p_0(t) = \Gamma\frac{\bar{P}_{absorb}}{A \cdot d_0}\delta(t), \tag{2.58}$$

where $\Gamma = bc^2/C_P$ is the Gruneisen coefficient, b is the isobaric volume expansion coefficient, C_P is the specific heat and c is acoustic velocity in biological tissue. The acoustic signal propagates outwards in all directions and only one portion of the acoustic energy is detected by the ultrasound transducer. Considering all the factors including finite thermoacoustic (TA) conversion efficiency, incomplete acoustic detection and transducer response, we use p $(0 < p < 1)$ as the conversion coefficient, representing the averaged power conversion ratio of the detected acoustic power (simply expressed as $\bar{p}^2_{acoustic}$) from the absorbed microwave power $\bar{P}_{absorb}$. Similarly, because only part of the scattered microwave signal could be collected by the receiver antenna, the ratio between the averaged received scattering microwave power expressed as $\bar{p}^2_{scat}$ and the total averaged scattered microwave power $\bar{P}_{scat}$ is represented as $q(0 < q < 1)$. Then we have $\bar{p}^2_{acoustic} = p\bar{P}_{absorb}$ and $\bar{p}^2_{scat} = q\bar{P}_{scat}$. Substitute above parameters to energy conservation Eq. (2.57), we have:

$$\frac{\bar{p}^2_{acoustic}}{p\bar{P}_{in}} + \frac{\bar{p}^2_{scat}}{q\bar{P}_{in}} = 1. \tag{2.59}$$

It is predicted that for a specific tissue, the detected acoustic signal and microwave signal by the ultrasound transducer and receiver antenna respectively, are

supposed to follow an ellipse equation with acoustic and microwave semi-axes $\sqrt{p\bar{P}_{in}}$ and $\sqrt{q\bar{P}_{in}}$.

According to Eq. (2.56), tissues with different conductivity σ will have different microwave absorption P_{absorb} and detected acoustic power, meanwhile $\bar{p}^2_{scat} = q\bar{P}_{scat}$ will vary in opposite direction based on Eq. (2.57). Therefore, tissues with different conductivity σ will fall on different locations of the ellipse. Drawing the ellipse with three tissues in Fig. 2.20, it is clearly shown that phase information $(\theta_1, \theta_2, \theta_3)$ is capable of differentiating tissues by correlating both acoustic and microwave signals, rather than conventional methods evaluating either one of them. The phase contrast of the MAPC can be derived as:

$$1+\frac{\Delta\theta}{\theta}=\frac{\arctan\left(\frac{\bar{p}_{acoustic}+\Delta\bar{p}_{acoustic}}{\bar{p}_{scat}+\Delta\bar{p}_{scat}}\right)}{\arctan\left(\frac{\bar{p}_{acoustic}}{\bar{p}_{scat}}\right)}\approx\frac{\left(\frac{\bar{p}_{acoustic}+\Delta\bar{p}_{acoustic}}{\bar{p}_{scat}-\Delta\bar{p}_{scat}}\right)}{\left(\frac{\bar{p}_{acoustic}}{\bar{p}_{scat}}\right)}(1-\varphi)\approx\left(\frac{1+\frac{\Delta\bar{p}_{acoustic}}{\bar{p}_{acoustic}}}{1-\frac{\Delta\bar{p}_{scat}}{\bar{p}_{scat}}}\right)$$
$$\approx\left(1+\frac{\Delta\bar{p}_{acoustic}}{\bar{p}_{acoustic}}\right)\left(1+\frac{\Delta\bar{p}_{scat}}{\bar{p}_{scat}}\right), \tag{2.60}$$

where φ is infinitesimal of higher order after Taylor expansion. According to Eq. (2.60), correlated phase contrast is clearly enhanced by multiplication of microwave contrast $(1+\Delta\bar{p}_{scat}/\bar{p}_{scat})$ and acoustic contrast $(1+\Delta\bar{p}_{acoustic}/\bar{p}_{acoustic})$, which is a kind of non-linear amplification. Therefore the proposed MAPC method is potentially powerful in tissue characterization with higher sensitivity and robustness.

The experimental setup for MAPC is shown in Fig. 2.21. A microwave generator (SMBV100A, Rohde & Schwarz) is used to provide 440 MHz continuous microwave, which is mixed with a pulse signal having 2 μs pulse duration and 100 Hz repetition rate coming from function generator (33250A, Agilent) by

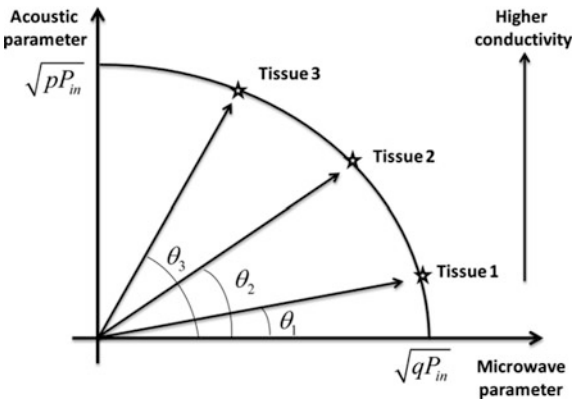

Fig. 2.20 Microwave-acoustic phasoscopy for three tissues with different conductivity, *horizontal axis* represents microwave signal and *vertical axis* represents acoustic signal

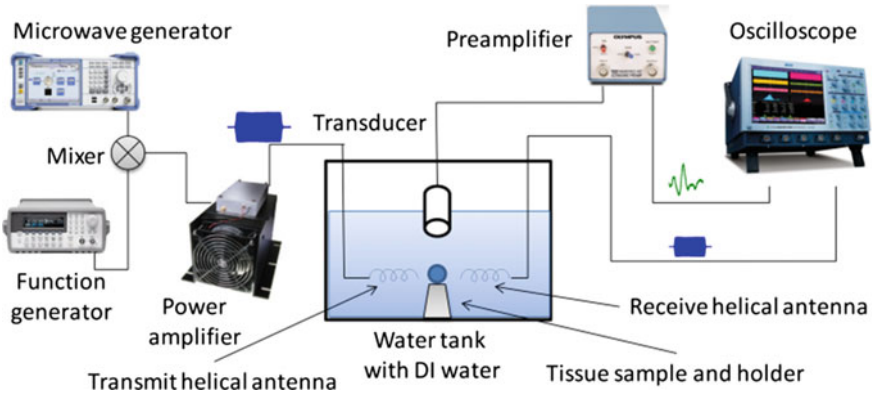

Fig. 2.21 Experimental setup for microwave-acoustic phasoscopy. Reprinted from Ref. [12] with permission from AIP Publishing LLC

frequency mixer (ZX05-1HW-S+, Mini-Circuits). Through a microwave power amplifier (ZHL-100 W-GAN+, Mini-Circuits), the pulse-modulated microwave signal is amplified up to 100 W peak power and fed into a custom-designed helical antenna operating at 440 MHz. Scattered microwave signal is received by another helical antenna placed at the other side. Meanwhile, the thermoacoustic signal due to the microwave absorption is also collected by a wideband ultrasound transducer (V323-SU, Olympus) with 2.25 MHz central frequency, which is sensitive enough to detect acoustic wave with frequencies ranging from several hundred kHz to 5 MHz, followed by an ultrasound preamplifier (Model 5662, Olympus). Both scattered microwave signal and thermoacoustic signal are recorded with a digital oscilloscope (WaveMaster 8000A, Lecroy) at 5 G samples/s rate. In the water tank, both microwave antennas and ultrasound transducer are immersed in the de-ionized water. Tissue sample is placed near the end of transmit helical antenna for maximum microwave illumination.

In order to generate and verify the proposed MAPC principle, three kinds of porcine tissues (kidney, liver, fat) with different conductivity at 440 MHz are prepared. According to previous literatures [14–16], the conductivity values of above biological tissues are listed in Table 2.6. Made in small round shape with 5 mm diameter and wrapped by ultrathin polyethylene film, the biological tissue is placed close to both antennas and transducer. Due to fast propagation speed of electromagnetic wave in water and lossy small size tissue sample, scattered microwave signal is received immediately after illumination, ignoring the much weaker multi-scattering microwave. Incident microwave source is shown in Fig. 2.22a, a microwave signal used for calibration is firstly recorded with no tissue sample placed, and subtracted by the recorded microwave signal with tissue sample to decouple the interference of direct-link microwave from transmitted antenna and reflected microwave by surrounding environment such as water tank wall, sample

holder etc. After envelope extraction and low-pass filtering, calibrated microwave signals for these three kinds of tissues are shown in Fig. 2.22b. Averaged 300 times by the oscilloscope and subtraction of background noise, the recorded acoustic signal triggered by transmitted microwave pulse propagates through water media, which last about 30 μs, are shown in Fig. 2.22c. It is obvious to see that the amplitude (energy) of the received microwave envelope and acoustic signal are varying in opposite trend, i.e., the more microwave energy absorbed to induce acoustic signal, the less microwave energy scattered by the tissue.

By applying proper normalization scheme to the extracted microwave and acoustic parameters, the MAPC ellipse is built in Fig. 2.23a, normalized parameters

Table 2.6 Conductivity of three different tissues at 440 MHz (S/m) [4]

Fat	Liver	Kidney
0.0418	0.6704	1.1209

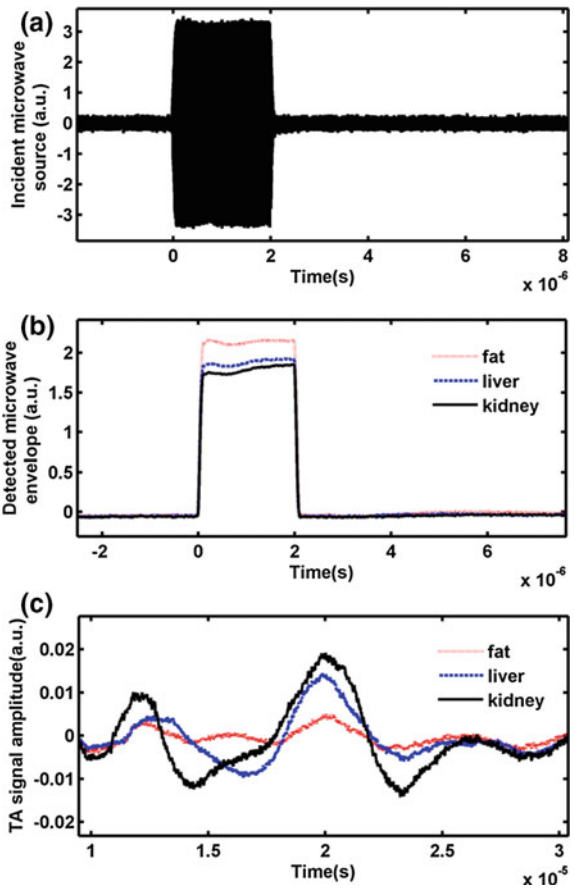

Fig. 2.22 **a** Incident microwave source, **b** microwave signal detected by receive antenna and **c** thermoacoustic signal detected by ultrasound transducer. Reprinted from Ref. [12] with permission from AIP Publishing LLC

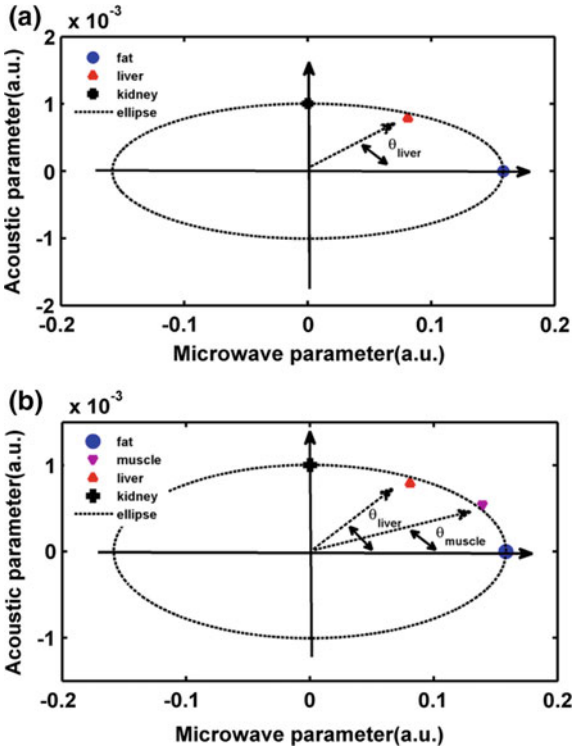

Fig. 2.23 **a** Established microwave-acoustic phasoscopy (MAPC) and **b** tissues with different absorption rate are characterized on the MAPC. Reprinted from Ref. [12] with permission from AIP Publishing LLC

of the three tissues are calculated and marked on the MAPC ellipse. Three tissues with different conductivity are well separated in the phase domain on the MAPC. The Fat and Kidney tissue are normalized to be $\theta_{fat} = 0°$ and $\theta_{kidney} = 90°$. Liver tissue is characterized by the phase of $\theta_{liver} = 42.42°$, marked on the ellipse with negligible deviation due to the experimental variation.

In the next step, porcine muscle tissue is also characterized using the proposed MAPC. Shown in Fig. 2.23b, it is with phase $\theta_{muscle} = 21.16°$, revealing that its microwave absorption rate is between fat and liver, and well differentiated on the MAPC, and similar conclusion is drawn by other methods [17]. Based on these experiments, we can estimate the phase sensitivity with regard to tissue's conductivity is averagely 8.34° per 0.1 S/m. In addition, applying the MAPC normalization scheme (step 3, 4), tissues with microwave absorption rate larger than kidney or smaller than fat can also be characterized by different phase in second and fourth quadrant respectively (the third quadrant remains blank based on the current normalization scheme). Proved by Eq. (2.57) and verified by the experiment, we can conclude the proposed MAPC can characterize all the biological tissues by its microwave-acoustic phase.

Compared with current thermoacoustic characterization by tissue's EM absorption [18], the proposed MAPC evaluates both scattered microwave signal

and induced thermoacoustic signal simultaneously. Phase information is extracted for different tissues rather than conventional amplitude or spectrum evaluation only [19]. Such multi-mode acquisition (EM and acoustic wave) is able to provide coherent enhancement related to EM absorption and scattering of the same tissue only, as well as suppression of variation and noise due to non-coherence characteristics of their EM and acoustic waves. Therefore, the MAPC is supposed to be more sensitive and robust for tissue characterization.

2.2.2 *Photoacoustic Phasoscopy Super-Contrast Imaging*

By applying the phasoscopy concept to PA imaging, we could achieve the PA phasoscopy (PAPS) by collecting both scattered photons and thermoelastically induced acoustic wave. Based on the PA phasoscopy concept, here we propose a novel imaging approach, termed PA phasoscopy (PAPS) imaging, which could be achieved by receiving both laser-induced PA wave and scattered photons simultaneously under the same laser illumination, and calculating the phase indicator $\tan\theta = p_{acoustic}/p_{scat}$ point by point to form a PA phasoscopy image. Then the intensity at each point fuses both optical absorption and scattering properties, and is expected to give enhanced image contrast than conventional photoacoustic imaging based on optical absorption only. Next we will experimentally demonstrate the super-contrast PAPS imaging on both phantom and ex vivo tissues.

The experimental setup is shown in Fig. 2.24. A Q-switched pulse laser (FDSS 532-1000, CryLaS, GmbH) with 1 mJ pulse energy, 1.8 ns pulse width and 532 nm

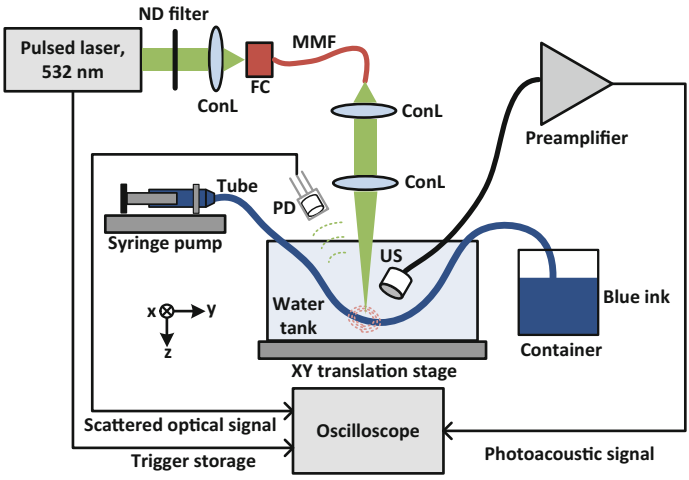

Fig. 2.24 Experimental setup of the proposed PAPS imaging. *ND* neutral density; *ConL* condenser lens; *FC* fibre coupler; *MMF* multi-mode fibre; *PD* photodiode; *US* ultrasound transducer. Reprinted from Ref. [11] with permission from AIP Publishing LLC

wavelength is used to provide the collimated light source, which is attenuated by a neutral density filter (NDC-50C-2 M, Thorlabs) and focused into a multi-mode fibre (MHP550L02, Thorlabs) coupler by a condenser lens (LB1471, Thorlabs). The output of the fibre is focused by a pair of lens onto the vessel-mimicking phantom, which is made of a silicone tube (3 mm diameter) filled with blue ink and pumped by a syringe. The phantom is immersed in water for optimum light transparency and acoustic coupling. A focused ultrasound transducer (V303-SU, Olympus) with 1 MHz central frequency is used to detect the PA signal, followed by 54 dB gain preamplifier (5662, Olympus). At the same time, the scattered photons are collected by a photodiode (DET10A, Thorlabs). Both the PA signal and scattered photon signal are averaged 100 times, recorded by a digital oscilloscope (WaveRunner 640Zi, LeCroy) with 5 GHz sampling rate and sent to a PC for post-processing. To acquire an image, the water tank is moved linearly by the XY translation stage (XYR1, Thorlabs) for raster scanning.

To get the cross-sectional image of the vessel-mimicking phantom, the translation stage is scanned 10 mm in X-axis with 0.5 mm step size. The received PA signals $p_{acoustic}$ are subjected to the low-pass filtering and Hilbert transformation for the envelope extraction, which are then mapped to form the PA image shown in Fig. 2.25a. On the other hand, the phasoscopy signals are obtained by extracting the phase $\tan\theta = p_{acoustic}/p_{scat}$ and are mapped to form the phasoscopy image, as shown in Fig. 2.25b. To fairly compare the imaging contrast, the intensities of both images are normalized to the same scale, which is clearly shown in Fig. 2.25c. As expected, the intensities of PA signal and scattered photon signal are changing on the opposite way based on energy conservation principles, i.e. when more light is absorbed, less light is scattered, and vice versa. The imaging results clearly show that the phasoscopy contrast $\tan\theta = 212:1$ (red solid line) fusing optical absorption and scattering contrasts, is more than 9 times larger than the optical absorption contrast (blue dashed line), i.e. the PA imaging contrast. The imaging results prove the feasibility of PAPS imaging to achieve super-contrast performance than conventional PA imaging based on optical absorption only.

To further validate the phasoscopy imaging approach, ex vivo porcine tissues are prepared with different optical absorption and scattering properties at fat and muscle parts. As shown in Fig. 2.26a, the tissue sample is scanned 6 mm across the solid line covering three different parts denoted as 1, 2, 3. After low-pass filtering, envelop extraction and contrast scale normalization, the conventional PA imaging and proposed PA phasoscopy imaging results are shown in Fig. 2.26b, c. It is clearly shown that the image contrast between fat and muscles parts reconstructed by the PAPS imaging in Fig. 2.26c is much better than the PA imaging in Fig. 2.26b. The image contrast comparison is shown in Fig. 2.26d, where the intensities along the dashed and dotted lines in Fig. 2.26b, c are plotted. It shows that the contrast of the PAPS imaging (red solid line) is more than two times larger than the contrast of conventional PA imaging based on optical absorption only (blue dashed line).

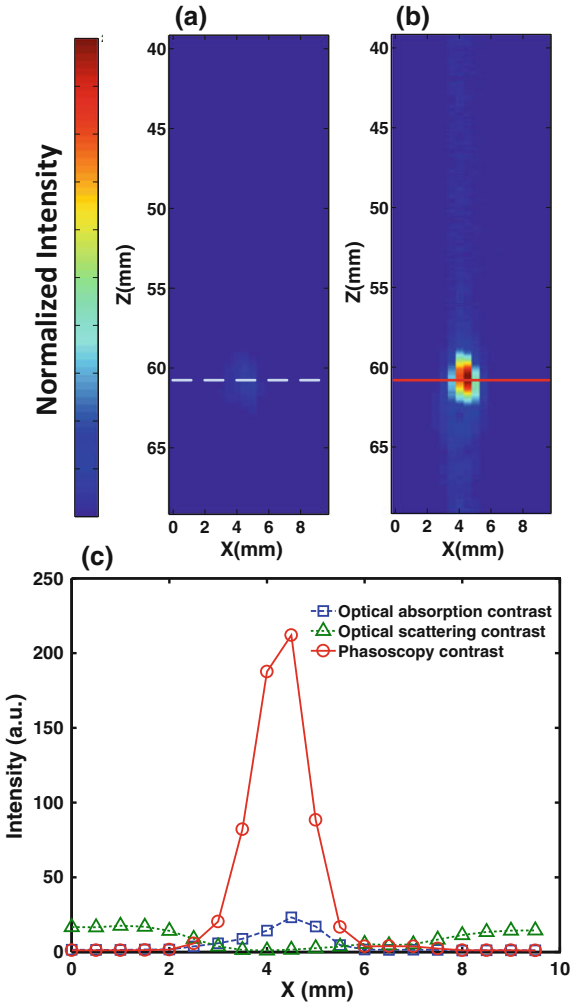

Fig. 2.25 **a** Conventional PA imaging result and **b** super-contrast PAPS imaging result of a vessel-mimicking phantom's cross-section. **c** The intensity along the *dashed* and *solid lines* in (**a**) and (**b**) to show the contrast comparison. Reprinted from Ref. [11] with permission from AIP Publishing LLC

Existing dual-modal PA imaging approaches include PA plus ultrasound [8, 20–22], PA plus OCT [23, 24], PA plus DOT [25, 26], and so on. All the above approaches are separately processing the PA signals and ultrasound/photon signals to reconstruct two individual and complementary images, where the intrinsic correlation between them has not been fully explored. The key difference between the proposed PAPS imaging and existing approaches is: PAPS imaging correlates the detected PA signal and scattered phonons to deliver ONE image fusing both optical absorption and scattering properties of the same object based on energy conservation principle and phasoscopy concept, rather than two separate images in conventional dual-modal PA imaging approaches. Moreover, compared with the conventional PA imaging suffering the laser intensity fluctuation, the proposed

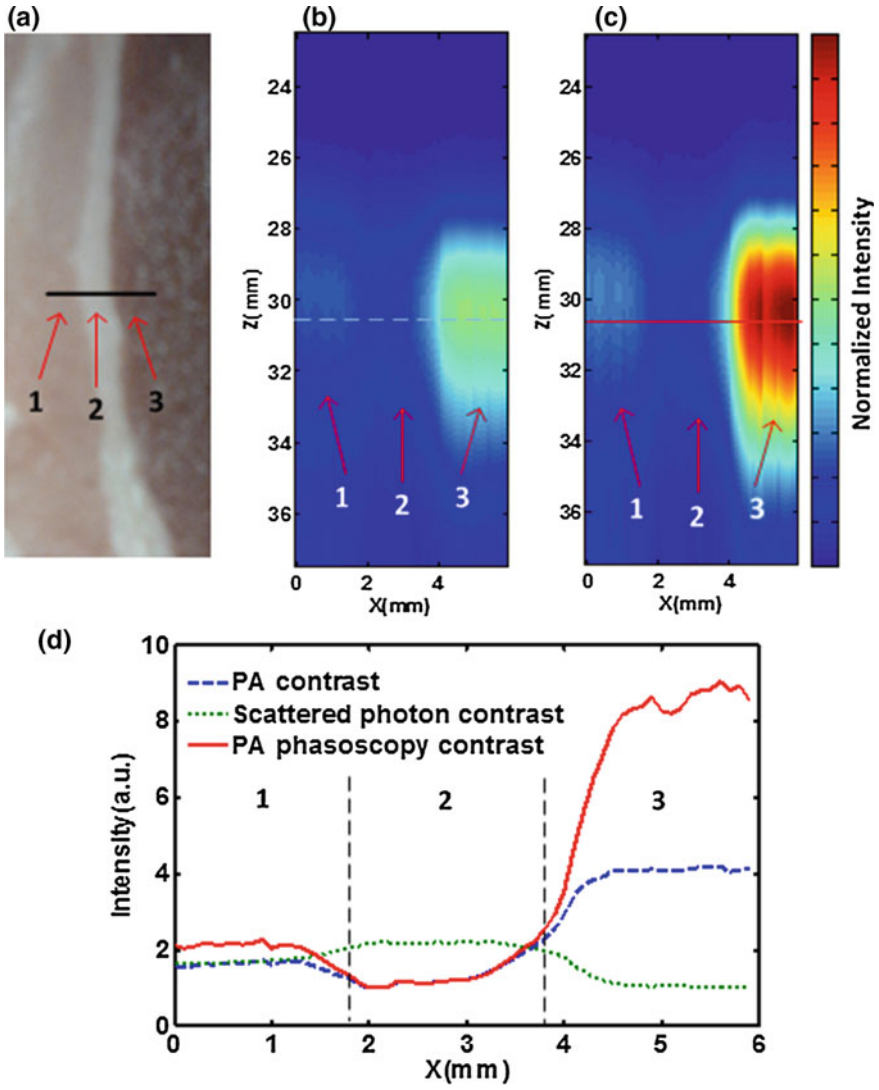

Fig. 2.26 **a** Photograph of the ex vivo porcine tissues with three different fat and muscle parts. The *black line* is the scanning axis-X with 6 mm range. **b** The conventional PA imaging, and **c** proposed PAPS imaging results with same contrast scale. **d** The intensity across the *dashed* and *solid lines* in (**b**) and (**c**) to show the image contrast comparison. Reprinted from Ref. [11] with permission from AIP Publishing LLC

PAPS imaging is inherently immune to the laser and system variations due to the reason that: when input laser intensity fluctuates, both the PA signal $p_{acoustic}$ and scattered photons p_{scat} fluctuate in the same way, leading to the constant phase: $\theta = \arctan(p_{acoustic}/p_{scat})$.

In conclusion, the concept of PA phasoscopy is briefly introduced and PA phasoscopy super-contrast imaging is proposed and experimentally demonstrated in this section. It correlates both optical absorption and scattering based on energy conservation to achieve super-contrast performance, rather than conventional PA imaging based on optical absorption only or optical imaging based on scattered photons only. In vivo 3D phasoscopy imaging will be studied for both small animal and clinical applications in the future.

2.3 EM-Acoustic Resonance Effect and Characterization

In this section, an interesting physical phenomenon, termed "EM-Acoustic resonance effect" is proposed for both microwave-induced thermoacoustic and laser-induced photoacoustic scenarios. Being different from conventional thermoacoustic/photoacoustic effect triggered by pulsed EM source, the proposed EM-acoustic resonance is induced by multi-pulse EM source to hit the intrinsic resonance frequency of the object (e.g. biological tissue) for maximum signal amplitude. Equivalent electrical circuit model is proposed to model the effect, as well as experimental validation on biological tissues. Furthermore, the photoacoustic resonance spectroscopy is elaborated as a useful characterization tool to probe both optical absorption and mechanical resonance properties of the biological tissues. The results of this section have been published in *Applied Physics Letters* [27] and *Journal of Biomedical Optics* [28].

2.3.1 Thermoacoustic Resonance Effect and Circuit Modeling

Microwave-induced thermoacoustic (TA) effect refers to the thermal expansion of tissue leading to the generation of an acoustic transient following the microwave illumination introduced in Chap. 1. Based on the TA effect, microwave-induced thermoacoustic tomography (TAT) has been proposed and applied to ex vivo and in vivo medical imaging, such as breast cancer detection, providing high microwave absorption contrast and high acoustic resolution simultaneously. Existing prototypes of TAT experiments are using single microwave pulse with a high peak power of up to 10 kW and above to illuminate biological tissue. Thereby, a wideband thermoacoustic signal is induced inside the tissue sample, and detected by ultrasound transducers for image reconstruction. A major obstacle for current prototypes is that high peak power microwave sources are bulky and expensive for an envisioned portable medical imaging device for on-site diagnosis.

In this section we report the resonance response of the tissue induced by multiple pulses of the microwave source. The response of the tissue can be modelled with a

damped harmonic oscillator, i.e. a series RLC circuit. Once the multi-pulse microwave source matches the resonance frequency of the biological tissue, the signal-to-noise ratio (SNR) of thermoacoustic resonance (TAR) signal is enhanced significantly, and narrowband characteristic is also achieved. Additionally, we propose a coherent demodulation scheme to obtain depth-resolved information for a future imaging implementation of the technique.

The basics of microwave-induced thermoacoustic effect is well established in literature. Very similar to the photoacoustic effect induced from pulsed lasers, biological tissue illuminated by pulsed microwave will absorb some of the electromagnetic (EM) energy. This results into heating and thermal expansion of the tissue, as sketched in Fig. 2.27a. Under the constrain that the tissue absorber (here about 5 mm in diameter) is small compared to the microwave wavelength, it acts as a point source, and the acoustic pressure emitted, $p(t)$, can be described through a forced oscillator [3, 29]:

$$\frac{\partial^2}{\partial t^2}p(t) + a^2\frac{\xi + \frac{4}{3}\eta}{\rho}\frac{\partial}{\partial t}p(t) + a^2c^2p(t) = \Gamma\frac{\partial H(t)}{\partial t}, \tag{2.61}$$

where a is the propagation phase constant, ρ is the tissue density, η is the shear viscosity, ξ is the bulk viscosity, and c is the acoustic velocity in tissue. Γ is the Gruneisen constant expressed as $\Gamma = \beta c^2/c_p$, where β is the thermal expansion

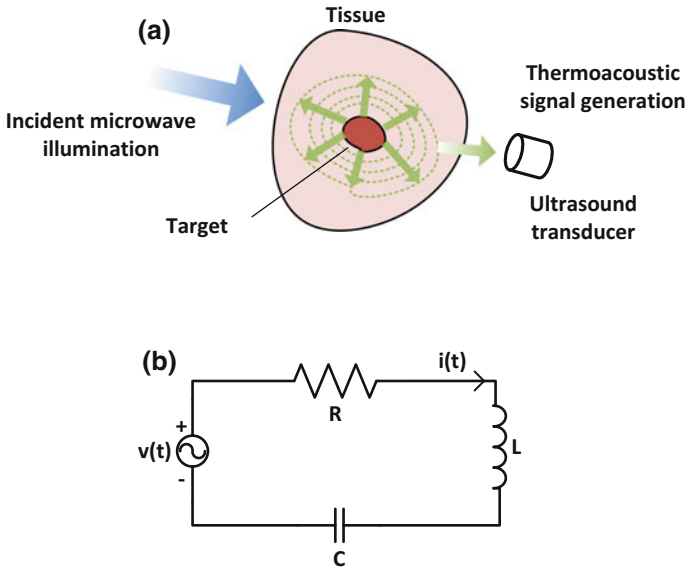

Fig. 2.27 **a** Diagram of thermoacoustic effect induced by microwave illumination, and **b** its equivalent series RLC resonance circuit model driven by voltage source v(t). Reprinted from Ref. [30] with permission from AIP Publishing LLC

coefficient, and c_p is the constant pressure heat capacity per unit mass. $H(t) = \sigma \bar{E}^2(t)$ is the heating function of microwave illumination, where σ is the conductivity of tissue, and $\bar{E}(t)$ is the short-time averaged electrical field strength.

In Eq. (2.61), the acoustic pressure follows a second order differential equation with source term $\Gamma \frac{\partial H(t)}{\partial t}$, which is electrically analogue to a series RLC circuit, where the pressure, $p(t)$, is replaced with a time-dependent current $i(t)$, and the heat source $H(t)$ with voltage source $v(t)$, see Fig. 2.27b:

$$\frac{\partial^2}{\partial t^2} i(t) + \frac{R}{L}\frac{\partial}{\partial t} i(t) + \frac{1}{LC} i(t) = \frac{1}{L}\frac{\partial}{\partial t} v(t), \tag{2.62}$$

where the resistance R, inductance L, and capacitance C represent the tissue properties of Eq. (2.61). Next, we discuss the electrical analogue and extraction from the measurement for the parameters. Assuming that the voltage source is a cosine tone burst driven at a frequency ω_R, the response of $i(t)$ at steady state can be expressed as:

$$i(t) = \left|I_p\right| \cos(\omega_R t + \theta_P), \tag{2.63}$$

where θ_P is the phase shift and I_P is the complex transient current expressed as:

$$I_p = \frac{V}{R + j\omega L + \frac{1}{j\omega C}} = \frac{V}{R + j\left(\omega L - \frac{1}{\omega C}\right)}. \tag{2.64}$$

The magnitude of I_P will be maximized at the resonance frequency ω_0:

$$\omega_R = \omega_0 = \frac{1}{\sqrt{LC}}. \tag{2.65}$$

We can relate the bandwidth (BW) and the quality factor (Q) with L, R, and C as:

$$BW = \frac{R}{L} \tag{2.66}$$

$$Q = \frac{\omega_0}{BW} = \frac{\omega_0 L}{R} = \frac{1}{R}\sqrt{\frac{L}{C}}. \tag{2.67}$$

Thus we expect that the thermoacoustic response of the tissue at steady state will follow the envelope frequency of the microwave source, and once these envelope hits the resonance frequency a resonant response should be observed. This resonance frequency of the tissue is related to the electrical analogue: $\omega_{tissue} = \omega_0 = 1/\sqrt{LC} = ac$. We now demonstrate that this resonance is sufficiently strong to be observed experimentally.

The experimental setup which allows to compare the thermoacoustic (TA) and thermoacoustic resonance (TAR) effect is shown in Fig. 2.28. A microwave generator (SMBV100A, Rohde & Schwarz) generates single and multi-pulse microwave source for the observation of TA and TAR effects, respectively. For the latter, the amplitude shift keying configuration is used together with a serial digital input. The microwave source is amplified up to 100 W with a microwave power amplifier (ZHL-100W-GAN+, Mini-Circuits). Considering the tissue absorption characteristics with respect to microwave frequencies, we choose 440 MHz as the carrier frequency. The pulsed microwave signal is then fed into a custom-designed helical antenna operating at 440 MHz. The thermoacoustic response of the tissue is detected with an ultrasound transducer (V323-SU, Olympus), fed into a preamplifier (54 dB gain, Model 5662, Olympus) and recorded with a digital oscilloscope (WaveMaster 8000A, Lecroy) at 500 MHz sampling rate. Later, they are transferred into a computer for further signal processing. In the tank, both the helical antenna and the ultrasound transducer are immersed in mineral oil ($\varepsilon_r = 2.1, \sigma \approx 0$). Muscle tissue samples ($\varepsilon_r = 56.8, \sigma \approx 0.8$) are shaped into small balls of 5 mm diameter, and placed close to the end of the helical antenna.

Applying the same peak power source for every pulse in the experiment, the thermoacoustic signals are detected by both the single pulse and the multi-pulse microwave illumination. Six continuous pulses (TAR) are transmitted for multi-pulse illumination, followed by a single pulse illumination (TA) afterwards, as shown in Fig. 2.29a. All pulses have a pulse widths of 3.67 μs. Figure 2.29b depicts the acoustic signal after suitable band-pass filters: the two dashed boxes indicate TAR signal and TA signal, respectively. It is seen that the TAR signal is clearly discernible from the background due to its higher SNR and narrowband characteristic. In contrast, the TA signal from a single pulse microwave is almost

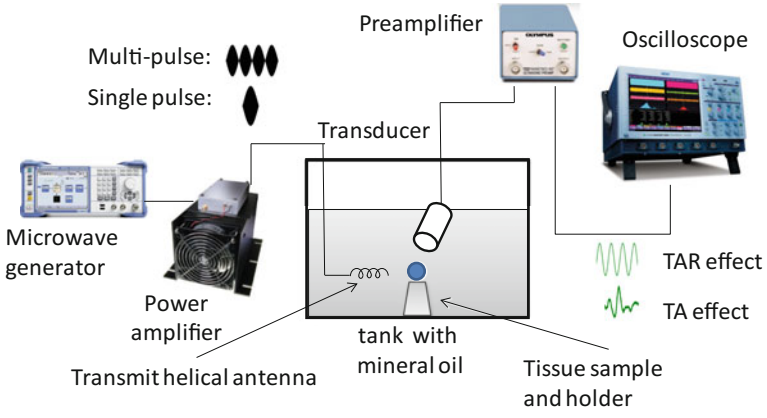

Fig. 2.28 Diagram of the experimental setup for the observation of both thermoacoustic (TA) and thermoacoustic resonance (TAR) effect induced by single pulse and multi-pulse microwave source

immersed in the noisy background. Here, even time-of-flight estimation (~30 μs delay between transmit and receive) cannot allow to detect the signal. The SNR for both TAR and TA signals are calculated within two dashed boxes (30–60 μs, 105–115 μs) in Fig. 2.29b by:

$$SNR = 10\log(\frac{P_{signal}}{P_{noise}}). \tag{2.68}$$

The SNR of the TAR signal is about 11.28 dB, and that of the TA signal is only 2.51 dB, resulting in almost 9 dB SNR improvement. Thus, a sufficient high SNR does not require a high peak power microwave source but can be obtained from the TAR effect. Increasing the number of cycles does not necessarily increase the SNR as energy dissipation in the biological tissue finally limits the TAR signal. This is equivalent to the resistance R in the series RLC circuit.

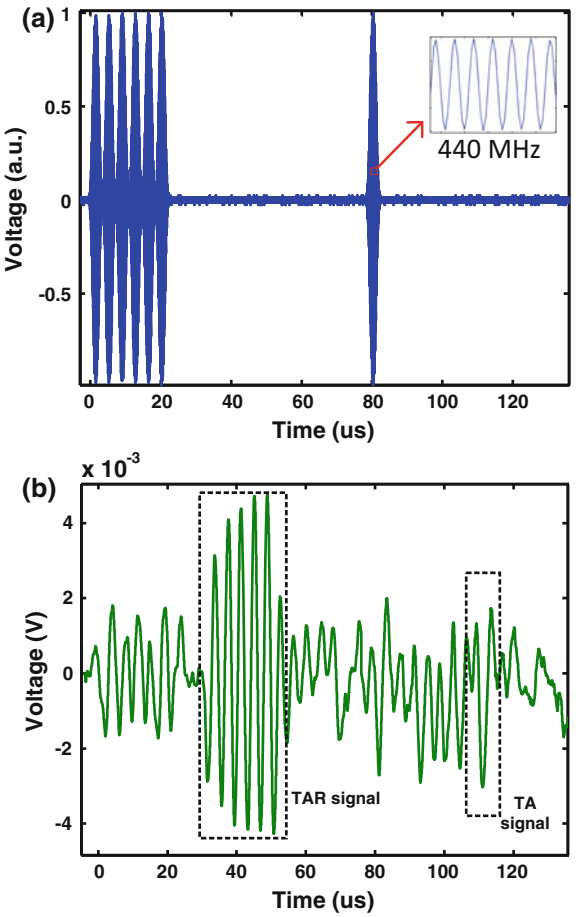

Fig. 2.29 **a** Incident multi-pulse and single pulse microwave waveform in time domain, and **b** induced acoustic signals (*dashed box*) after band-pass filtering by TAR and TA effects with regards to the incident microwave source

We obtain the constants R, L, C, ω_0 and $Q_{circuit}$ from fitting the measured response to a SPICE (Simulation Program with Integrated Circuit Emphasis) simulation model. These values are: $R = 0.5\,\Omega$, $L = 0.8\,\mu H$, $C = 0.45\,\mu F$, $\omega_0 = \sqrt{1/LC} = 1.67 \times 10^6$ rad/s, $Q_{circuit} = (1/R)\sqrt{L/C} = 2.67$. The waveform to drive the resonant system is shown in Fig. 2.30a together with the response in Fig. 2.30b. We find a good overall agreement between simulation and experiment. Interestingly, the TAR effect may allow to characterize tissue by the parameters ω_0 and $Q_{circuit}$.

The spectrum of the TAR signal, TA signal and noise are obtained by Fourier transformation within the dashed boxes, see Fig. 2.31. The central frequency of the TAR and TA signals are 0.27 and 0.21 MHz, respectively. As predicted, the TAR signal shows narrowband characteristic determined by multi-pulse illumination rather than the wideband TA signal induced by single pulse microwave illumination, allowing narrowband filtering and detection, which could sufficiently suppress the background noise because the noise amplitude is proportional to the square root of the signal bandwidth. Narrowband TAR signal also relaxes the requirements of choosing ultrasound transducer and pre-amplifier to achieve higher sensitivity even without using high peak power illumination source.

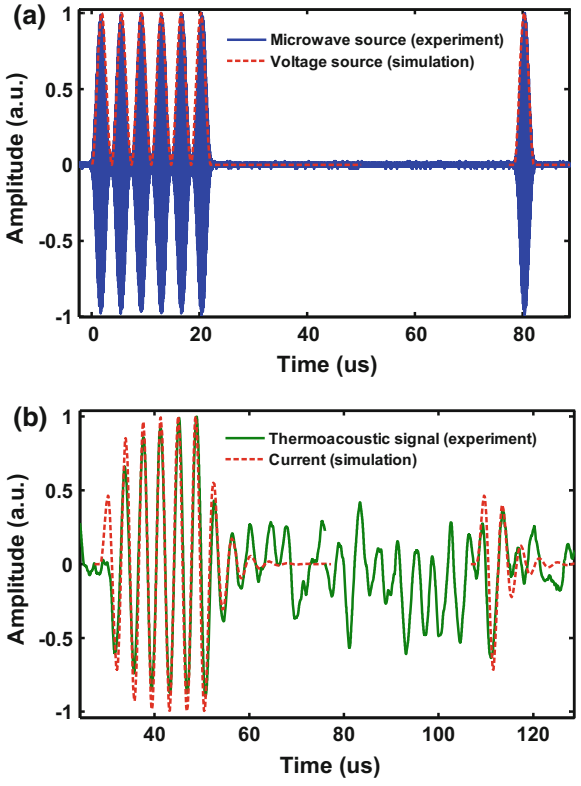

Fig. 2.30 Model fitting of **a** microwave source in experiment (*blue*) and voltage source in circuit simulation (*red*), **b** induced acoustic signal in experiment (*green*) and current in circuit simulation (*red*). Reprinted from Ref. [30] with permission from AIP Publishing LLC

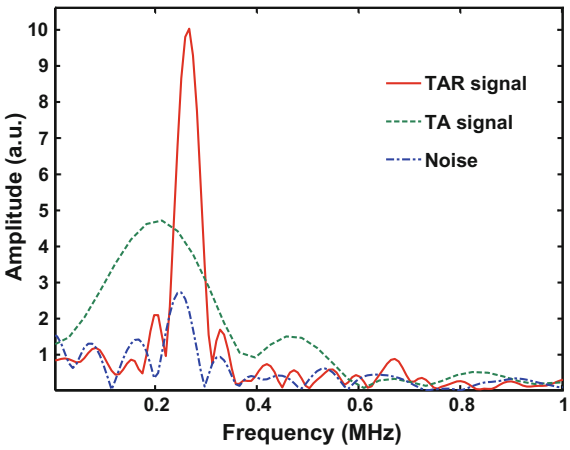

Fig. 2.31 Spectrum of TAR signal (*solid blue line*), TA signal (*dotted green line*) and noise (*solid dotted blue line*)

To further enhance the sensitivity for TAR signal detection and extract spatial information of tissue, the RLC resonance model of biological tissue is treated as a communication channel, and analyzed with scheme of coherent demodulation. Figure 2.32 depicts that the reference signal obtained after an envelope detector and differentiator, which is then cross-correlated with the detected TAR signal to obtain

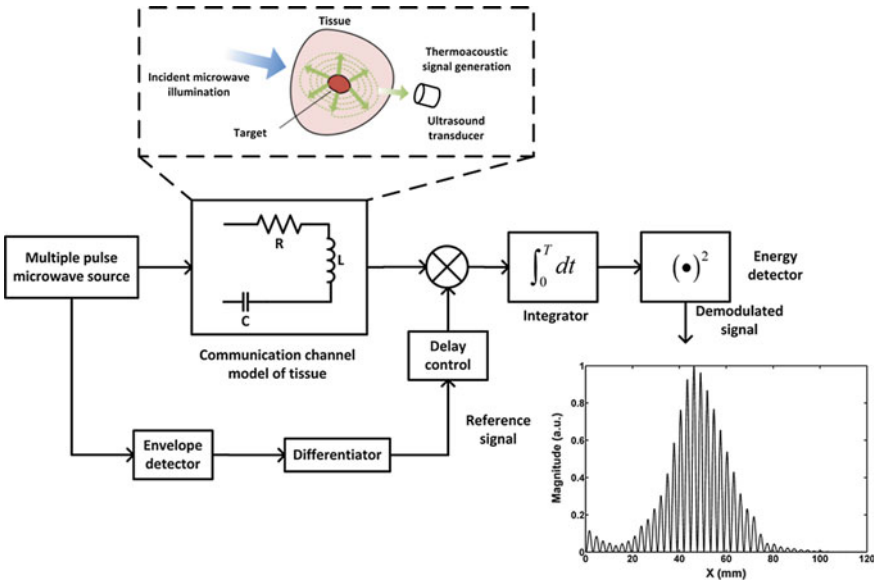

Fig. 2.32 Proposed coherent demodulation scheme by treating biological tissue as a RLC communication channel to extract the depth-resolved information. Reprinted from Ref. [30] with permission from AIP Publishing LLC

the delay time of the acoustic source. The analysis here indicates a distance of about 50 mm between biological tissue and the ultrasound transducer.

In summary, we have demonstrated thermoacoustic resonance (TAR) and evaluate its parameters through an electrical analogue (RLC circuit). The response from multi-pulse microwave illumination of muscle tissue allows to determine ω_0 and Q of circuit model. The TAR response has higher SNR and narrower bandwidth than the conventional TA signal. The model parameters allow to characterize the tissue, and imaging may be feasible with the presented cross correlation scheme. The TAR effect provides a unique prospect to develop a microwave-induced TAT prototype for low-cost portable devices operating at considerably lower peak power than current implementations.

2.3.2 *Photoacoustic Resonance Spectroscopy for Biological Tissue Characterization*

Photoacoustic effect refers to the acoustic generation thermoelastically induced by laser illumination, which is introduced in Chap. 1. In recent years, photoacoustic microscopy (PAM) and photoacoustic tomography (PAT) have been widely studied in multiple scales from contrast-enhanced molecular imaging to small animal imaging in vivo, providing high optical contrast and high acoustic resolution simultaneously due to its breaking through of optical diffusion limit. Functional photoacoustic imaging has also been proposed to detect the wavelength-dependent property of optical absorbers, which leads to important applications, such as haemoglobin concentration and oxygen saturation detection. From physical perspective, photoacoustic effect is a hybrid physical process correlating both optical absorption and mechanical vibration. Unfortunately almost all the state-of-art PAM/PAT systems are only exploring the optical absorption features and ignoring the mechanical vibration characteristics of biological tissues, which could potentially give enhanced endogenous contrast from another dimension. In this section, we demonstrate the observation of photoacoustic resonance (PAR) response of biological tissues induced by multi-burst modulated laser illumination, which is predicted by the damped mass-string oscillator model and RLC circuit. PAR spectroscopy is therefore proposed to characterize different phantom and tissue samples, revealing their mechanical resonance properties beyond optical absorption only. The primary motivation of the proposed PAR approach is to fuse the optical absorption and mechanical resonance dual-contrast for super-sensitive biomedical sensing and imaging.

The basics of photoacoustic effect have been discussed widely in previous literatures. Biological tissues illuminated by intensity-modulated laser will experience optical energy absorption, localized heating and thermal expansion, as shown in Fig. 2.33a modeling a small enough viscid biological tissue as an ideal point source, the induced acoustic pressure $p(t)$ follows the expression:

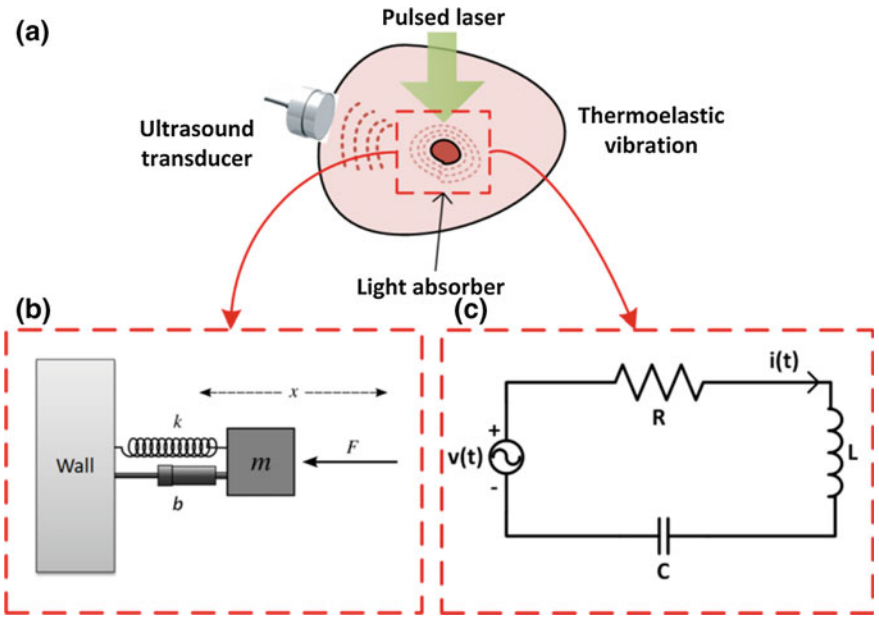

Fig. 2.33 **a** Diagram of photoacoustic effect induced by laser illumination, **b** the equivalent mass-string damped oscillator model driven by force F, and **c** equivalent RLC circuit model

$$\frac{\partial^2}{\partial t^2}p(t) + a^2\frac{\xi + \frac{4}{3}\eta}{\rho}\frac{\partial}{\partial t}p(t) + a^2c^2p(t) = \Gamma\frac{\partial H(t)}{\partial t}, \tag{2.69}$$

where a is the propagation phase constant, ρ is the tissue density, η is the shear viscosity, ξ is the bulk viscosity, and c is the acoustic velocity in tissue. Γ is the Gruneisen constant expressed as $\Gamma = \beta c^2/c_p$, where β is the thermal expansion coefficient, and c_p is the constant pressure heat capacity per unit mass. $H(t) = \mu_a\Phi(t)$ is the heating function of laser illumination, where $\nabla^2 H(\vec{r}, t) = 0$. is the optical absorption coefficient of tissue, and $\Phi(t)$ is the optical radiation fluence rate.

It is obviously seen that Eq. (2.69) is a second order differential pressure equation driven by the optical source term $\Gamma \times \partial H(t)/\partial t$. Therefore, we propose to model photoacoustic effect using the damped mass-string oscillator model, as shown in Fig. 2.33b. The differential equation of displacement $x(t)$ of this oscillator is:

$$\frac{\partial^2}{\partial t^2}x(t) + \frac{b}{m}\frac{\partial}{\partial t}x(t) + \frac{k}{m}x(t) = \frac{F(t)}{m}, \tag{2.70}$$

where m is the mass, k is the string constant, and b is the damping coefficient, which represents a force proportional to the speed of the mass. Comparing Eqs. (2.69) and (2.70), they agree well as a second order differential equation with the similar source term. Therefore photoacoustic effect of biological tissue induced by laser

illumination could be equivalently modelled as a mass-string damped oscillation driven by an external force. Assuming the driving force term is a cosine wave $F(t)/m = f_0 \cos(\omega t)$, the steady-state displacement is given by:

$$x(t) = A\ \cos(\omega t - \theta), \tag{2.71}$$

where θ is the phase shift between the displacement and the driving force, and A is the magnitude expressed as:

$$A = \frac{f_0}{\sqrt{\left(\frac{k}{m} - \omega^2\right)^2 + \left(\frac{b}{m}\omega\right)^2}}. \tag{2.72}$$

According to above analysis, the magnitude of displacement will be maximized at its resonance frequency ω_0:

$$\omega_0 = \sqrt{\frac{k}{m} - \frac{1}{2}\left(\frac{b}{m}\right)^2}. \tag{2.73}$$

Converting the damped mass-string oscillator model back into photoacoustic effect induced by laser illumination, it predicts that the magnitude of photoacoustic signal will be maximized at its resonance frequency, which we term it as "photoacoustic resonance (PAR)". By mapping Eqs. (2.69) and (2.70) for each counterpart, we have:

$$\begin{aligned} \frac{1}{m} &= \Gamma, \\ \frac{b}{m} &= a^2 \frac{\xi + \frac{4}{3}\eta}{\rho}, \\ \frac{k}{m} &= a^2 c^2, \end{aligned} \tag{2.74}$$

then the resonance frequency of biological tissue is obtained by:

$$\omega_{tissue} = \sqrt{a^2 c^2 - \frac{1}{2}\left(a^2 \frac{\xi + \frac{4}{3}\eta}{\rho}\right)^2}, \tag{2.75}$$

and the quality factor could be derived as:

$$Q = \frac{m}{b}\omega_{tissue} = \sqrt{\frac{\rho^2 c^2}{a^2\left(\xi + \frac{4}{3}\eta\right)^2} - \frac{1}{2}}. \tag{2.76}$$

Similarly, the PAR effect could also be modelled as a RLC circuit as shown in Fig. 2.33c, following the second-order differential equation:

$$\frac{\partial^2}{\partial t^2} i(t) + \frac{R}{L}\frac{\partial}{\partial t} i(t) + \frac{1}{LC} i(t) = \frac{1}{L}\frac{\partial}{\partial t} v(t). \tag{2.77}$$

Then the parameters could be mapped from the mechanical oscillator to a RLC circuit:

$$\begin{aligned} \frac{R}{L} &= \frac{b}{m}, \\ \frac{1}{LC} &= \frac{k}{m}, \\ \frac{1}{L} &= \frac{1}{m}. \end{aligned} \tag{2.78}$$

Now we have modelled the PAR effect as both the mass-string oscillator and the RLC circuit model. It is observed that tissues with different mechanical properties such as the acoustic velocity and viscosity etc. will demonstrate different resonance frequencies and quality factors. Therefore, by sweeping the frequency of a multi-burst modulated laser, the photoacoustic response of different tissues could be maximized when the frequency hits their unique resonance frequencies, which is proposed as the "PAR spectroscopy". Moreover, different tissues could also be differentiated quantitatively by the circuit model parameters, such as equivalent impedance and phase (consisting of resistance, inductance, capacitance), extracted from the resonance frequency and quality factor.

The experimental setup for PAR effect and PAR spectroscopy is shown in Fig. 2.34, a continuous-wave (CW) laser (RD532-100G4, Laser-rich Ltd.) with 1 W average power and 532 nm wavelength is used to provide the light source, which is focused by a condenser lens (LB1471, Thorlabs) and fed into an acousto-optic modulator (R23080-1-.85-LTD, Gooch & Housego) for intensity-modulation controlled by a function generator (33250A, Agilent). The function generator could provide multi-burst waveform with its frequency swept for spectrum analysis. A beam splitter and a photodiode (DET10A, Thorlabs) are used to monitor the input laser power for calibration purpose. The laser beam is weakly focused onto the biological tissue placed in de-ionized water with a spot of ~ 2 mm in diameter. Photoacoustic signal is collected by a wideband ultrasound transducer with 2.25 MHz central frequency (V323-SU, Olympus), followed by an ultrasound preamplifier (Model 5662, Olympus). A digital oscilloscope (HDO4000, 12-bit, Lecroy) is used to record the photoacoustic signal at 500 MHz sampling rate.

To prove the PAR effect and the feasibility of the proposed PAR spectroscopy, three agar phantoms with different agar concentration (1, 2, 3%) are prepared to simulate tissues with different mechanical properties, such as viscosity and acoustic impedance, which are made into slices with 3 mm thickness. By sweeping the multi-burst modulation frequency of the laser source from 50 to 150 kHz with step

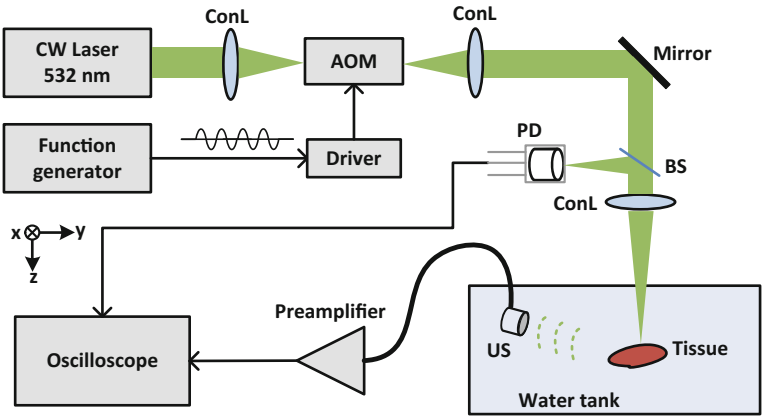

Fig. 2.34 Diagram of the experimental setup for the observation of photoacoustic resonance effect and spectroscopy. *ConL* condenser lens; *AOM* acousto-optic modulator; *BS* beam splitter; *PD* photodiode; *US* ultrasound transducer

2 kHz, the peak-to-peak magnitude is recorded at every frequency point. Utilizing an ultrasound transducer with flat frequency response in the interested band, the spectrums of the three phantoms are shown in Fig. 2.35a, where at the resonance frequency of each phantom, the magnitude is larger than those at other frequencies, proving the PAR effect. In addition, phantoms with higher agar concentration (higher viscosity) exhibit lower resonance frequency, which is matched with the prediction from Eq. (2.75). The waveforms of the PA signals from the phantom 3 at resonance (75 kHz) and non-resonance (130 kHz) are shown in Fig. 2.35b, where the PA signal at resonance has increasingly larger amplitude (>0.8 mV) and significantly narrower bandwidth of <20 kHz (high Q) than the PA signal at non-resonance with amplitude <0.4 mV and bandwidth >200 kHz (low Q), as expected. To further verify the feasibility of PAR spectroscopy for tissue characterization, three kinds of porcine tissues (muscle, fat, liver) are prepared in slices to be tested by the PAR spectroscopy by sweeping the multi-burst modulation frequency from 50 to 300 kHz. Figure 2.35c shows that the liver has the lowest resonance frequency due to its highest viscosity while the muscle has the highest resonance frequency with the smallest viscosity, which is matched well with the reported data [31]. The experiment results demonstrate that the proposed PAR spectroscopy is able to characterize different biological tissues by their mechanical resonance property, showing the potential to achieve a new kind of spectroscopic imaging. The error bar in the Fig. 2.35 may be caused by the geometry, heat dissipation and ultrasound detection uncertainty of the sample, which will be optimized in the next iteration of design.

Next we will extract the RLC circuit parameters and impedance from the resonance frequency and quality factor shown in the spectrums in Fig. 2.35a, c. Based on Eqs. (2.74) and (2.78), $L = 1/\Gamma$, where the Gruneisen factor Γ is normally supposed to be constant for all the samples, so here the inductance is chosen to be

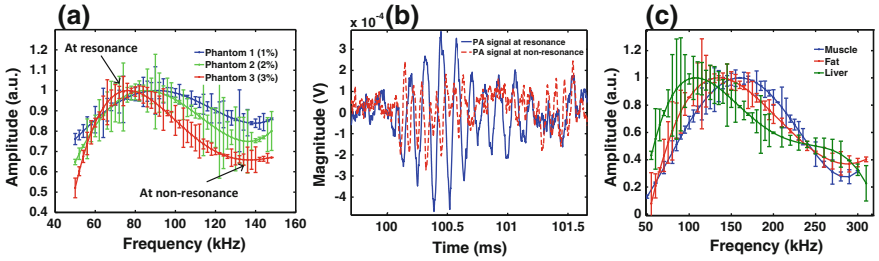

Fig. 2.35 **a** The PAR spectroscopy for three phantoms with different agar densities to simulate the different mechanical properties, and **b** waveforms of photoacoustic signal at resonance and non-resonance. **c** PAR spectroscopy for three different biological tissues characterized by their resonance frequencies and Q factors

1 H for normalization. Then according to the resonance frequency ω_0 and quality factor Q exacted from the PAR spectrums, the R, L and C can be calculated from the extracted ω_0 and Q with the following equations by substituting Eq. (2.78) into Eqs. (2.74)–(2.77):

$$\begin{aligned} R &= \omega_0 L\sqrt{2Q^2-1}, \\ C &= \frac{2Q^2}{\omega_0^2 L(2Q^2+1)}, \\ L &= 1, \end{aligned} \tag{2.79}$$

Based on Eq. (2.79), the circuit complex impedance $Z = R + j\omega_0 L + 1/j\omega_0 C$ can be calculated. Now the different phantoms and porcine tissues have been quantitatively characterized by the equivalent RLC circuit parameters. It is worth noting that for different phantoms and tissue samples, the absolute values of real part and imaginary part of the circuit impedance are changing on the opposite way, i.e., when the real part is decreasing, the imaginary part is increasing, and vice versa. Therefore similar to the proposed concept of phasoscopy in previous section, we can employ the phase $\tan\varphi = \mathrm{Im}(Z)/\mathrm{Re}(Z)$ of the circuit impedance as a correlated indicator for PAR spectroscopy characterization. As described above, the R, L, C, ω_0, Q, Z, and $\tan\varphi$ of the phantoms and tissues are listed in Table 2.7. Furthermore, the extracted phase can be derived from Eqs. (2.74) to (2.78) as:

$$\begin{aligned} \tan\varphi &= \left[\sqrt{a^2c^2 - \frac{1}{2}\left(a^2\frac{\xi+\frac{4}{3}\eta}{\rho}\right)^2}\right]\left[\frac{\rho\left(\xi+\frac{4}{3}\eta\right)}{a^2\left(\xi+\frac{4}{3}\eta\right)^2 - 2\rho^2c^2}\right] \\ &= \left(\frac{-\frac{1}{2}\Lambda}{\sqrt{1-\frac{1}{2}\Lambda^2}}\right), \quad \text{where } \Lambda = a\frac{\xi+\frac{4}{3}\eta}{\rho c}. \end{aligned} \tag{2.80}$$

Table 2.7 RLC circuit parameters of three phantoms and porcine tissues

Sample	ω_0 (kHz)	Q	R (kΩ)	C (pF)	L (H)	Z (Ω)	$\tan\varphi\|_{\omega=\omega_0}$
Phantom 1	90	0.5	71.59	93.787	1	7.159×10^4 + jω(0.1188)	0.1825
Phantom 2	85	1.1	67.61	105.14	1	6.761×10^4 + jω(0.2140)	0.3482
Phantom 3	73	1.5	58.07	142.55	1	5.807×10^4 + jω(0.4203)	0.7961
Muscle	160	1.4	127.27	29.675	1	1.2727×10^5 + jω (0.1575)	0.2476
Fat	130	1.2	103.41	44.951	1	1.0341×10^5 + jω (0.4438)	0.8584
Liver	110	1.0	87.50	62.783	1	8.750×10^4 + jω(0.6018)	1.3756

If we choose negative a with $|a| \ll 1$, then Eq. (2.80) can be approximated as:

$$\tan\varphi \approx -\frac{1}{2}\left(\Lambda + \frac{1}{4}\Lambda^3\right) \approx -\frac{1}{2}\Lambda. \tag{2.81}$$

Equation (2.81) discloses that the proposed spectroscopy indicator $\tan\varphi$ is the ratio between viscosity parameter $(\xi + 4/3\eta)$ and acoustic impedance (ρc), correlating the physical basis of viscosity imaging and ultrasound imaging to achieve an improved contrast.

The advantage of the proposed PAR spectroscopy is threefold: Firstly from physical perspective: compared with conventional photoacoustic approaches exploring the optical absorption property of biological tissues only, the proposed PAR spectroscopy based on the PAR effect is revealing both optical absorption and mechanical resonance properties, which is intrinsically an endogenous dual-contrast characterization approach. In addition, separation of the two kinds of contrasts is also feasible: Photoacoustic mechanical resonance spectrum in terms of resonance frequency (ω_0) and quality factor (Q) is related with mechanical property only (viscosity, mechanical impedance), and doesn't depend on optical absorption property; Optical absorption contrast could also be readily obtained by utilizing single-pulse modulation of the CW laser source, which is similar with pulsed laser illumination without resonating the biological tissue. Secondly from performance perspective: utilizing the PAR effect, the PA signal of the object could be maximized at its resonance frequency, giving the enhanced SNR. In addition, the narrowband characteristic of the PA signal at resonance allows subsequent narrowband amplification and detection using lock-in amplifier with much higher sensitivity than conventional wideband PA signals induced by single pulse lasers. Thirdly from application perspective: potential applications of the PAR spectroscopy will extend the conventional PAM/PAT applications. The proposed PAR spectroscopy is also capable of revealing mechanical resonance properties related with viscosity

and acoustic impedance, which are also important indicators of biological tissue and other materials. In brief, the PAR effect and spectroscopy proposed in this section are marriage of optical absorption and mechanical resonance effects, going beyond conventional pulsed-laser photoacoustic approaches by providing endogenous dual-contrast performance.

In summary, the PAR effect is predicted and modelled by the damped mass-string oscillator model and the RLC electrical circuit model, and investigated experimentally by sweeping the multi-burst modulation frequency of a laser source. Both agar phantoms and biological tissues are tested to show different spectrums, demonstrating the significant potential of the PAR spectroscopy for tissue characterization. Electrical circuit parameters are also extracted for unique quantitative analysis. A potential PAR imaging technique will be implemented in the future for in vivo animal study.

2.4 EM-Acoustic Elastic Oscillation and Characterization

In this section, the EM-acoustic, specifically photoacoustic, elastic damped oscillation effect will be introduced and utilized for biological tissue characterization. Being different from the photoacoustic resonance effect in previous section, the damped oscillation of the elastic object is induced by pulsed laser illumination. the photoacoustic damped oscillation is predicted and modelled by an equivalent mass-string system by treating the optical absorber as an elastic oscillator. The photoacoustic simulation incorporating the proposed oscillation model shows better agreement with the measured signal from an elastic phantom, than conventional photoacoustic simulation model. More interestingly, the photoacoustic damping oscillation effect could potentially be a useful characterization approach to evaluate biological tissue's mechanical properties in terms of relaxation time, peak number and ratio, beyond optical absorption only. The results of this section have been submitted to *Optics Express*.

2.4.1 Introduction

Photoacoustic (PA) effect refers to the ultrasound generation induced by the pulsed laser illumination due to thermoelastic expansion, which is introduced in Chap. 1. Based on the "listening to photons" advantage of PA effect to break through the optical diffusion limit, both PA microscopy and computed tomography have attracted dramatically increasing research interest in recent years to achieve high optical contrast and high ultrasound resolution at unprecedented imaging depth. Theoretically, to better understand and model the PA generation mechanism,

previous literatures have derived both analytical and numerical expressions to simulate the PA generation and propagation. The simulated PA waveform from existing analytical model or numerical simulator (i.e. k-space pseudospectral method [32, 33]) is commonly a bipolar "N-shape" pulse with no oscillation effect. However in real situation, the PA oscillation effect could be considered as the damped harmonic oscillation of an elastic optical absorber, which has not been properly modelled. In this section, firstly we derive the PA generation equation and model it as a damped mass-string system. Then the PA damped oscillation effect is predicted and simulated as an impulse response of the damped mass-string oscillator. The simulated PA signal shows much better agreement with the measured PA signal compared with existing k-space pseudospectral method. Moreover, the PA damped oscillation could potentially be a very useful tool to characterize the mechanical properties, e.g. viscoelasticity and acoustic impedance, of the object in terms of the oscillation relaxation time, peak number and ratio. A feasibility study using two types of phantoms (a black line made of plasticized polyvinyl chloride, and a silicone tube filled with porcine blood) is demonstrated to show different PA oscillation effect. Ex vivo porcine muscle tissues (pink muscle and red muscle) are also evaluated and differentiated by their oscillation peak ratios. Lastly, a simulation study of image reconstruction embedding the PA damped oscillation effect is provided to demonstrate more details for tumor characterization than traditional PA imaging.

2.4.2 Theory

The formulation of PA effect has been well established in previous literatures. By modeling the optical absorbing object as a small viscid point source shown in Fig. 2.36a, the generated PA wave will follow the below equation:

$$\frac{\partial^2}{\partial t^2}p(t) + a^2\frac{\xi + \frac{4}{3}\eta}{\rho}\frac{\partial}{\partial t}p(t) + a^2c^2p(t) = \Gamma\frac{\partial H(t)}{\partial t}, \tag{2.82}$$

where a is the propagation phase constant, ρ is the tissue density, η is the shear viscosity, ξ is the bulk viscosity, and c is the acoustic velocity in tissue. Γ is the Gruneisen constant expressed as $\Gamma = \beta c^2/c_p$, where β is the thermal expansion coefficient, and c_p is the constant pressure heat capacity per unit mass. $H(t) = \mu_a\Phi(t)$ is the heating function of laser illumination, where μ_a is the optical absorption coefficient of tissue, and $\Phi(t)$ is the optical radiation fluence rate.

It is obvious that Eq. (2.82) is a second order differential pressure equation driven by the optical source term $\Gamma \times \partial H(t)/\partial t$. Therefore, in order to give an intuitive perspective of the PA oscillation, we employ the well-known damped mass-string system for illustration, as shown in Fig. 2.36b. The differential equation of displacement $x(t)$ of this oscillator is:

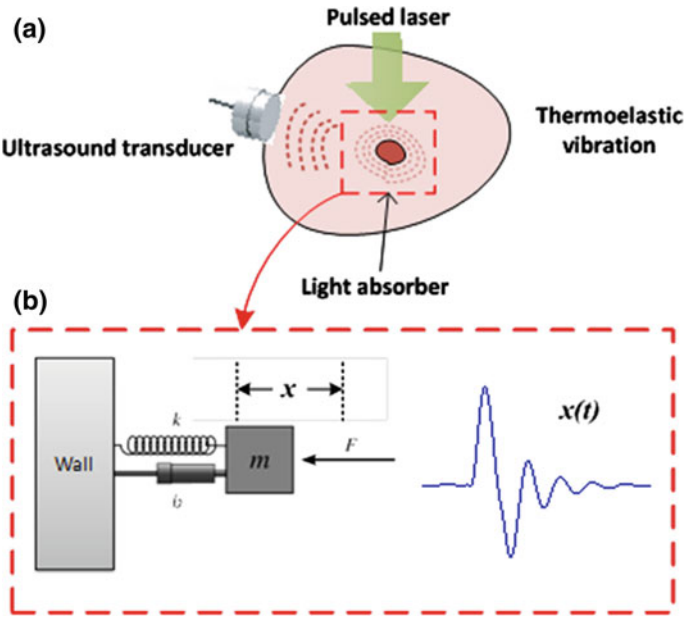

Fig. 2.36 **a** The diagram of PA effect induced by pulsed laser. **b** The mass-string damped oscillation model of PA effect and a typical simulated PA signal incorporating this model

$$\frac{\partial^2}{\partial t^2}x(t) + \frac{b}{m}\frac{\partial}{\partial t}x(t) + \frac{k}{m}x(t) = \frac{F(t)}{m}, \tag{2.83}$$

where m is the mass, k is the string constant, and b is the damping coefficient, which represents a force proportional to the speed of the mass. Comparing Eqs. (2.82) and (2.83), it is observed that they agree well as a second order differential equation with the similar source term. Therefore, we could naturally map the parameters in Eqs. (2.82) and (2.83) to obtain:

$$\begin{aligned} \frac{1}{m} &= \Gamma, \\ \frac{b}{m} &= a^2\frac{\xi + \frac{4}{3}\eta}{\rho}, \\ \frac{k}{m} &= a^2c^2. \end{aligned} \tag{2.84}$$

To derive the analytical solution of Eq. (2.83), the PA response of the elastic object is treated as an impulse response externally triggered by an ultra-short pulsed laser. In this case the source term $F(t)$ could be simplified to be zero when the laser pulse-width ($\sim$ns) is much shorter than the thermoelastic relaxation time ($\sim\mu$s). By substituting $\omega_0^2 = k/m, \zeta = b/2m$ into Eq. (2.83), we can have:

$$\frac{\partial^2}{\partial t^2}x(t) + 2\zeta\frac{\partial}{\partial t}x(t) + \omega_0^2 x(t) = 0, \tag{2.85}$$

then it could be solved by:

$$\begin{aligned} x(t) &= Ae^{S_1 t} + Be^{S_2 t}, \\ s_1 &= -\zeta + \sqrt{\zeta^2 - \omega_0^2}, \\ s_2 &= -\zeta + \sqrt{\zeta^2 - \omega_0^2}, \end{aligned} \tag{2.86}$$

where A, B could be determined by the initial conditions. The solution in Eq. (2.86) could be further categorized into three cases:

1. $\zeta < \omega_0$: under damped case:

$$x(t) = A_d e^{-\zeta t}\cos(\omega_d t + \phi_d), \quad \text{where } \omega_d = \sqrt{\omega_0^2 - \zeta^2}. \tag{2.87}$$

The constant A_d, ϕ_d are to be determined by the initial conditions. The motion $x(t)$ is an exponentially damped sinusoidal oscillation.

2. $\zeta > \omega_0$: over damped case:

$$\begin{aligned} x(t) &= A_1 e^{-\lambda_1 t} + A_2 e^{-\lambda_2 t}, \\ \lambda_1 &= \zeta + \sqrt{\zeta^2 - \omega_0^2}, \\ \lambda_2 &= \zeta + \sqrt{\zeta^2 - \omega_0^2}. \end{aligned} \tag{2.88}$$

The constant A_1, A_2 are to be determined by the initial conditions. There is no oscillation at all and the motion $x(t)$ dies off exponentially.

3. $\zeta = \omega_0$: critically damped case:

$$x(t) = A_c e^{-\zeta t}. \tag{2.89}$$

The constant A_c is to be determined by the initial conditions. This is the case where motion $x(t)$ dies off in the quickest way with no oscillation.

Among the above three cases, because PA effect includes both expansion and contraction caused by transient laser-induced heating and sequent cooling, the generated PA signal is normally following the under damped oscillation including

both positive and negative peaks, as shown in Fig. 2.36b. By substituting the parameters in Eq. (2.84) into Eq. (2.87), we can have:

$$p(t) = A_d e^{-\frac{1}{2}a^2\frac{\xi+\frac{4}{3}\eta}{\rho}t}\cos\left(\sqrt{a^2c^2-\left(\frac{1}{2}a^2\frac{\xi+\frac{4}{3}\eta}{\rho}\right)^2}t-\frac{\pi}{2}\right), \quad \text{when } p(0)=0. \tag{2.90}$$

To visualize the properties of PA damped oscillation for object characterization, here three parameters are defined: relaxation time T_r, peak number P_n and peak ratio P_r. Relaxation time is defined as the time duration when the envelope amplitude of the PA signal is decreased to 10% of the first maximum peak:

$$e^{-\frac{1}{2}a^2\frac{\xi+\frac{4}{3}\eta}{\rho}T_r} = 0.1. \tag{2.91}$$

Then the relaxation time could be obtained by:

$$T_r = \frac{\rho}{a^2}\frac{4.6}{\xi+\frac{4}{3}\eta}. \tag{2.92}$$

It is observed that the relaxation time T_r is proportional to the density ρ, and inversely proportional to the viscosity $\xi+4/3\eta$. The peak number P_n could be derived by the ratio between relaxation time T_r and the sinusoidal period $T = 2\pi/\omega_d$:

$$P_n = \frac{T_r}{T} = \frac{2.3}{2\pi}\sqrt{\frac{4}{a^2}\left(\frac{\rho c}{\xi+\frac{4}{3}\eta}\right)^2-1}. \tag{2.93}$$

It is observed that the peak number P_n is proportional to the ratio between acoustic impedance ρc and viscosity $\xi+4/3\eta$, which could be a novel characterization approach correlating optical absorption, mechanical property (bulk and shear viscosity) and acoustic property (acoustic impedance) of the same object. Lastly, for some extreme cases, where relaxation time and peak number are almost same, the peak ratio P_r between the first peak and second peak of PA signal could be derived for more accurate evaluation:

$$P_r = \frac{P\left(t=\frac{\pi}{2\omega_d}\right)}{P\left(t=\frac{5\pi}{2\omega_d}\right)} = \exp\left(\frac{2\pi}{\sqrt{\frac{4}{a^2}\left(\frac{\rho c}{\xi+\frac{4}{3}\eta}\right)^2-1}}\right). \tag{2.94}$$

Different from the peak number expression in Eq. (2.93), the peak ratio P_r of Eq. (2.94) is inversely proportional to the ratio between acoustic impedance and viscosity. Intuitively, a higher viscosity will cause larger peak ratio, indicating more

energy loss per oscillation cycle. The exponential function will also enhance the sensitivity of peak ratio characterization.

2.4.3 Simulation and Experimental Results

In the above, the PA damped elastic oscillation has been well modelled by a mass-string system. To incorporate the PA damped oscillation effect into a PA simulation tool, the k-space pseudospectral method based MATLAB toolbox is employed and modified. The initial pressure is replaced by a time-varying pressure source from Eq. (2.90) by assigning proper physical parameters. Experiment on phantom is also conducted based on the PA measurement setup, as shown in Fig. 2.37. A nanosecond pulsed laser (FDSS 532-1000, CryLaS, GmbH) is used to provide green light illumination with 532 nm wavelength and 1 mJ pulse energy. The light is focused into a multimode fibre (MHP550L02, Thorlabs) by a fibre coupler, and focused on the phantom by a pair of lens (LB1471, Thorlabs). The black line phantom made of plasticized polyvinyl chloride (PVC) is immersed in water for optimum light transparency and acoustic coupling. A focused ultrasound transducer (V303-SU, Olympus) with 1 MHz central frequency is used to detect the PA signal, followed by a 54 dB gain preamplifier (5662, Olympus). A digital oscilloscope (WaveRunner 640Zi, LeCroy) with 500 MHz sampling rate is used to record the PA signal and send it to a PC for post-processing.

The PA simulation results of k-space pseudospectral method without and with incorporating the PA oscillation model are shown in Fig. 2.38a, b, as well as the measured PA signal shown in Fig. 2.38c. It is clearly observed that by

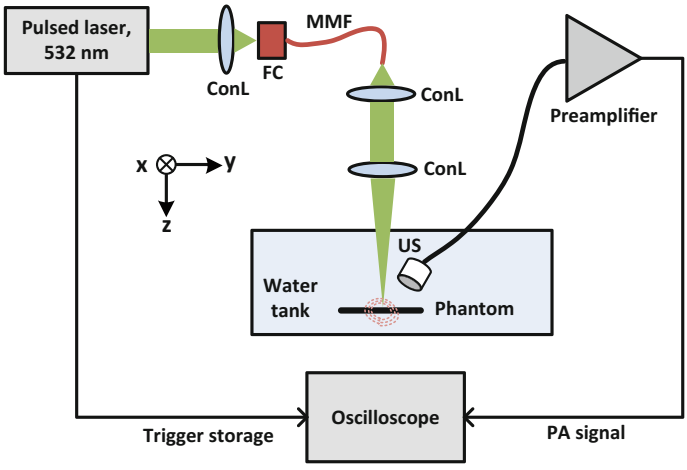

Fig. 2.37 The experimental setup of photoacoustic measurement. *ConL* condenser lens; *FC* fibre coupler; *MMF* multi-mode fibre; *US* ultrasound transducer

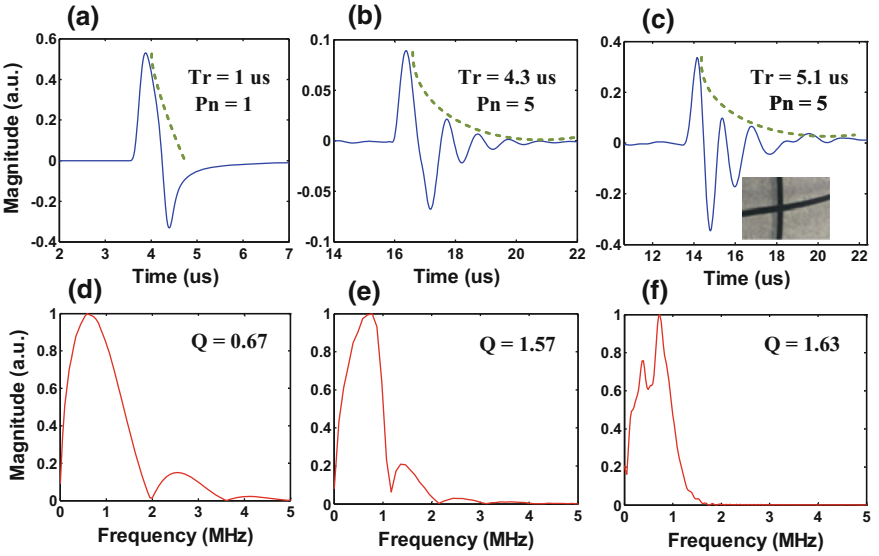

Fig. 2.38 **a**, **b** K-space pseudospectral method simulation results without and with incorporating the proposed PA oscillation model. **c** Measured PA signal of the *black line* phantom with photograph. **d**–**f** The frequency spectrums of the PA signals in (**a**)–(**c**)

incorporating the PA oscillation model in the k-space simulation tool, the simulated PA damped oscillation waveform in Fig. 2.38b is much more close to the measured waveform in Fig. 2.38c in shape, compared with the conventional k-space simulated "N-shape" waveform in Fig. 2.38a. Quantitatively, the relaxation times T_r of the PA waveforms in Fig. 2.38a–c are calculated to be 1, 4.3, and 5.1 μs. The peak numbers P_n are 1, 5, and 5, showing that the PA simulation with the proposed oscillation model presents much better agreement than the conventional simulation approach. Figure 2.38d–f are plotted to show their respective spectrums, and the quality factors match well between Fig. 2.38e, f, validating the proposed PA damped oscillation model.

To further verify the characterization capability of PA damped oscillation in terms of relaxation time and peak number, a vessel-mimicking phantom is prepared using a silicone tube filled with porcine blood. The measured PA signal is shown in Fig. 2.39a, where the relaxation time is 1.2 μs and the peak number is 3. Compared with the PVC line phantom in last experiment, the vessel-mimicking phantom suffers higher viscosity and lower acoustic velocity, leading to smaller relaxation time and peak number, predicted from Eqs. (2.92) and (2.93). To demonstrate the feasibility of characterizing biological tissues, ex vivo porcine tissues are prepared including pink muscle and red muscle. Figure 2.39b, c are showing the typical PA oscillation signals from pink muscle and red muscle parts, where the peak number is same for both and invalid for characterization. Therefore we calculate the peak ratio P_r of the two kinds of muscles to be 3.5 and 9.2. Then we conduct 20

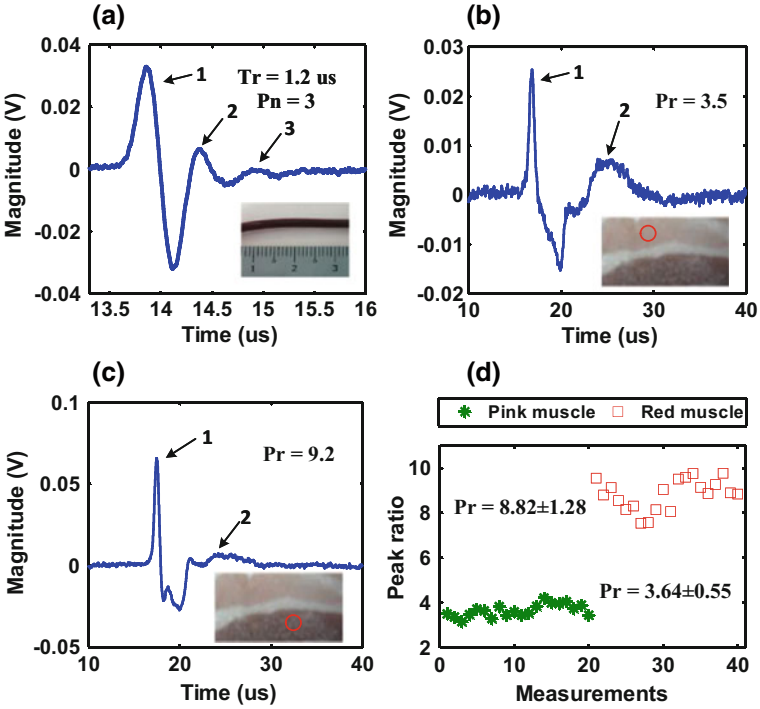

Fig. 2.39 **a** The typical PA oscillation signal and characterization of a vessel-mimicking phantom, **b** *pink muscle*, and **c** *red muscle*. **d** The peak ratio of 20 measurements each for pink and red muscle. Reprinted from Ref. [34] with permission from OSA Publishing

measurements for both pink and red muscles within the red circle region in the tissue photograph, which are plotted in Fig. 2.39d. It is observed that red muscle has statistically much higher peak ratio $P_r = 8.82 \pm 1.28$ than pink muscle $P_r = 3.64 \pm 0.55$, indicating the higher acoustic energy loss rate in red muscle. The underlying reason is: the red muscle contains more mitochondria, myoglobin, and capillaries than the pink muscle. Therefore the red muscle is expected to suffer higher viscosity to attenuate the acoustic energy more significantly.

In the last section, PA imaging simulation is performed by incorporating the PA oscillation model. The simulation diagram is shown in Fig. 2.40a, where two tumors are embedded with different oscillation damping factors due to different viscosity properties to mimic malignant and benign tumors, and surrounded by 100 acoustic sensors. The PA signals of the two tumors detected by one of the sensors are shown in Fig. 2.40b as well as all the sensor data shown in Fig. 2.40c. It is seen that tumor 1 features larger relaxation time and peak numbers than tumor 2. After image reconstruction by simplified back-projection algorithm, it shows that the tumor 1 demonstrates more "ripples" than tumor 2 in Fig. 2.40d, which indicates that tumor 1 suffers less acoustic attenuation and viscosity. Based on the fact that

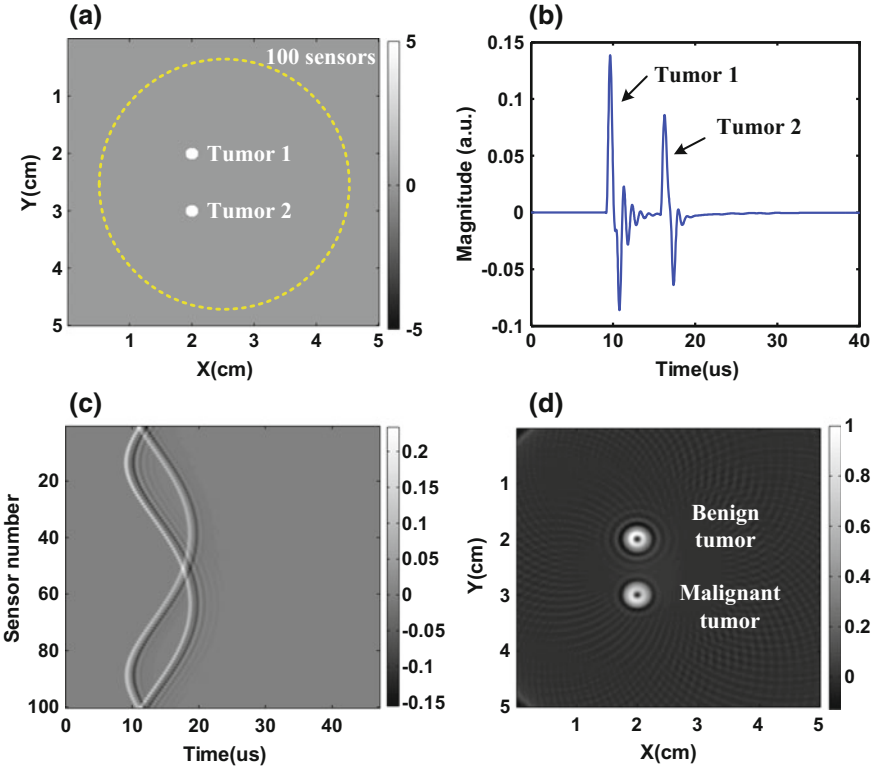

Fig. 2.40 **a** The PA imaging simulation diagram of two tumors incorporating the PA oscillation model. **b** A typical PA signal from one of the acoustic sensors, and **c** all the PA signals from 100 acoustic sensors. **d** The reconstructed PA image of the two tumors. Reprinted from Ref. [34] with permission from OSA Publishing

malignant tumor has more irregular shape, greater impedance discontinuities and disorganized vasculature [35], leading to higher viscosity and acoustic attenuation than benign tumor, inducing less 'ripple' in the reconstructed images, we can conclude that tumor 1 is a benign tumor, and tumor 2 is a malignant one. The quantitative characterization in terms of relaxation time, peak number and peak ratio is summarised in Table 2.8, providing more accurate and reliable classification of benign/malignant tumor than direct observation from the images. In this case, conventional PA imaging analysis could not tell which one is more malignant as

Table 2.8 Quantitative characterization of benign/malignant tumors

	Tumor 1 (benign)	Tumor 2 (malignant)
Relaxation time (T_r) (μs)	5.6	3.5
Peak number (P_n)	5	2
Peak ratio (P_r)	6.2	30.7

they show similar image intensity. Interestingly, by considering the PA oscillation effect, i.e. multiple cycles in PA signal could lead to multiple ripples in PA image, the more malignant tumor with less ripples could be easily identified due to its higher viscosity and acoustic attenuation. The proposed quantitative characterization of PA elastic oscillation is proved to be potential for benign/malignant tumor classification with higher sensitivity and reliability.

2.4.4 Summary

In conclusion, we have modelled the PA elastic oscillation as a damped mass-string system theoretically, and achieved prediction and simulation much closer to the experimentally observed PA signal, compared with conventional PA simulation. Utilizing the PA oscillation effect, three parameters are proposed to characterize the phantoms and biological tissues, which revealed the mechanical properties (viscosity, acoustic impedance) experimentally in terms of relaxation time, peak number, and peak ratio. Lastly the feasibility of PA elastic oscillation in imaging reconstruction is explored, where malignant and benign tumors are well differentiated. By incorporating the PA elastic oscillation characterization in conventional PA imaging, we open the window to enable the PA imaging to characterize both optical and mechanical properties in single imaging modality.

2.5 Coherent EM-Acoustic Ultrasound Correlation and Imaging

Both photoacoustics and ultrasound have been studied extensively but separately. In this section, we report an initial study on the coherent correlation between pulsed photoacoustic wave and pulse-echo ultrasound wave. By illuminating an object with pulsed-laser and external ultrasound sequentially, both the endogenous photoacoustic wave and pulse-echo ultrasound wave are received and coherently correlated, demonstrating enhanced signal-to-noise ratio. Image contrast of the proposed coherent photoacoustic-ultrasound imaging is also demonstrated to be improved significantly on vessel-mimicking phantom, due to fusion of the optical absorption and ultrasound reflection contrasts by coherent correlation than either conventional laser-induced photoacoustic imaging or pulse-echo ultrasound imaging separately. The results of this section have been published in *IEEE Transactions on Biomedical Engineering* [36].

2.5.1 Introduction

Photoacoustic and thermoacoustic effects refer to the acoustic generation thermoelastically induced by pulsed electromagnetic wave, e.g. laser, microwave, or very recently proposed magnetic mediation, which is introduced in Chap. 1. In the recent decade, photoacoustic technique shows significant potentials for biomedical sensing and imaging, ranging from contrast-enhanced molecular imaging to whole body tomography of small animals. Although photoacoustic imaging could break through the optical diffusion limit by converting photons to ultrasound and sustaining high spatial resolution in deep tissue, the sensitive detection of the weak photoacoustic signal is a long-standing challenge especially for deep tissue imaging [37] due to strong optical scattering/absorption, very low energy conversion efficiency from optical to acoustic energy and strict ANSI safety standard limit (<20 mJ/cm^2). In a typical photoacoustic imaging system, a pulsed laser will illuminate the sample to induce the transient acoustic emission, which will be detected by ultrasound transducers for image reconstruction. Due to sharing the same ultrasound components with conventional pulse-echo ultrasound imaging, recent studies have demonstrated the feasibility of photoacoustic-ultrasound dual-modality imaging approaches [8, 20–22, 38, 39]. However, these dual-modality approaches all separately explore the pulsed photoacoustic wave and pulse-echo ultrasound wave for complementary imaging reconstructions. Up to now, the coherent correlation between endogenous photoacoustic wave and exogenous ultrasound wave has been an untapped area to be explored.

In this section, we report the initial research on the study of intrinsic physical correlation between endogenous photoacoustic wave and exogenous ultrasound wave coming from the same object by fusing the optical absorption and ultrasound reflection contrasts based on the coherent detection approach, see Fig. 2.41. The proposed coherent photoacoustic-ultrasound (PAUS) correlation is implemented by cross-correlating (multiplication and integration) the two signals to enhance the weak PA signal and suppress the uncorrelated strong noise significantly, leading to significantly enhanced signal-to-noise ratio (SNR). The proposed coherent PAUS imaging is also demonstrated through a vessel-mimicking phantom experiment with improved contrast significantly than either conventional pulsed photoacoustic imaging or pulse-echo ultrasound imaging separately.

2.5.2 Theory

In communication, radar and sonar systems, coherent detection (also called matched filtering) is usually applied to recover the weak received signal $r(t)$ immersed in the white Gaussian noise introduced by the communication channel [40]. Specifically, a template signal $s(t)$ that is a replica of the transmitted signal highly correlated with

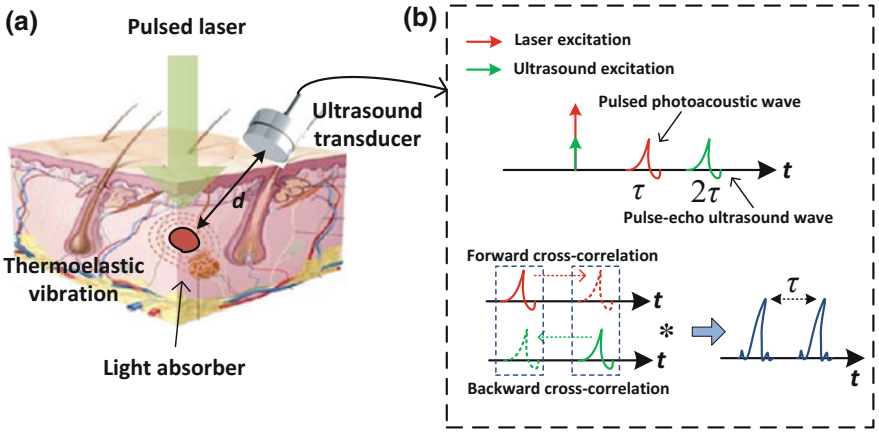

Fig. 2.41 **a** Diagrams of the coherent PAUS correlation, where the object is excited by both a pulsed laser and external ultrasound. **b** Schematic of the incoherent detection (*top*), and coherent PAUS correlation including time-shift, multiplication and integration (*bottom*), where * represents the convolution

the received signal is used to cross-correlate with the received signal $r(t)$ to achieve maximum SNR:

$$\langle s, r\rangle(t) = \int_{+\infty}^{+\infty} s^*(t) \times r(t+\tau)d\tau, \tag{2.95}$$

where $s^*(t)$ is the complex conjugate of $s(t)$. In a photoacoustic procedure, the laser-induced photoacoustic wave $p(r, t)$ could be treated as the weak received signal suffering the strong noise induced in the acoustic channel. To optimally detect the weak $p(r, t)$, a replica of the true photoacoustic signal is required, which is however physically not available. Here we propose a method to obtain a highly correlated template signal by transmitting and receiving the pulse-echo ultrasound signal $u(r, t)$ with controlled similar pattern to the photoacoustic signal coming from the same object and experiencing the same acoustic channel response.

Firstly the pattern (time domain waveform and frequency domain spectrum) of the photoacoustic signal should be estimated. As shown in Fig. 2.41a, using ultra-short laser illumination, the induced photoacoustic wave $p(r, t)$ in a non-viscous medium could be described as:

$$\nabla^2 p(r,t) - \frac{1}{v_s^2}\frac{\partial^2}{\partial t^2}p(r,t) = -\frac{\beta}{C_p}\frac{\partial}{\partial t}H(r,t), \tag{2.96}$$

where $H(r,t) = \mu_a(r)\Phi(r,t)$ is the heating function, defining the thermal energy deposited at position r and time t by the laser illumination related with the optical absorption coefficient μ_a and optical radiation fluence rate Φ, C_p is the specific heat,

β is the volume expansion coefficient, and v_s is the acoustic velocity. The solution of the wave equation using Green function approach is:

$$p(r,t) = \frac{1}{4\pi v_s^2}\frac{\partial}{\partial t}\left[\frac{1}{|r-r'|}\int dr' H\left(r', t - \frac{|r-r'|}{v_s}\right)\right]. \tag{2.97}$$

According to Eq. (2.97), the detected pressure at location r and time t comes from sources over a spherical shell centered at r with a radius of $|r - r'|$. For a spherical absorber with radius a, the photoacoustic wave could have an analytical solution:

$$\begin{aligned} &p(r,t) = H(r)U(a - |R - v_s t|)(R - v_s t)/2R, \\ &\text{where } U(x) = \begin{cases} 1, & x \geq 0 \\ 0, & x < 0. \end{cases} \end{aligned} \tag{2.98}$$

Here R is the distance between the absorber and the detector. It is predicted that the pulse width of the 'N-shape' photoacoustic signal is proportional to the size of the absorber, i.e. the laser spot size when the object is much larger. In fact, the photoacoustic signal in real situation $p_r(r, t)$ also depends on the unknown object's properties, and suffering unknown acoustic channel impulse response $I(r, t)$, which could be expressed as:

$$p_r(r,t) = I(r,t) * p(r,t) + N_1(r,t), \tag{2.99}$$

where $I(r, t)$ is related with the unknown object's properties, acoustic channel's attenuation, distortion, and ultrasound transducer's frequency response. $N_1(r, t)$ is related with the additive white Gaussian noise of acoustic transmission channel. The one-way propagation delay of photoacoustic signal from the object to the detector is $\tau_p = d/v_s$ with distance d and acoustic speed v_s of 1.5 mm/μs, as shown in Fig. 2.41b. A template signal that is highly correlated with the real photoacoustic signal is to be generated. It should come from the same object, and experience the same acoustic channel impulse response and transducer's frequency response. Therefore, here we employ an external ultrasound signal $u(r, t)$, which is designed to highly resemble the photoacoustic signal: $u(r,t) \approx p(r,t)$. Practically, we can transmit a controlled ultrasound signal, which has similar waveform and spectrum as the photoacoustic signal as much as possible. Then the received pulse-echo ultrasound signal $u_r(r,t)$ is expressed as:

$$u_r(r,t) = \Gamma \times I(r,t) * u(r,t) + N_2(r,t), \tag{2.100}$$

where Γ is the reflection coefficient due to the acoustic impedance mismatch, and the round-trip propagation delay of the pulse-echo ultrasound signal is $\tau_u = 2d/v_s$, then we have $\tau_u = 2\tau_p$. According to Eqs. (2.99) and (2.100), the photoacoustic signal and ultrasound signal are highly correlated, because they are from same

object, experiencing the same acoustic channel and ultrasound transducer's same frequency response, i.e. sharing the same unknown $I(r, t)$.

In conventional photoacoustic imaging and ultrasound imaging, as well as the recently proposed dual-modality PAUS imaging, the laser-induced photoacoustic signal and pulse-echo ultrasound signal are processed separately to acquire two independent images. In this section, we propose to coherently correlate these two signals that are highly correlated based on the above analysis as shown at the bottom of Fig. 2.41b, to achieve significantly enhanced SNR and image contrast through cross-correlation:

$$\mathrm{PAUS}(r,t)=\langle u_r(r), p_r(r)\rangle(t) = \int_{-\infty}^{+\infty} u_r^*(r,t) \times p_r(r,t+\tau)d\tau. \tag{2.101}$$

Similar to coherent detection in communication, radar and sonar systems, coherent PAUS correlation is able to significantly improve the detection SNR of received signals by integrating the weak but correlated signal pattern, and suppressing the strong but uncorrelated noise and interference. Moreover, the coherent correlation between photoacoustic and pulse-echo ultrasound signals fuses optical absorption and ultrasound reflection from the same object, which is expected to significantly improve the image contrast. In addition, considering the propagation delay relationship $d = v_s\Delta\tau = v_s(\tau_u - \tau_p)$, the depth information could be extracted accurately by performing both the forward and backward cross-correlations as shown in Fig. 2.41b, where the distance between two peaks indicates the accurate depth information. Next we will demonstrate the experiments of coherent PAUS correlation and preliminary imaging results.

2.5.3 Experimental Setup

The diagram of the experimental setup for coherent PAUS correlation and imaging is shown in Fig. 2.42. A Q-switched pulsed laser (FDSS 532-1000, CryLaS, GmbH) with 532 nm wavelength and 1.8 ns pulse width is used to provide the light source. The output laser beam is attenuated by a neutral density filter (NDC-50C-2 M, Thorlabs) and then focused into the fiber collimator by a condenser lens (LB1471, Thorlabs). To handle the high peak power laser, multi-mode fiber is adopted. The output of the multi-mode fiber (MHP550L02, Thorlabs) is focused by another pair of condenser lens to a spot with 3 mm diameter, generating 'N-shape' photoacoustic signal of 0.5 MHz central frequency based on analytical solution. Then a beam splitter and a photodiode (DET10A, Thorlabs) are used to monitor the laser intensity fluctuation. The vessel-mimicking phantom is a silicone tube (outer diameter: 3 mm, inner diameter: 2.2 mm) filled with the porcine blood pumped by a syringe, which is designed to model the brain superior sagittal sinus (SSS), human's carotid, jugular with similar vessel diameter (1–5 mm) and

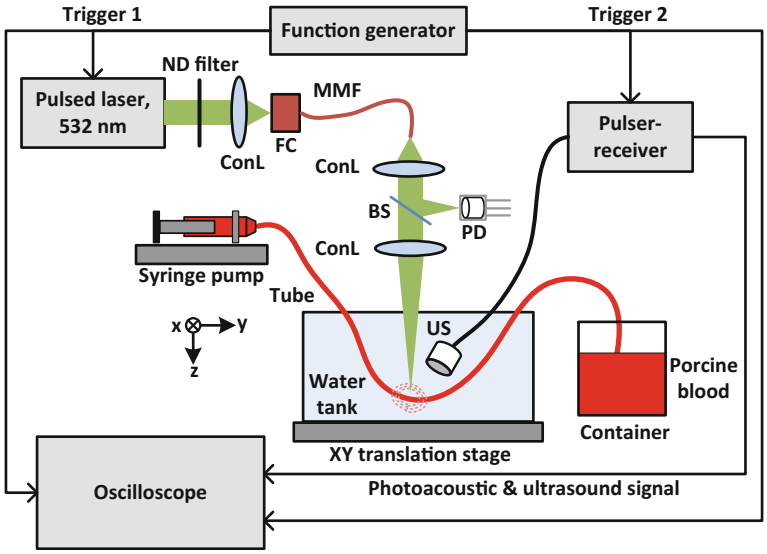

Fig. 2.42 Experimental setup of the coherent PAUS correlation and imaging. *ConL* condenser lens; *FC* fiber collimator; *MMF* multi-mode fiber; *ND* neutral density; *BS* beam splitter; *PD* photodiode; *US* ultrasound transducer

measured photoacoustic signal waveform [41, 42]. The phantom is immersed in water for optimum light transparency and acoustic coupling. A focused ultrasound transducer (V303-SU, Olympus, central frequency: 0.9 MHz, −6 dB bandwidth: 59.74%, normalized sensitivity at 0.5 MHz: 20%) driven by an ultrasound pulser-receiver (5077PR, Olympus) working in its transmission mode is used to excite the exogenous ultrasound signal, which is matched to the predicted photoacoustic signal's central frequency, and receives both the laser-induced photoacoustic wave and pulse-echo ultrasound wave with pulser-receiver working in its receiving mode sequentially and separately (In some cases, both signals can be recorded at the same time but resolved in time because they appear at different time locations). Both the pulsed laser and pulser-receiver in its transmission mode are sequentially triggered by a function generator (33250A, Agilent) with two TTL trigger signals. Then the acoustic signals received by the transducer and pulser-receiver in its receiving mode are recorded by an oscilloscope (WaveRunner 640Zi, LeCroy) and sent to PC for post data-processing. The water tank could be moved by the XY translation stage (XYR1, Thorlabs) for raster scanning to acquire imaging data. Before the measurement, laser focusing and ultrasound transducer are well aligned by manually tuning the position of the ultrasound transducer until the maximum photoacoustic signal is achieved and observed from oscilloscope. To identify the photoacoustic and pulse-echo ultrasound signals from laser burst induced jitter noise, proper time-gating is applied to remove the unwanted interference before the coherent PAUS correlation and image reconstruction. Moreover,

the laser-induced jitter noise is uncorrelated with the photoacoustic and pulse-echo ultrasound signals, and could be easily suppressed by the proposed correlated PAUS approach.

2.5.4 Results

2.5.4.1 System Evaluation

Before performing the coherent PAUS correlation and imaging experiments, the validity evaluation of the proposed system is conducted by detecting both the photoacoustic wave and ultrasound wave in high SNR situation shown in Fig. 2.43a, where the signals are aligned for intuitive comparison. The signal patterns of both photoacoustic and ultrasound waves achieve good agreement in both time domain (Fig. 2.43a) and frequency domain (Fig. 2.43b), showing the strong coherent correlation between them.

2.5.4.2 Signal SNR Improvement

Firstly to prove the feasibility of detecting the weak photoacoustic signal by cross-correlating it with a strong and correlated ultrasound signal, the separate laser-induced pulsed photoacoustic signal and pulse-echo ultrasound signal are recorded sequentially with separately triggered laser and ultrasound excitations as shown in Fig. 2.44a, b, where the photoacoustic signal is suffering low SNR (4.4 dB) due to the weak signal strength and inevitable instrumental noise. The ultrasound signal can be made relatively strong (9.6 dB) by increasing transmit power and treated as the template signal. Then based on the proposed coherent PAUS correlation approach, the photoacoustic signal and ultrasound signal are

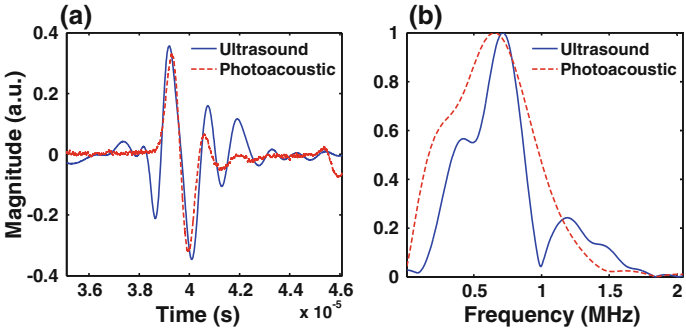

Fig. 2.43 **a** Measured time-domain photoacoustic and ultrasound signals in high SNR situation for system evaluation. **b** The spectrums of them with similar central frequency and bandwidth

cross-correlated within 6 μs time window as shown in Fig. 2.44c. The SNR of the coherent PAUS correlation signal is significantly increased to 22.5 dB due to the correlated PAUS signal integration and uncorrelated noise suppression. In the next step, to prove the feasibility of coherent PAUS correlation at a worse case, the SNR of photoacoustic signal and pulse-echo ultrasound signal are set to be below −10 dB by reducing the power of laser and ultrasound sources as shown in Fig. 2.44f, g. It shows that due to the strong noise background, both photoacoustic signal and ultrasound signal are hardly identified. After performing both the backward and forward cross-correlations within a longer window (10 μs), two peaks could be clearly identified in Fig. 2.44h to give the depth information ($d = v_s \Delta\tau = 37.5\,\text{mm}$) of the object. Finally the coherent PAUS signals in Fig. 2.44c, h are further low-pass filtered to improve the SNR and peak detection in Fig. 2.44d, i. Although proper low-pass filtering (4-order Butterworth filter with cut-off frequency at 1 MHz) of the origin photoacoustic signals in Fig. 2.44a, f could improve the signal SNR to a certain extent, which are shown in Fig. 2.44e, j, it is impossible to suppress the noise components with similar spectrum as the photoacoustic signal. On the other hand, coherent correlation behaves as a matched filter to exactly extract the highly correlated photoacoustic signal and suppresses the uncorrelated white noise, which traditional filtering process can never achieve. It is shown that the low-pass filtered PAUS signals in Fig. 2.44d, i perform much higher SNR than low-pass filtered original photoacoustic signals in Fig. 2.44e, j, especially when suffering strong background noise and interference.

To fully explore the capability of coherent PAUS correlation on SNR improvement, the input laser pulse energy is swept from 10 to 200 μJ to induce the photoacoustic signals with different SNR (from −20 to −5 dB) as shown in

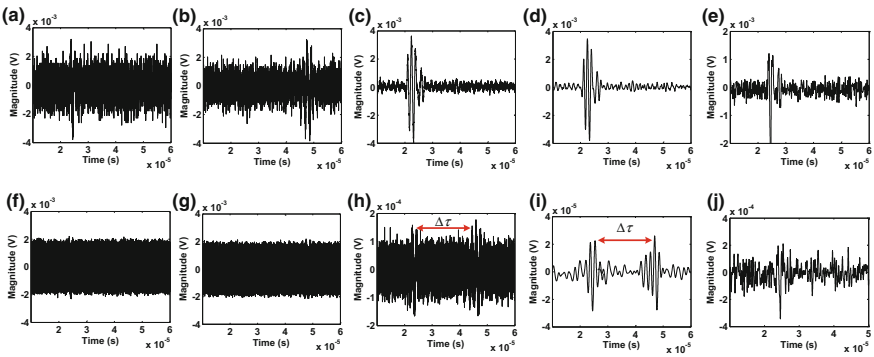

Fig. 2.44 The separately detected **a** pulsed photoacoustic wave, **b** pulse-echo ultrasound wave, and **c** the coherent PAUS correlation wave using backward cross-correlation. **d**, **e** Show the low-pass filtered signals of (**c**) and (**a**) respectively. In some extreme low signal SNR scenario, **f** pulsed photoacoustic wave, **g** pulse-echo ultrasound wave, and **h** the coherent PAUS correlation using both forward cross-correlation and backward cross-correlation. The **i**, **j** show the low-pass filtered signals of (**h**) and (**f**) respectively. Reprinted from Ref. [43] with permission from Institute of Electrical and Electronics Engineers

Fig. 2.45, where the SNR of pulse-echo ultrasound from the blood of the vessel-mimicking phantom remains 9.6 dB. It is clearly shown that over 20 dB SNR improvement is achieved by coherent PAUS correlation across a wide range of input laser energy. More interestingly, the SNR improvement is becoming more significant when the laser energy is decreasing, validating its potential to achieve a superior sensitivity when the photoacoustic signal suffers severe noisy background.

It is worth noting that only one wide ultrasound pulse is received by overlapping the four echos from the four interfaces of the vessel-mimicking phantom due to the small diameter (outer: 3 mm, inner: 2.2 mm) of the tube, and the low 0.5 MHz central frequency (>3 mm resolution) used in the experiment. Then the four ultrasound echos at 0.5 MHz are overlapped significantly and cannot be differentiated.

2.5.4.3 Image of Vessel-Mimicking Phantom

The images of the blood in the vessel-mimicking phantom (Fig. 2.46a) are created by laterally moving the object in Y axis by the XY translation stage (Fig. 2.42). The received acoustic signals are subjected to the low-pass filtering and Hilbert transformation to extract the envelope. Three comparable B-scan images of the pulsed photoacoustic imaging (Fig. 2.46b), pulse-echo ultrasound imaging (Fig. 2.46c), and the proposed coherent PAUS imaging (Fig. 2.46d) are reconstructed respectively. The slight location difference of photoacoustic image and ultrasound image is due to the wider ultrasound pulse and slight time delay difference caused by the different signal generation mechanism. As expected, the proposed coherent PAUS imaging performs much better image contrast (the different between image pixel intensity of object and background pixel intensity) than the separate photoacoustic or ultrasound imaging that may suffer strong noisy and/or low contrast background, due to coherently correlating the photoacoustic and ultrasound signals to improve

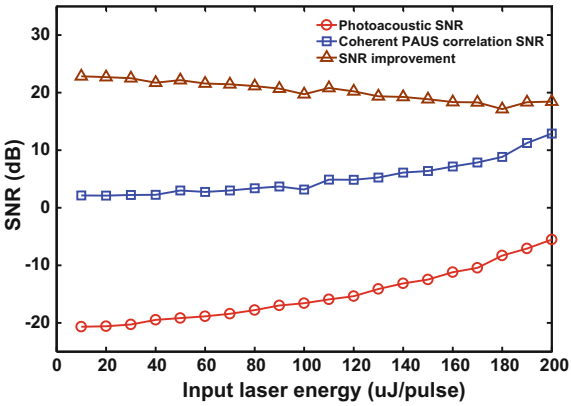

Fig. 2.45 The SNR of the photoacoustic signal, the coherent PAUS correlation signal and the SNR improvement when the input laser pulse energy is swept from 10 to 200 μJ

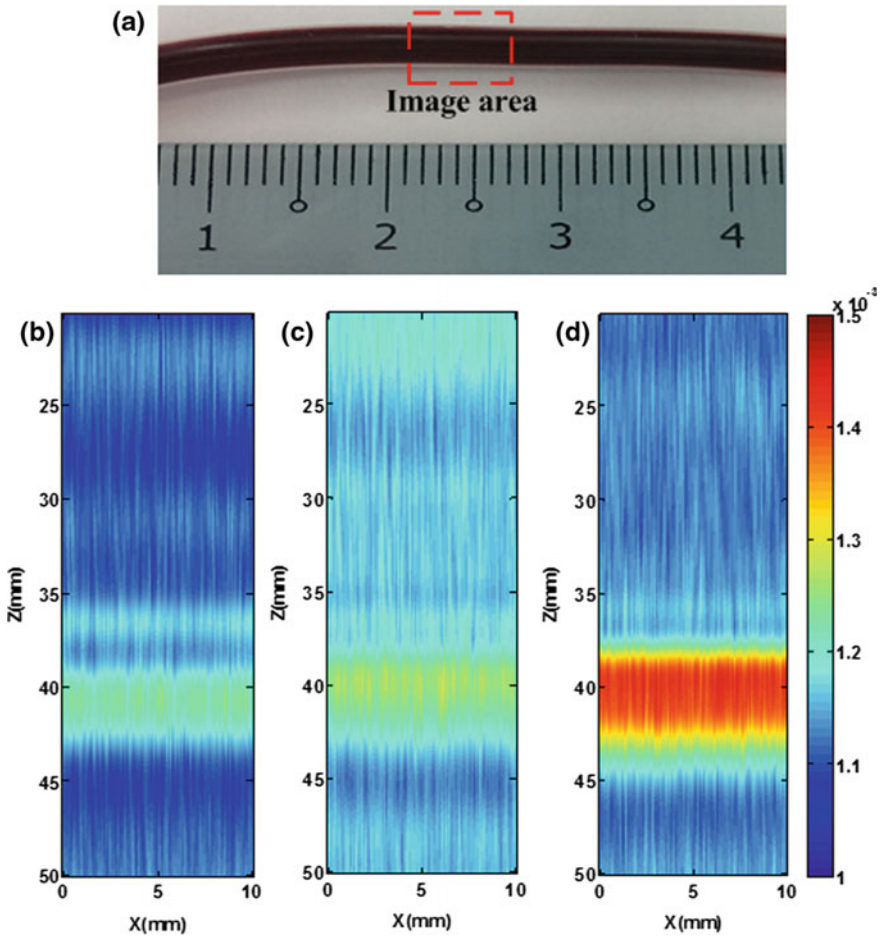

Fig. 2.46 The reconstructed images of the **a** vessel-mimicking phantom by **b** pulsed laser-induced photoacoustic imaging, **c** pulse-echo ultrasound imaging, and **d** the proposed coherent PAUS imaging. Scale bar (normalized unit). Reprinted from Ref. [43] with permission from Institute of Electrical and Electronics Engineers

the SNR, fusing both optical absorption and acoustic reflection properties of the same target. It is also observed that the axial resolution of the coherent PAUS imaging is slightly degraded. The reason is that the cross-correlation will induce more cycles than the original signals due to its time-shifted multiplication and integration processing, which leads to a bit larger pulse envelope width.

2.5.4.4 Image of Vessel-Mimicking Phantom with Random Scatterer

To validate the proposed PAUS correlation approach in a more realistic scenario, e.g. human brain SSS, carotid and jugular vessels in deep tissue, a piece of ex vivo chicken breast tissue with 5 mm thickness is placed on top of the vessel-mimicking phantom. Figure 2.47a, b shows the photograph of experimental and phantom setup. The reconstructed images of photoacoustic, pulse-echo ultrasound and the proposed correlated PAUS approach are shown in Fig. 2.47c–e, respectively. It is observed that due to the existence of the chicken breast scatterer, more distortion is induced in both photoacoustic image and ultrasound image. However, the SNR improvement is still significant by applying the coherent PAUS correlation in Fig. 2.47e.

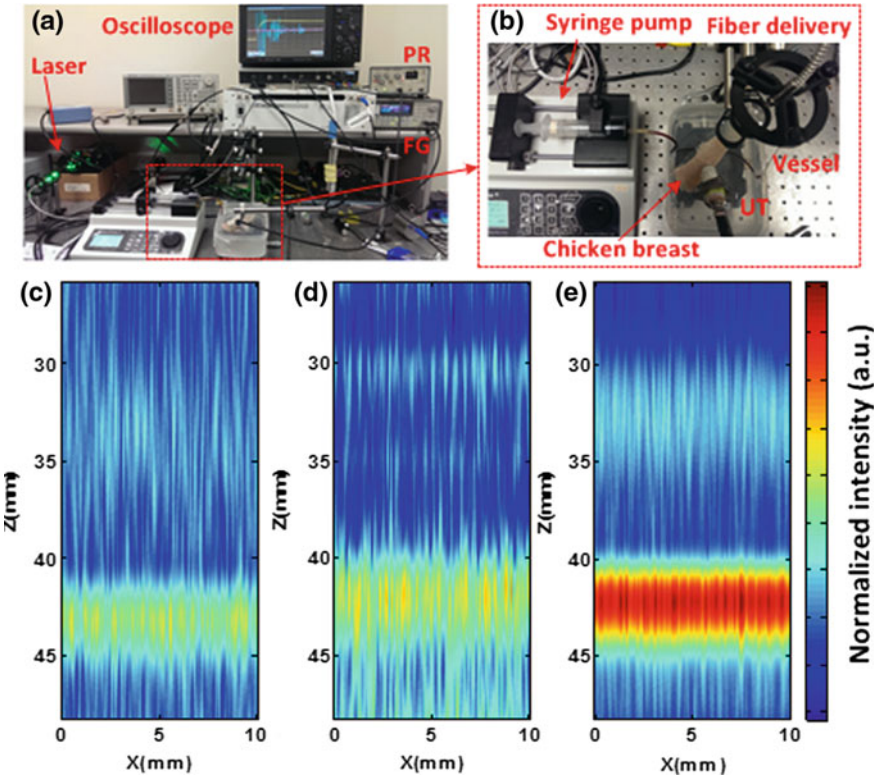

Fig. 2.47 **a**, **b** The photograph of the experiment setup and phantom. **c** Pulse-laser induced photoacoustic imaging, **d** pulse-echo ultrasound imaging, and **e** the proposed coherent PAUS imaging. *PR* pulser-receiver; *FG* function generator; *UT* ultrasound transducer. Reprinted from Ref. [43] with permission from Institute of Electrical and Electronics Engineers

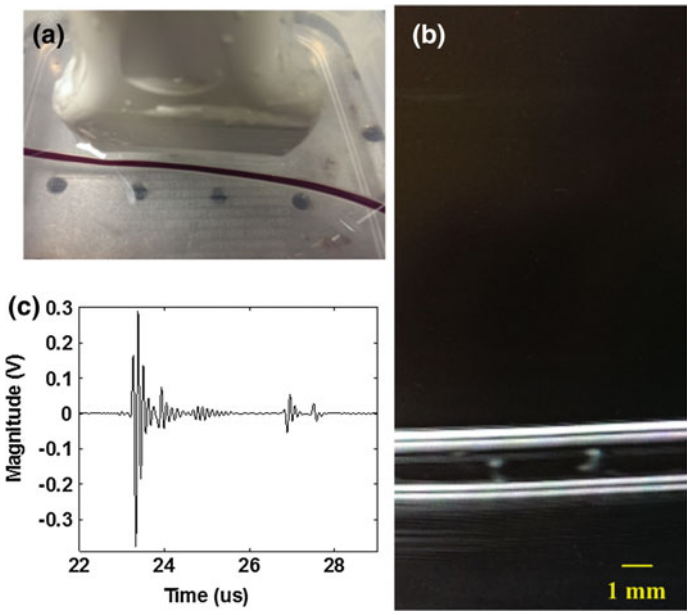

Fig. 2.48 **a** The photograph of the phantom imaged by a 10 MHz linear array ultrasound probe, and **b** the reconstructed high-resolution ultrasound image. **c** The measured raw ultrasound signal without time-gain compensation

2.5.4.5 Image of Vessel-Mimicking Phantom with High Resolution Ultrasound Imaging

To complement the images in previous section reconstructed by low-frequency signals, another ultrasound image is appended to render the detailed structure of the tube phantom in this section using Sonix RP ultrasound scanner (Ultrasonix Inc.) with 10 MHz ultrasound linear-array probe (Fig. 2.48a). The reconstructed image of the vessel-mimicking phantom is shown in Fig. 2.48b, where the vessel walls and blood inside are clearly differentiated. A typical time-domain ultrasound signal at 10 MHz central frequency is shown in Fig. 2.48c, showing coherent waveform pattern with that in Fig. 2.43a. It proves the feasibility of the coherent PAUS approach to be applied in high-resolution imaging applications, e.g. subcutaneous vascular imaging [44] intravascular imaging [39], and retinal imaging [45], with both high-frequency photoacoustic and ultrasound signals.

2.5.5 Discussion and Conclusion

The primary application of the proposed coherent PAUS approach is related with photoacoustic tomography for deep tissue imaging. A typical application is brain

imaging with intact scalp [42, 46]. Due to the deep imaging depth and much stronger attenuation (~6.9 dB/(MHz·cm)) of high-frequency component of photoacoustic signal than its low-frequency component caused by the scalp, only low-frequency signals could be survived and detected by the transducer with <5 MHz frequency. Low sensitivity and signal SNR are the key bottleneck of such applications to be used in human brain. Other applications also include carotid/jugular imaging with >2 cm penetration depth [41]. In these applications, the imaged vessels (sheep superior sagittal sinus (SSS), human's carotid, jugular, radial artery, etc.) have a diameter range between 1 and 5 mm, where the detected photoacoustic signals have frequency spectrum from hundreds of kHz to 1 MHz, which are close to the vessel-mimicking phantom used in this section. Therefore, the proposed PAUS coherent imaging approach is primarily targeting this kind of application, where low sensitivity and signal SNR are the critical challenges, and low-frequency photoacoustic signals are usually detected. To coherently correlate with the weak photoacoustic signal, low-frequency ultrasound signal is chosen to match the spectrum of the photoacoustic signal to maximize the SNR improvement of the proposed PAUS coherent imaging.

Another important application is related with high-resolution photoacoustic microscopic imaging. Typical applications include subcutaneous vascular imaging, endoscopic, intravascular imaging, and retinal imaging. Due to the small imaging depth and better optical focusing, high-frequency photoacoustic signal is induced to render high-resolution images, where the sensitivity and signal SNR are not critically challenging compared with above deep tissue imaging. Again, the proposed PAUS coherent imaging is also applicable to achieve enhanced sensitivity and signal SNR for such high resolution applications, which can be fully explored in the future work.

In conclusion, we have conducted the initial study on the coherent correlation of endogenous photoacoustic wave and exogenous pulse-echo ultrasound wave. Due to the coherent correlation of the optical absorption and acoustic reflection properties from the same object, the experimentally detected PAUS correlation signal achieved significantly enhanced SNR than conventional pulsed photoacoustic or pulse-echo ultrasound signals. Preliminary imaging results demonstrated much improved image contrast by the proposed coherent PAUS correlation imaging approach. The proposed PAUS correlation could be treated as a new imaging modality fusing mechanical impedance, optical absorption and thermoelastic properties of the same object, delivering higher sensitivity and image contrast than existing ultrasound or photoacoustic imaging only. Except the anatomical image acquired in this section, functional information (e.g. blood oxygen saturation) could also be extracted by applying multi-wavelength laser illumination to excite distinct photoacoustic signals. Functional coherent PAUS imaging with dedicated calibration will be explored further. Future work will also focus on the 3D PAUS imaging implementation for in vivo small animal studies.

2.6 Micro-Doppler EM-Acoustic Effect and Detection

In recent years, photoacoustics has attracted intensive research to improve biomedical imaging modalities. However, the physical interaction between photoacoustic generated waves with an additional ultrasound wave is a largely unexplored area. In this section, we report initial results on the interaction of photoacoustic and external ultrasound waves leading to a micro-Doppler photoacoustic (mDPA) effect, which is experimentally observed and consistently modelled. It is based on a simultaneous excitation of the target with a pulsed laser and continuous wave (CW) ultrasound. The thermoelastically induced expansion modulates the CW ultrasound and leads to transient Doppler frequency shift. The reported mDPA effect can be described as frequency modulation of the intense CW ultrasound carrier through photoacoustic vibrations. The technique opens the possibility to avoid acoustic distortions limiting state-of-the-art pulsed photoacoustic imaging systems.

2.6.1 Introduction

Photoacoustic effect refers to the light-induced acoustic generation discovered by Alexander Bell in 1880. Based on photoacoustic effect, both photoacoustic microscopy (PAM) and photoacoustic tomography (PAT) have attracted increasing interest in recent years on multi-scale biomedical imaging research, ranging from molecular imaging of biomarkers to whole body imaging of small animals, which is introduced in Chap. 1. PAM and PAT circumvent the penetration depth limitation of conventional optical imaging modalities due to optical diffusion by listening to thermoelastically induced photoacoustic signals. In a typical photoacoustic imaging application, a nanosecond pulsed laser is employed to illuminate the biological tissue non-specifically. Upon optical absorption and heating of endogenous chromophores (melanin, haemoglobin, etc.), transient acoustic waves are launched due to thermoelastic expansion. However, due to the low energy conversion efficiency of this process, acoustic attenuation, and scattering in heterogeneous biological tissues, the received acoustic signal is usually very weak and severely distorted, limiting the endogenous contrast and resolution in photoacoustic imaging.

To enhance the signal-to-noise ratio (SNR), the pulse energy of laser may be increased, yet this is limited by the ANSI laser exposure standard for human safety (<20 mJ/cm^2 at 532 nm wavelength). The most commonly used approaches are pre-amplification of the signal and averaging after multiple data acquisition. The signal enhancement this way is still limited by long acquisition time, and the hardware's performance, e.g. limited gain and bandwidth and unavoidable instrument noise. Contrast-enhanced photoacoustic imaging is studied extensively with the help of exogenous contrast agents, such as nanoparticles [47, 48], carbon nanotubes [49], and vaporized nanodroplets [50]. The problems encountered with

these engineered contrast agents are their limited optical absorption and issues with toxicity. Besides increasing contrast, acoustic distortion in heterogeneous tissues is mostly addressed through algorithm re-design [51, 52].

Here we report on a photoacoustic detection technique, which increases the sensitivity without adding agents and avoids some of the distortions photoacoustics is plagued. This is achieved by combining endogenous induced photoacoustic vibration and exogenous excited ultrasound, abbreviated as photoacoustic-ultrasound interaction. More specifically, a pulsed laser illumination and CW ultrasound driving are utilized simultaneously, then it was observed that endogenous induced photoacousic vibration can modulate the exogenous excited ultrasound wave in terms of Doppler frequency shift. Next, the detailed working principle will be discussed.

2.6.2 Method and Preliminary Results

Here we transmit the CW ultrasound and receive the backscattering ultrasound from an optical-absorbing object, which is excited with a laser to emit a photoacoustic pulse at the same time. Because the photoacoustic effect imparts a transient velocity change to the object due to thermoelastic expansion, the frequency of received CW ultrasound will be shifted due to Doppler effect. Being different from photoacoustic Doppler effect caused by bulk translation of the target at a constant velocity [53–55], the frequency shift induced by the mechanical vibration or rotation of the target is termed as micro-Doppler effect [56]. Interestingly, here we treat the photoacoustic effect as a thermoelastic mechanical vibration induced by pulsed laser illumination at the optical absorber site, rather than conventional photoacoustic wave directly detected by ultrasound transducer, see Fig. 2.49a. Therefore, photoacoustic induced thermoelastic vibrations will modulate the frequency of the received CW ultrasound wave, which we define as micro-Doppler photoacoustic (mDPA) effect. As shown in Fig. 2.49b, the model of the mDPA effect is simplified to be a plane CW ultrasound wave with frequency f_0 hitting on a round-shape target with diameter R. The transient velocity vector $\vec{V}_{PA}$ of the photoacoustic vibration is proportional to the derivative of the photoacoustic pressure $p(t)$ expressed as:

$$V_{PA}(t) = \kappa_s R \frac{\partial p(t)}{\partial t} \tag{2.102}$$

where κ_s is the adiabatic compressibility. Then the transient micro-Doppler frequency shift can be expressed as:

$$f_{mDPA} = 2f_0 \frac{V_{PA}(t)}{c} \cos\theta = \frac{2f_0 \kappa_s R}{c} \frac{\partial p(t)}{\partial t} \cos\theta \tag{2.103}$$

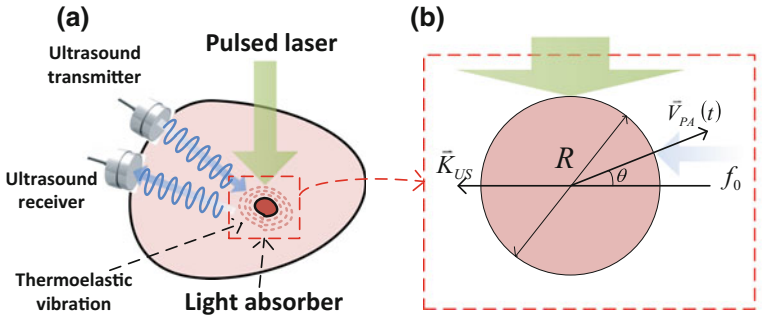

Fig. 2.49 The mDPA effect and modeling. **a** Fundamentals of photoacoustics-ultrasound interaction when light absorber is illuminated by both pulsed laser and CW ultrasound simultaneously. mDPA effect occurs when the laser-induced thermoelastic vibration modulates the CW ultrasound in terms of micro-Doppler frequency shift. **b** Simplified round-shape model of the light absorber with diameter *R*. Laser illumination is from *top side*, and ultrasound excitation is from *right side*

where θ is the photoacoustic vibration angle annotated in Fig. 2.49b. From Eq. (2.103) it is observed that the micro-Doppler frequency shift f_{mDPA} is proportional to the derivative of the photoacoustic pressure $p(t)$, showing the feasibility of extracting the photoacoustic information from the micro-Doppler frequency shift of the ultrasound transmitter/receiver.

The discovered mDPA effect allows the weak and wideband pulsed photoacoustic signal to be carried by the intensive narrowband ultrasound wave, retaining much stronger immunity against acoustic attenuation and distortion in heterogeneous acoustic channel such as biological tissues.

Next we will experimentally test if this Doppler shift can be picked up (Fig. 2.50). The setup consist of a Q-switched Nd: YAG laser at 532 nm emitting single laser pulses with 7 ns pulse width (Orion, New Wave, Inc). The collimated laser beam with 2 mm diameter spot size is guided onto a silicone tube immersed in water filled with diluted blue ink (Pelikan, $\mu_a = \sim 100\,\mathrm{cm}^{-1}$) pumped with a syringe pump. Two US transceiver systems are used. First a wideband ultrasound transducer (V323-SU, 2.25 MHz, 6 mm in diameter; Olympus) is adopted to receive the photoacoustic wave conventionally and acts as a reference. It is connected to a preamplifier (54 dB gain, model 5662; Olympus) and the signal is recorded with an oscilloscope (500 MHz sampling rate, WaveMaster 8000A; LeCroy). The data is 20 times averaged. The second transceiver system is running simultaneously using a dual-element ultrasound transducer (5 MHz, 6 mm in diameter, DHC711-RM; Olympus). It operates as an ultrasound radar, transmitting and receiving CW ultrasound by its dual elements. A 5 MHz sine wave generated from a function generator is fed into a power amplifier (250 W; BT00200-AlphaSA-CW, Tomcorf) to drive the transmitting element. The receiving element is directly connected to the oscilloscope for data recording. Both the wideband and dual-element transducers are

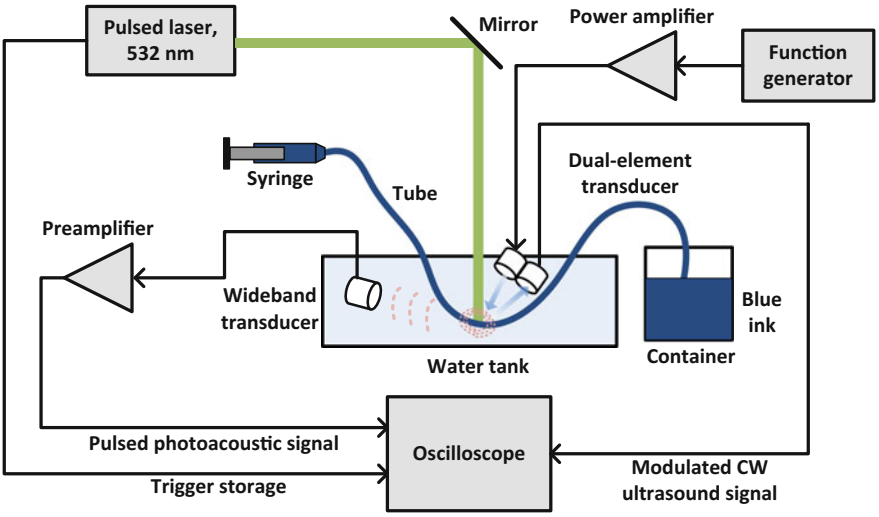

Fig. 2.50 Diagram of the experimental setup for the detection of conventional pulsed photoacoustic signal and CW ultrasound modulated by the micro-Doppler photoacoustic effect

placed near the testing tube at a distance of 4.5 cm. A synchronization signal from the pulsed laser is used to trigger the data acquisition of the oscilloscope.

To extract the micro-Doppler frequency shifted from the received ultrasound signal, band-pass filtering and down-conversion technique are employed, which multiplies the received ultrasound wave (Fig. 2.51c, d) $US(t) = A_{US}\sin[2\pi(f_0 + f_{mDPA})t]$ with a reference signal $R(t) = A_R\cos[2\pi f_0 t]$. Here A_{US} and A_R are the respective amplitudes. Then we apply low-pass filtering:

$$\begin{aligned} mDPA(t) &= US(t)R(t) = A_{US}A_R\sin[2\pi(f_0 + f_{mDPA})t]\cos[2\pi f_0 t] \\ &= \frac{1}{2}A_{US}A_R\sin[2\pi(2f_0 + f_{mDPA})t] + \frac{1}{2}A_{US}A_R\sin[2\pi f_{mDPA}t] \\ &\xrightarrow{Low-pass\ filtering} \frac{1}{2}A_{US}A_R\sin[2\pi f_{mDPA}t] \xrightarrow{small-angle\ approximation} A_{US}A_R\pi f_{mDPA}t \\ &= \frac{2\pi f_0\kappa_s RA_{US}A_R}{c}\cos\theta\frac{\partial p(t)}{\partial t}t = K\frac{\partial p(t)}{\partial t}t \end{aligned} \tag{2.104}$$

where small-angle approximation is applicable due to the much shorter duration of photoacoustic wave than mDPA period, and $K = 2\pi f_0\kappa_s RA_{US}A_R\cos\theta/c$ is assumed to be the mDPA conversion constant. Both photoacoustic (PA) wave (Fig. 2.51f) and mDPA wave (Fig. 2.51e) detected by conventional pulsed photoacoustic system (Fig. 2.51b) and the proposed mDPA system (Fig. 2.51a) respectively, indicate the photoacoustic source located 4.5 cm away with a delay of about 30 μs.

The extracted mDPA signal amplitude is proportional to the derivative of the photoacoustic pressure according to Eq. (2.104), so it is also expected to reveal the

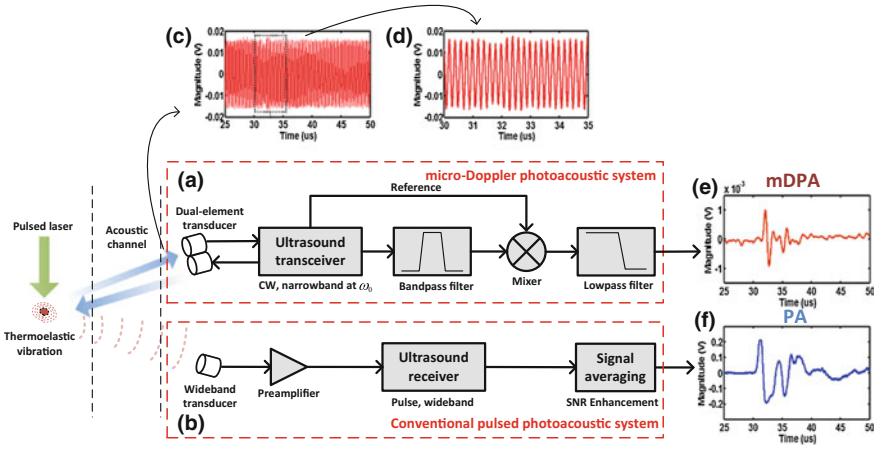

Fig. 2.51 The mDPA and pulsed photoacoustic system. **a** Micro-Doppler photoacoustic system, and **b** conventional pulsed photoacoustic system. **c**, **d** Received CW ultrasound signal with frequency modulation by micro-Doppler photoacoustic effect, and **e** recovered micro-Doppler photoacoustic signal. **f** Conventional pulsed photoacoustic signal. Reprinted from Ref. [57] with permission from Institute of Electrical and Electronics Engineers

optical absorption coefficient as the conventional photoacoustic pressure does. The laser pulse energy is varied from 20 to 90 μJ, to validate that the normalized amplitude of the mDPA wave has a good agreement with the amplitude of conventional photoacoustic wave for optical absorption measurement as shown in Fig. 2.52.

To compare the sensitivity of the proposed mDPA system with a conventional pulsed photoacoustic system, pre-amplification and averaging are removed from both the mDPA system and the conventional pulsed photoacoustic system. At the source site as shown on the left side of Fig. 2.53a, both the mDPA signal and the

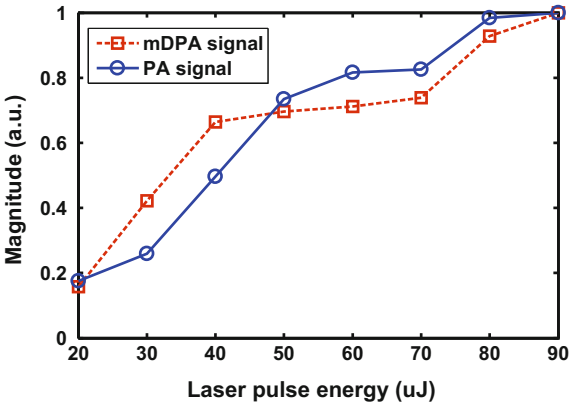

Fig. 2.52 Normalized amplitude comparison of micro-Doppler photoacoustic (mDPA) signal and pulsed photoacoustic (PA) signal by varying the laser pulse energy. Reprinted from Ref. [57] with permission from Institute of Electrical and Electronics Engineers

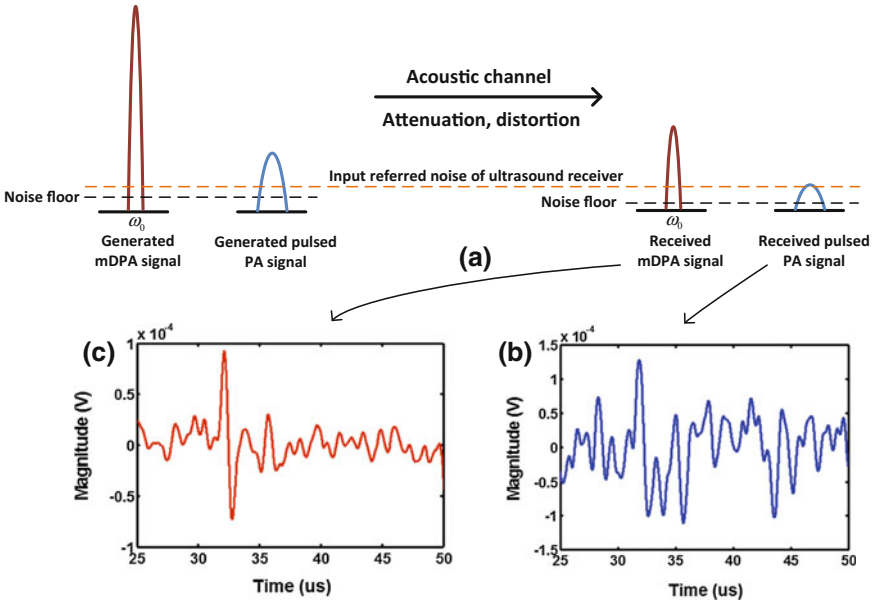

Fig. 2.53 SNR analysis of mDPA versus pulsed photoacoustic signals. **a** Signal and noise levels of micro-Doppler photoacoustic and pulsed photoacoustic signals before and after acoustic channel. **b** Waveform of received pulsed photoacoustic signal, and **c** recovered mDPA signal. The mDPA signal detection retains data higher SNR than conventional pulsed photoacoustic detection. Reprinted from Ref. [57] with permission from Institute of Electrical and Electronics Engineers

pulsed photoacoustic signal are detectable above the noise floor. However, after acoustic attenuation and distortion during the propagation, the amplitude of the pulsed photoacoustic signal is below the input referred noise of ultrasound receiver, which is equivalently to the base-line noise floor of the oscilloscope used in the experiment as shown on the right of Fig. 2.53a. Therefore, the pulsed photoacoustic wave can be hardly detected in presence of the background noise (Fig. 2.53b). On the other hand, the mDPA system is still capable of recovering the photoacoustic information (Fig. 2.53c), for the reason that photoacoustic vibrations modulate the intense CW ultrasound wave in terms of micro-Doppler frequency shift. The modulated CW ultrasound wave reserves the high intensity and the narrow bandwidth, which allows band-pass filtering with high quality factor (Q) to significantly suppress the noise. The experimental result shows higher signal SNR (14 dB) and fidelity than pulsed photoacoustic signal SNR (2.5 dB) during its propagation in acoustic channel.

2.6.3 Discussion and Conclusion

To further illustrate the feature and advantage of the proposed mDPA system, it is interesting to make an analogy between the photoacoustic detection system and the well-established telecommunication system. More specifically, pulsed photoacoustic detection is similar with amplitude modulation (AM) communication system, where information is carried in terms of signal's amplitude. On the other hand, the proposed mDPA detection can be related to a frequency modulation (FM) communication system, where information is carried in terms of signal's frequency shift. According to communication theory, FM systems are far better at rejecting noise as compared to AM system: the noise is distributed uniformly in frequency and varies randomly in amplitude. Therefore, the FM system is inherently immune to the random noise due to its narrowband characteristics and high Q band-pass filtering, guaranteeing the superior advantages of the FM mDPA system over conventional AM pulsed photoacoustic system.

In summary, initial photoacoustics-ultrasound interaction is studied to experimentally observe the mDPA effect. Simultaneous illuminating the object by pulsed laser and CW ultrasound leads to the micro-Doppler frequency modulation of CW ultrasound induced by transient thermoelastic expansion and vibration. Second, based on the mDPA effect, a new photoacoustic detection system, termed micro-Doppler photoacoustic system, is proposed to extract the photoacoustic information from the received modulated CW ultrasound signal through down-conversion technique. Due to the mDPA effect, the weak and wideband photoacoustic signal is modulated onto the CW ultrasound carrier in terms of micro-Doppler frequency shift. Taking advantage of CW ultrasound's high intensity and narrowband spectrum, it retains much stronger immunity than the pulsed photoacoustic signal against the acoustic attenuation and distortion suffered during its propagation in the heterogeneous acoustic channel. Comparison studies demonstrate that mDPA signal achieves much higher signal-to-noise (SNR) ratio and fidelity than conventional pulsed photoacoustic system. It is highly expected that an imaging system based on mDPA effect will outperform the conventional pulsed photoacoustic imaging, which will be studied in the future work.

References

1. Gao F, Zheng Q, Zheng Y (2014) Electrical circuit modeling and analysis of microwave acoustic interaction with biological tissues. Med Phys 41
2. Gao F, Zheng Q, Zheng YJ (2014) Electrical circuit modeling and analysis of microwave acoustic interaction with biological tissues. Med Phys 41
3. Fisher AR, Schissler AJ, Schotland JC (2007) Photoacoustic effect for multiply scattered light. Phys Rev E 76
4. Lazebnik M, Popovic D, McCartney L, Watkins CB, Lindstrom MJ, Harter J et al (2007) A large-scale study of the ultrawideband microwave dielectric properties of normal, benign and malignant breast tissues obtained from cancer surgeries. Phys Med Biol 52:6093–6115

5. Gao F, Zheng YJ (2012) A correlated microwave-acoustic imaging method for early-stage cancer detection. In: 2012 annual international conference of the IEEE engineering in medicine and biology society (Embc), pp 480–483
6. Kirshin E, Oreshkin B, Zhu GK, Popovic M, Coates M (2013) Microwave radar and microwave-induced thermoacoustics: dual-modality approach for breast cancer detection. IEEE Trans Biomed Eng 60:354–360
7. Karpiouk AB, Aglyamov SR, Mallidi S, Shah J, Scott WG, Rubin JM et al (2008) Combined ultrasound and photoacoustic imaging to detect and stage deep vein thrombosis: phantom and ex vivo studies. J Biomed Opt 13
8. Niederhauser JJ, Jaeger M, Lemor R, Weber P, Frenz M (2005) Combined ultrasound and optoacoustic system for real-time high-contrast vascular imaging in vivo. IEEE Trans Med Imaging 24:436–440
9. Amineh RK, Ravan M, Trehan A, Nikolova NK (2011) Near-field microwave imaging based on aperture raster scanning with TEM horn antennas. IEEE Trans Antennas Propag 59:928–940
10. Maslov K, Wang LV (2008) Photoacoustic imaging of biological tissue with intensity-modulated continuous-wave laser. J Biomed Opt 13
11. Gao F, Feng X, Zheng Y (2014) Photoacoustic phasoscopy super-contrast imaging. Appl Phys Lett 104
12. Gao F, Zheng YJ, Wang DF (2012) Microwave-acoustic phasoscopy for tissue characterization. Appl Phys Lett 101
13. Li CH, Wang LHV (2009) Photoacoustic tomography and sensing in biomedicine. Phys Med Biol 54:R59–R97
14. Gabriel C, Gabriel S, Corthout E (1996) The dielectric properties of biological tissues. 1. Literature survey. Phys Med Biol 41:2231–2249
15. Gabriel S, Lau RW, Gabriel C (1996) The dielectric properties of biological tissues. 2. Measurements in the frequency range 10 Hz to 20 GHz. Phys Med Biol 41:2251–2269
16. Gabriel S, Lau RW, Gabriel C (1996) The dielectric properties of biological tissues. 3. Parametric models for the dielectric spectrum of tissues. Phys Med Biol 41:2271–2293
17. Xu MH, Wang LHV (2006) Photoacoustic imaging in biomedicine. Rev Sci Instrum 77
18. Wang LHV, Zhao XM, Sun HT, Ku G (1999) Microwave-induced acoustic imaging of biological tissues. Rev Sci Instrum 70:3744–3748
19. Razansky D, Distel M, Vinegoni C, Ma R, Perrimon N, Koster RW et al (2009) Multispectral opto-acoustic tomography of deep-seated fluorescent proteins in vivo. Nat Photon 3:412–417
20. Jiang Y, Forbrich A, Harrison T, Zemp RJ (2012) Blood oxygen flux estimation with a combined photoacoustic and high-frequency ultrasound microscopy system: a phantom study. J Biomed Opt 17
21. Jose J, Willemink RGH, Resink S, Piras D, van Hespen JCG, Slump CH et al (2011) Passive element enriched photoacoustic computed tomography (PER PACT) for simultaneous imaging of acoustic propagation properties and light absorption. Opt Express 19:2093–2104
22. Subochev P, Katichev A, Morozov A, Orlova A, Kamensky V, Turchin I (2012) Simultaneous photoacoustic and optically mediated ultrasound microscopy: phantom study. Opt Lett 37:4606–4608
23. Zhang HF, Wang J, Wei Q, Liu T, Jiao SL, Puliafito CA (2010) Collecting back-reflected photons in photoacoustic microscopy. Opt Express 18:1278–1282
24. Zhang XY, Zhang HF, Jiao SL (2012) Optical coherence photoacoustic microscopy: accomplishing optical coherence tomography and photoacoustic microscopy with a single light source. J Biomed Opt 17
25. Li XQ, Xi L, Jiang RX, Yao L, Jiang HB (2011) Integrated diffuse optical tomography and photoacoustic tomography: phantom validations. Biomed Opt Express 2:2348–2353
26. Yin L, Wang Q, Zhang QZ, Jiang HB (2007) Tomographic imaging of absolute optical absorption coefficient in turbid media using combined photoacoustic and diffusing light measurements. Opt Lett 32:2556–2558

27. Gao F, Zheng YJ, Feng XH, Ohl CD (2013) Thermoacoustic resonance effect and circuit modelling of biological tissue. Appl Phys Lett 102
28. Gao F, Feng X, Zheng Y, Ohl C-D (2014) Photoacoustic resonance spectroscopy for biological tissue characterization. J Biomed Opt 19:067006
29. Lou CG, Xing D (2010) Photoacoustic measurement of liquid viscosity. Appl Phys Lett 96
30. Gao F, Zheng Y, Feng X, Ohl C-D (2013) Thermoacoustic resonance effect and circuit modelling of biological tissue. Appl Phys Lett 102:063702
31. Gao GD, Yang SH, Xing D (2011) Viscoelasticity imaging of biological tissues with phase-resolved photoacoustic measurement. Opt Lett 36:3341–3343
32. Treeby BE, Cox BT (2010) k-Wave: MATLAB toolbox for the simulation and reconstruction of photoacoustic wave fields. J Biomed Opt 15
33. Treeby BE, Jaros J, Rendell AP, Cox BT (2012) Modeling nonlinear ultrasound propagation in heterogeneous media with power law absorption using a k-space pseudospectral method. J Acoust Soc Am 131:4324–4336
34. Gao F, Feng X, Zheng Y (2015) Photoacoustic elastic oscillation and characterization. Opt Express 23:20617–20628
35. Beatty CH, Bocek RM, Peterson RD (1963) Metabolism of red and white muscle fiber groups. Am J Physiol 204:939
36. Gao F, Feng X, Zheng Y, Coherent photoacoustic-ultrasound correlation and imaging. IEEE Trans Biomed Eng 1
37. Kothapalli SR, Ma TJ, Vaithilingam S, Oralkan O, Khuri-Yakub BT, Gambhir SS (2012) Deep tissue photoacoustic imaging using a miniaturized 2-D capacitive micromachined ultrasonic transducer array. IEEE Trans Biomed Eng 59:1199–1204
38. Yang JM, Favazza C, Chen RM, Yao JJ, Cai X, Maslov X et al (2012) Simultaneous functional photoacoustic and ultrasonic endoscopy of internal organs in vivo. Nat Med 18:1297
39. Wei W, Li X, Zhou QF, Shung KK, Chen ZP (2011) Integrated ultrasound and photoacoustic probe for co-registered intravascular imaging. J Biomed Opt 16
40. Turin GL (1960) An introduction to matched-filters. IRE Trans Inform Theory 6:311–329
41. Dima A, Ntziachristos V (2012) Non-invasive carotid imaging using optoacoustic tomography. Opt Express 20:25044–25057
42. Petrov IY, Petrov Y, Prough DS, Cicenaite I, Deyo DJ, Esenaliev RO (2012) Optoacoustic monitoring of cerebral venous blood oxygenation though intact scalp in large animals. Opt Express 20:4159–4167
43. Gao F, Feng XH, Zheng YJ (2014) Coherent photoacoustic-ultrasound correlation and imaging. IEEE Trans Biomed Eng 61:2507–2512
44. Zhang HF, Maslov K, Stoica G, Wang LHV (2006) Functional photoacoustic microscopy for high-resolution and noninvasive in vivo imaging. Nat Biotechnol 24:848–851
45. Jiao SL, Jiang MS, Hu JM, Fawzi A, Zhou QF, Shung KK et al (2010) Photoacoustic ophthalmoscopy for in vivo retinal imaging. Opt Express 18:3967–3972
46. Wang XD, Pang YJ, Ku G, Xie XY, Stoica G, Wang LHV (2003) Noninvasive laser-induced photoacoustic tomography for structural and functional in vivo imaging of the brain. Nat Biotechnol 21:803–806
47. Kircher MF, de la Zerda A, Jokerst JV, Zavaleta CL, Kempen PJ, Mittra E et al (2012) A brain tumor molecular imaging strategy using a new triple-modality MRI-photoacoustic-Raman nanoparticle. Nat Med 18:829-U235
48. Galanzha EI, Shashkov EV, Kelly T, Kim JW, Yang LL, Zharov VP (2009) In vivo magnetic enrichment and multiplex photoacoustic detection of circulating tumour cells. Nat Nanotechnol 4:855–860
49. De La Zerda A, Zavaleta C, Keren S, Vaithilingam S, Bodapati S, Liu Z et al (2008) Carbon nanotubes as photoacoustic molecular imaging agents in living mice. Nat Nanotechnol 3:557–562

50. Wilson K, Homan K, Emelianov S (2012) Biomedical photoacoustics beyond thermal expansion using triggered nanodroplet vaporization for contrast-enhanced imaging. Nat Commun 3
51. Dean-Ben XL, Ma R, Rosenthal A, Ntziachristos V, Razansky D (2013) Weighted model-based optoacoustic reconstruction in acoustic scattering media. Phys Med Biol 58:5555–5566
52. Huang C, Nie LM, Schoonover RW, Guo ZJ, Schirra CO, Anastasio MA et al (2012) Aberration correction for transcranial photoacoustic tomography of primates employing adjunct image data. J Biomed Opt 17
53. Fang H, Maslov K, Wang LV (2007) Photoacoustic doppler effect from flowing small light-absorbing particles. Phys Rev Lett 99
54. Fang H, Maslov K, Wang LV (2007) Photoacoustic Doppler flow measurement in optically scattering media. Appl Phys Lett 91
55. Wang LD, Xia J, Yao JJ, Maslov KI, Wang LHV (2013) Ultrasonically encoded photoacoustic flowgraphy in biological tissue. Phys Rev Lett 111
56. Chen VC, Li FY, Ho SS, Wechsler H (2006) Micro-doppler effect in radar: phenomenon, model, and simulation study. IEEE Trans Aerospace Electron Syst 42:2–21
57. Gao F, Feng X, Zheng Y (2016) Micro-Doppler photoacoustic effect and sensing by ultrasound radar. IEEE J Sel Top Quant Electron 22:1–6

Chapter 3
Multi-wave EM-Acoustic Applications

In this chapter, several interesting applications of the EM-Acoustic sensing and imaging will be introduced with innovative approach. In Sect. 3.1, a correlated microwave-acoustic imaging approach is proposed by fusing scattered microwave and thermoacoustic image to deliver higher image contrast for early-stage breast cancer detection, which is proved with numerical simulation results. In Sect. 3.2, a novel single-wavelength approach is proposed to detect the blood oxygen saturation (SO_2), where both scattered optical wave and photoacoustic wave are collected and correlated. Phantom studies are performed to validate its feasibility. In Sect. 3.3, a photoacoustic-guided depth-resolved Raman spectroscopy approach is proposed for skin cancer diagnosis, which is experimentally validated on multi-layer phantom. In Sect. 3.4, a multistatic photoacoustic classification approach is proposed to characterize malignant and benign tumors, which is challenging for conventional photoacoustic tomography for deep tissue imaging.

3.1 Correlated Microwave-Acoustic Imaging for Breast Cancer Detection

Microwave-based imaging technique shows large potential in detecting early-stage cancer due to significant dielectric contrast between tumor and surrounding healthy tissue. In this section, we present a new way named Correlated Microwave-Acoustic Imaging (CMAI) of combining two microwave-based imaging modalities: confocal microwave imaging (CMI) by detecting scattered microwave signal, and microwave-induced thermo-acoustic imaging (TAI) by detecting induced acoustic signal arising from microwave energy absorption and thermal expansion. Necessity of combining CMI and TAI is analyzed theoretically, and by applying simple algorithm to CMI and TAI separately, we propose an image correlation approach merging CMI and TAI together to achieve better performance in terms of resolution and contrast. Preliminary numerical simulation shows promising results in case of

F. Gao, *Multi-wave Electromagnetic-Acoustic Sensing and Imaging*,
Springer Theses, DOI 10.1007/978-981-10-3716-0_3

low contrast and large variation scenarios. A UWB transmitter is designed and tested for future complete system implementation. This preliminary study inspires us to develop a new medical imaging modality CMAI to achieve real-time, high resolution and high contrast simultaneously. The results of this section have been published in *Proc. EMBC 2012* [1].

3.1.1 Introduction

Early detection is very important for effective treatment of cancer. Previous studies have shown that at microwave frequencies, the dielectric properties of cancerous tumor is much different from the healthy tissue, which is the basis of microwave-based imaging method for cancer diagnosis [2, 3]. By detecting the large dielectric contrast, various microwave-based imaging modalities have been proposed, among which, confocal microwave imaging (CMI) and microwave-induced thermo-acoustic imaging (TAI) are attracting significant attentions in recent years. Compared with microwave tomography that is solving a scattering inverse problem to reconstruct the dielectric distribution, CMI is using antenna array to transmit UWB pulse alternately and receive the scattered signals at different locations. Tumor could be detected from these received signals by various beamforming techniques [4, 5]. Interestingly, apart from the scattering caused by dielectric difference of tumor, energy absorption also exists when microwave is propagating in the tissue. Due to higher water content in tumor, it absorbs more microwave energy than surrounding healthy tissue. Following tissue heating, thermo-acoustic expansion and tissue vibration, acoustic signals are generated and eradiating to the surface of the body, which are detected by the ultrasound transducers placed around the objective sample [6, 7]. The received acoustic signals carrying the information of tissue EM absorption, could also be used for tumor detection. Through detecting the scattered microwave signals and induced acoustic signals for imaging simultaneously, we expect to correlate these two images to improve resolution and contrast significantly. In this section, we propose a new image correlation method named Correlated Microwave-Acoustic Imaging (CMAI) by merging CMI and TAI to achieve higher contrast, resolution rather than any one of them. A UWB transmitter is also designed for the whole system implementation in the future work.

3.1.2 Theory

3.1.2.1 System Configuration

System Setup

System configuration is shown in Fig. 3.1, objective sample is modeled as a circle filled with heterogeneous healthy human tissue, where a tumor with different dielectric property is embedded [8]. Microwave antennas are placed around to

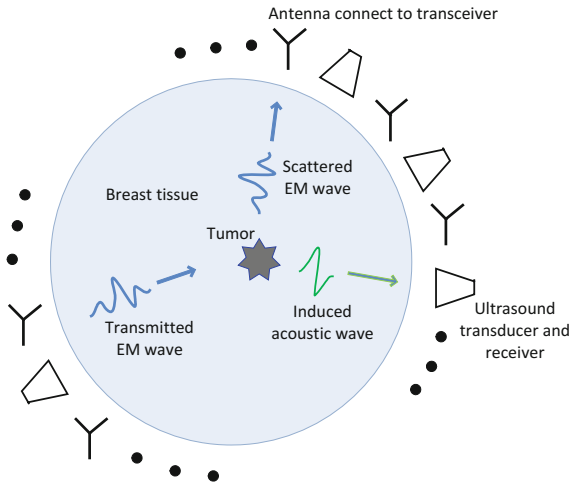

Fig. 3.1 System setup for merging CMI and TAI. *CMI* confocal microwave imaging; *TAI* thermoacoustic imaging

transmit UWB signals and receive scattered signals. Ultrasound transducers are also placed around for acoustic signals detection. This setup allows collecting both microwave and acoustic signals for image reconstruction.

Confocal Microwave Imaging

By solving the Maxwell's equations in heterogeneous medium, the scattered electric field *Escat* could be derived as [9]:

$$Escat = \omega^2 \mu (1 + \frac{\nabla \nabla \cdot}{k_b^2}) \int_V E(r') g(r, r') [\varepsilon^*(r') - \varepsilon_b^*] dV' \tag{3.1}$$

where ω and μ are the angular frequency and permeability of the medium, $\varepsilon^*(\mathrm{r}')$ and ε_b^* are the permittivity of tumor and surrounding normal tissue, $\mathrm{k_b} = \omega\sqrt{\mu\varepsilon_\mathrm{b}^*}$ and $\mathrm{g(r, r')} = \mathrm{e}^{-\mathrm{jk_b|r-r'|}}/4\pi|\mathrm{r} - \mathrm{r}'|$ is the Green's function. From above equation we see that strong scattering occurs at the interface of permittivity mismatch. Instead of solving the inverse problem of the equation for dielectric distribution mapping, CMI is to directly process the scattered signals for tumor detection. Signal pre-processing is illustrated in Fig. 3.2, followed by conventional delay-and-sum algorithm for image reconstruction.

Microwave-induced Thermoacoustic Imaging

When EM wave is propagating in the lossy human tissue, energy absorption occurs leading to transient temperature rising and thermal expansion. Induced acoustic wave goes outwards to the surface of the body following the wave equation:

$$\nabla^2 p(r, t) - \frac{1}{c^2} \frac{\partial^2}{\partial t^2} p(r, t) = -\frac{\beta}{C_P} \frac{\partial}{\partial t} H(r', t') \tag{3.2}$$

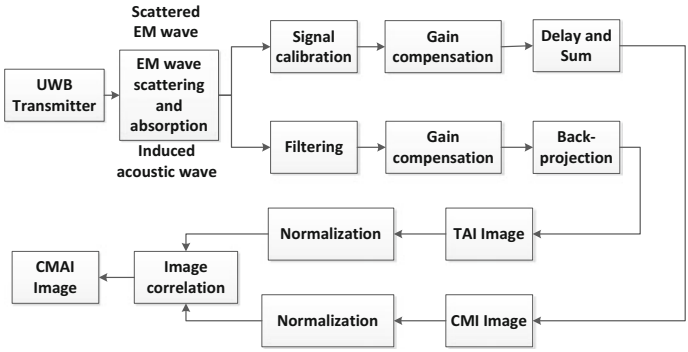

Fig. 3.2 Signal processing for CMI and TAI

where p(r, t) is the acoustic pressure signal, c is acoustic velocity in tissue, β is thermal expansion coefficient, C_p is the specific heat, $t' = (|r - r'|/c)$, and the heating function $H(r', t') = A(r')I(t')$, where A(r) is absorption distribution and I(t) is the temporal illumination function. Solving this equation gives:

$$p(r,t) = \frac{\beta}{4\pi C_p} \int\int\int \frac{d^3 r'}{|r - r'|} A(r') \frac{dI(t')}{dt'} \tag{3.3}$$

It is easy to see that the induced acoustic signal is proportional to the absorption distribution. Modified backprojection method is used for image reconstruction, revealing the absorption property of human tissue for tumor detection. Signal flow is shown in Fig. 3.2.

3.1.2.2 Proposed CMAI Method

According to the analysis before, both CMI and TAI are showing the dielectric properties of human tissue, i.e., the relative permittivity and conductivity. Thus we expect that combining of this two methods in some way will result in better performance. A correlated microwave-acoustic imaging (CMAI) method is proposed to strengthen the tumor detection and suppress the clutters in both images, shown in Fig. 3.2. Numerical simulation in part V shows significant performance improvement.

Although the imaging basis of both CMI and TAI are dielectric difference of tumor and healthy human tissue, they are acquired in totally different ways: scattered EM wave and induced acoustic wave. Due to the difference of their energy existence (EM wave and acoustic wave), they propagate in separated channels and suffer respective noise sources. Therefore, for the images of CMI and TAI, it is expected that they are correlated at the tumor location (strong scattering and absorption), and uncorrelated at other locations (different forms of noise source). In

addition, CMI has good contrast but poor resolution; while TAI can achieve good resolution and normal contrast. Hence, we proposed CMAI method to merge CMI and TAI together for both high resolution and high contrast.

CMI and TAI images are obtained using the simple algorithm mentioned above. Due to different reconstruction ways of CMI and TAI, scaling procedure should be applied for both images to have same scale range and then shift by their mean values, as illustrated in Eqs. (3.4) and (3.5). After scaling to the same range, CMI and TAI images are correlated as in Eq. (3.6):

$$CMI\ image: A(i,j) = \frac{A(i,j) - mean[A(i,j)]}{\max[A(i,j)]} \tag{3.4}$$

$$TAI\ image: B(i,j) = \frac{B(i,j) - mean[B(i,j)]}{\max[B(i,j)]} \tag{3.5}$$

$$CMAI\ image: C(i,j) = \frac{\sum_{m=i-1}^{i+1} \sum_{n=j-s}^{j+s} A(m,n)B(m,n)}{(2l+1)(2s+1)} \tag{3.6}$$

where the correlated image C(i, j) is obtained by multiplying the corresponding elements of CMI and TAI images in a rectangular area of size $(2l+1) \times (2s+1)$, adding together, and then averaging. By this way, at the tumor location, the elements of A and B are highly correlated, where multiplication and summation leads to significantly amplification and sharpening of the tumor. While for other locations, due to different noise sources and clutters, the elements of A and B are uncorrelated, i.e., both positive and negative values exist, their multiplication and then summation tend to be zero. Therefore, through this kind of image correlation, the tumor is supposed to be enhanced and clutters to be suppressed effectively

3.1.3 Results

3.1.3.1 UWB Transmitter Design

An on-off LC oscillator based pulse generator with high peak power and efficiency is shown in Fig. 3.3, which is designed and tested based on the previous work [10]. It includes a digital pulse generator, a LC VCO and a driver amplifier. On-Off Keying (OOK) with RZ input data is adopted to simplify the circuit. From simulation, the pulse generator is capable of generating nano-second pulse according to the rising edge of the RZ input data, and the total setup time can be controlled to be within 255 ps.

The transmitter chip is realized in Chartered's 0.18 μm process and occupies an area of 0.8 mm × 0.6 mm (core circuit). With 1 Mbps baseband input data, the circuit can generates a pulse with 2 GHz bandwidth (−20 dB). Figure 3.4 shows

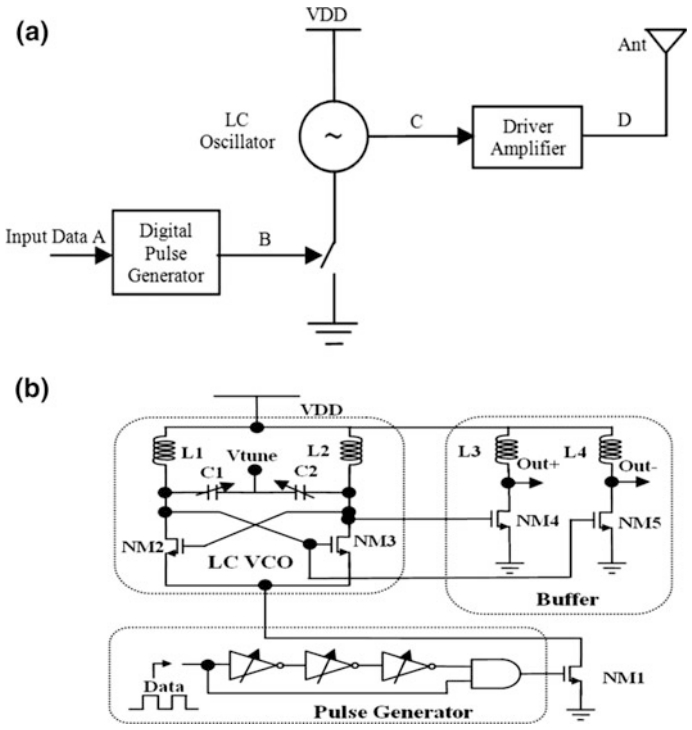

Fig. 3.3 **a** UWB transmitter architecture, **b** circuit schematic

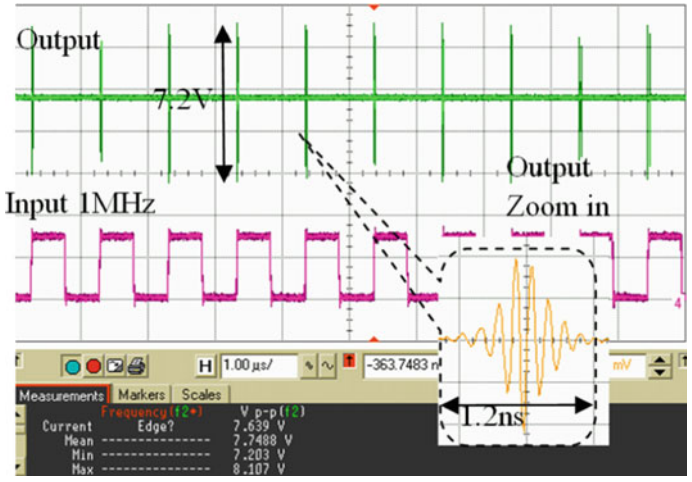

Fig. 3.4 Measured time-domain UWB pulse

the output pulse with 1.2 ns width and peak swing of 7.2 V, which is high enough for future imaging prototyping, and within the maximum permissible exposure (MPE) of radio frequency EM fields (3 kHz–300 GHz).

3.1.3.2 Numerical Simulation

Finite-difference time-domain (FDTD) method is used for the simulation of EM wave scattering and acoustic wave propagation. A simulated UWB signal, representing similar waveform with measured transmitter's output signal, is transmitted into human tissue model. Scattered microwave and induced acoustic wave shown in Fig. 3.5a, b are collected by microwave receivers and ultrasound transducers placed around objective sample at the same time.

The field of imaging is modeled as a 2D planar region (141 × 201) with 0.4 mm resolution, modeling healthy human tissue. Tumor is embedded as a circle with

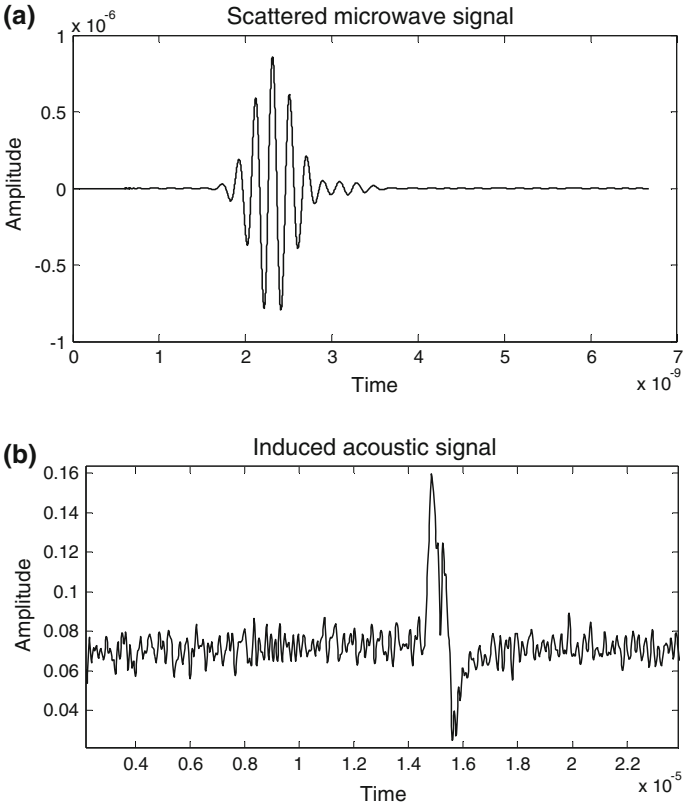

Fig. 3.5 Waveform of **a** scattered microwave signal and **b** induced acoustic signal. Reprinted from Ref. [11] with permission from Institute of Electrical and Electronics Engineers

Table 3.1 Dielectric properties of 6 cases

Table head	Dielectric properties					
	Low contrast scenario			High variation scenario		
ε_r/ϵ_b	2.0	1.7	1.4	2.0		
ε_b variation	3%			3%	6%	9%

1.6 mm radius. We set two scenarios of low contrast and large variation to test the performance of our proposed correlation method. Dielectric parameters are specified in Table 3.1.

In Table 3.1, three cases for low contrast scenarios and three cases for large variations scenarios are simulated, where $\varepsilon_r/\varepsilon_b$ specifies the dielectric contrast ratio of tumor and surrounding healthy tissue, and ε_b variation is modeling the heterogeneous properties of human tissue. Signal to clutter ratio (*S/C*) for these 6 cases are shown in Fig. 3.6. The *S/C* is deteriorating when dielectric contrast is decreasing and dielectric variation is increasing. In either case, the CMAI outperforms the CMI and the TAI with 2.5 and 0.5 dB improvement respectively.

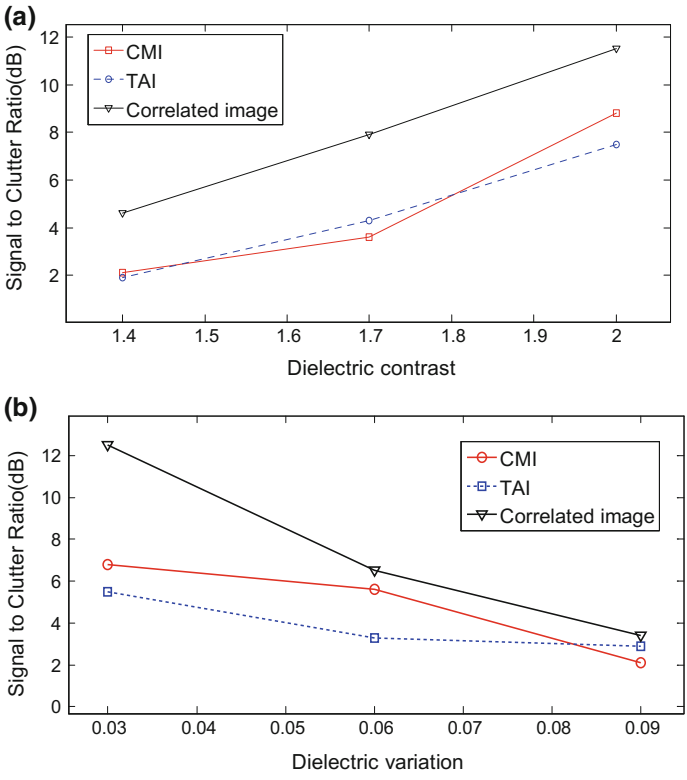

Fig. 3.6 Signal to clutter ratio is decreasing with **a** lower contrast and **b** larger variation. Reprinted from Ref. [11] with permission from Institute of Electrical and Electronics Engineers

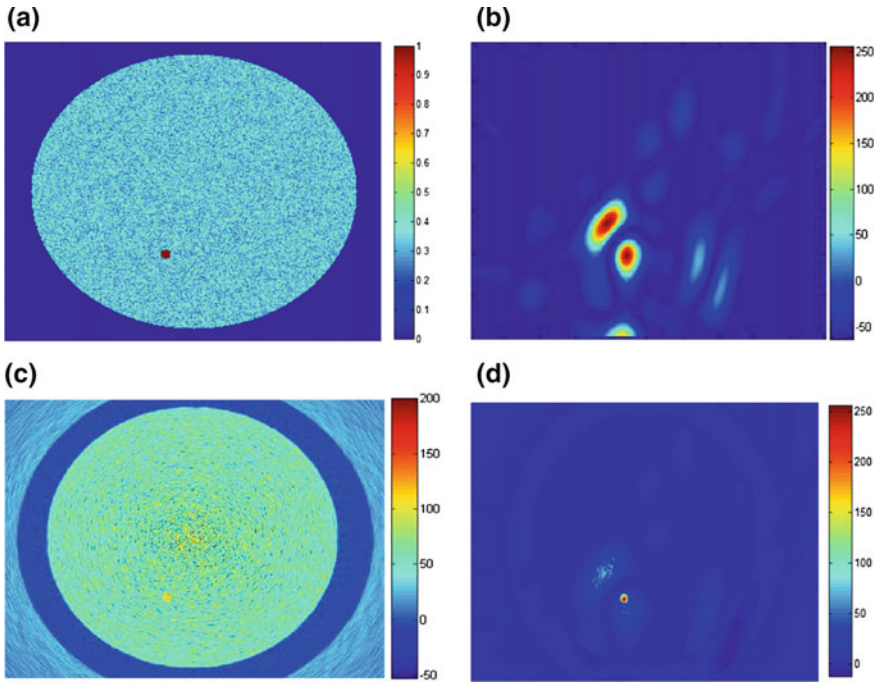

Fig. 3.7 **a** Dielectric distribution, and reconstructed images by **b** confocal microwave imaging, **c** microwave-induced thermoacoustic imaging and **d** proposed correlated imaging. Reprinted from Ref. [11] with permission from Institute of Electrical and Electronics Engineers

An extreme case by giving contrast as low as 1.4:1 and variation as large as 9% is tested using the three approaches. Simulation result is shown in Fig. 3.7, it is seen that for only CMI or TAI reconstructed image, the tumor cannot be identified clearly due to strong clutter in Fig. 3.7b, which is the result of multiple scattering of microwave in human tissue, and noise caused by heterogeneous tissue heating in Fig. 3.7c. However, by the proposed CMAI method (Fig. 3.7d), the tumor is detected clearly by strengthening the correlated tumor part and suppressing other uncorrelated clutter parts.

3.1.4 Conclusion

In this section, we propose a new imaging correlation approach CMAI to merge CMI and TAI. Avoiding complicated reconstruction algorithms of CMI and TAI proposed before, we apply simple reconstruction algorithm and the proposed CMAI method obtains much better performance in terms of resolution, contrast and speed. A UWB transmitter is designed specifically for the UWB signal generation with

high peak voltage and efficiency, which will be embedded in the whole imaging system for experimental verification in our future work. For the realistic application of the correlated microwave-acoustic imaging, a high-peak power microwave source is needed, and a rough estimation of the peak power should be around several kW for a single pulse. Meanwhile, the average power during the operation should be kept low around several mW to ensure EM exposure safety. Considering its high potential of integrated circuit integration, we expect to develop the CMAI into a portable microwave-based imaging device for early-stage cancer monitoring.

3.2 Single-Wavelength Blood Oxygen Saturation Detection

In this section, a novel approach using single laser wavelength based on the combined optical absorption induced photoacoustic and optical scattering method, is developed to noninvasively measure blood oxygen saturation (SO_2), the concentration of deoxygenated haemoglobin (HbR) and oxygenated hemoglobin (HbO_2) on dual-ink phantoms. Here, using mixed green-red ink phantom, the concentration of ink and pseudo-SO_2 were quantified with less than 6.97% error experimentally. Then the pseudo-SO_2 was imaged in the single tube cross-section. Unlike conventional multi-wavelength photoacoustic or near infrared spectroscopy approaches, the proposed single-wavelength method would significantly lower the laser system cost and enable potential portable implementations. The results of this section have been published in *IEEE Sensors Journal* [12].

3.2.1 Introduction

Blood oxygen saturation (SO_2) is defined as the ratio of the concentrations between oxyhemoglobin (HbO_2) and total hemoglobin ($HbR + HbO_2$), which is a very important physiological parameter in the medical and clinical fields. Blood oxygen saturation can show the oxygenation of the lungs, blood transport and tissue oxygen consumption. It could provide a potential method for diagnosis and detection of brain, tumor hemodynamics, gene expression, and other pathophysiological phenomena. Pulse oximetry is a widely used and non-invasive method to monitor the blood oxygen saturation. It is based on the light absorbing variations of the arterial blood following the heart beat, while the absorption of the skin, muscle, bones and venous blood remain constant. The spectrophotometric method is used to calculate the arterial blood oxygen saturation using multi-wavelength light source. However, this method has poor spatial resolution and suffers body movement. On the other

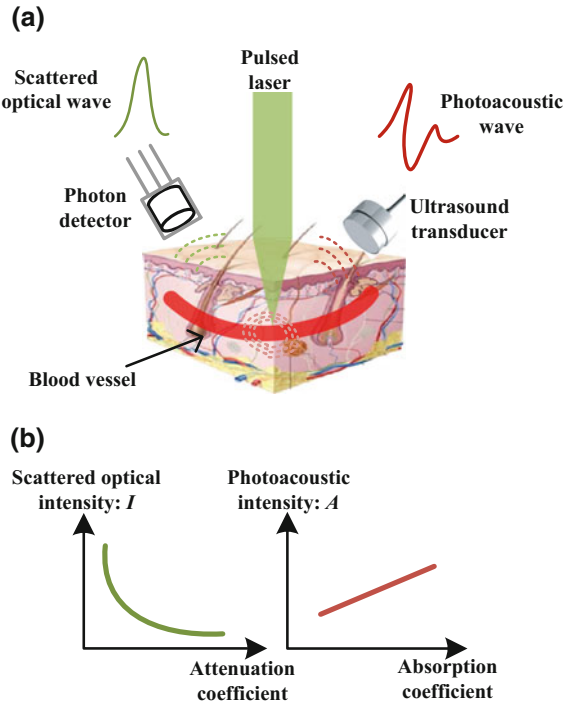

Fig. 3.8 **a** Cross-sectional schematic of single wavelength SO_2 detection with ultrasound transducer and photon detectors. **b** The plots of scattered optical intensity and photoacoustic intensity along with attenuation/absorption coefficients

hand, the photoacoustic (PA) effect is the mechanism referring to the generation of sound wave through the absorption of light and conversion to heat. Because the PA signal is proportional to the optical absorption and the local optical fluency, the photoacoustic microscopy (PAM) is able to calculate the blood oxygen saturation using multi-wavelength light source. The PAM has high spatial resolution, but multi-wavelength PA measurement typically requires an expensive and bulky tunable high-power laser, which is undesirable in non-laboratory environment. Moreover, the spectral dependence of the local optical fluence, and hence the PA signal, combined with the unknown spectral properties of the surrounding tissues, present challenges to accurate SO_2 measurements. A very recent study reports a single wavelength PA method based on the saturation of the optical absorption, but it may bring damage to organism due to the significantly high laser intensity. In our study, both the optical absorption induced photoacoustic signal and diffusively scattered optical signal after the attenuation of the light through tissues are collected to establish the equations as shown in Fig. 3.8a. Based on the PA signal equation and scattered optical equation, we can measure the SO_2 and the concentrations of the HbO_2 and HbR using single wavelength within the laser safety range.

3.2.2 Theory

During laser-induced photoacoustic process, the acoustic signal is launched based on the principle of thermal expansion following the optical energy absorption by the sample. Here the blood vessel is the targeted object, we can get the photoacoustic signal.

$$A(\lambda) = H\alpha\Gamma(\varepsilon_{HbR}[HbR] + \varepsilon_{HbO_2}[HbO_2])F \tag{3.7}$$

where H is the system transfer function, α is a coefficient related to the ultrasonic parameters, Γ is the Gruneisen parameter, and F is the local optical fluence (J/cm^2). The local optical fluence can also be expressed as the multiplication of the local laser intensity and the laser pulse width. H, α, Γ and F are all constant due to the fixed system setup and experimental environment, so A and the absorbing factor present the liner relationship as shown in Fig. 3.8b. The ε_{HbR} and ε_{HbO_2} are the known molar extinction coefficients of HbR and HbO_2, respectively, and also constant. Only $[HbR]$ and $[HbO_2]$ are the unknown concentrations of HbR and HbO_2. We need two equations to resolve $[HbR]$ and $[HbO_2]$. Here we can set up the first equation about PA:

$$A = \text{constant1} * [HbR] \ + \ \text{constant2} * [HbO_2] \tag{3.8}$$

On the other hand, when a beam of light irradiates on the surface of the sample, the light intensity will be attenuated, which follows the Beer-Lambert law. The Beer-lambert law relates the attenuation of light to both the optical absorption and scattering properties of the sample. The power of the residual light intensity is derived by the expression:

$$I = I_0 e^{-\mu l C} \tag{3.9}$$

The attenuation coefficient of the light μ is related with the summation of the absorption coefficient and the scattering coefficient. L is the light route, and C is the molar concentration.

According to the property of the multilayer biological tissues, light goes through each layer and experiences exponential attenuation as shown in Fig. 3.8b. Then we can get the power of the detected light from the photon detector as shown in Fig. 3.8:

$$I = I_0 e^{-\mu_1 l_1 C_1} e^{-\mu_2 l_2 C_2} e^{-\mu_3 l_3 C_3} \ldots \tag{3.10}$$

The absorption and scattering of the light through the multilayer biological tissues can be seen as constant. Then we can derive the second optical equation as below:

$$\begin{aligned} \lg(I) &= \text{constant} - \mu lC = \text{constant} - (\mu_{HbR}[HbR] + \mu_{HbO_2}[HbO_2]l \\ &= \text{constant3} - (\text{constant4} * [HbR] + \text{constant5} * [HbO_2]) \end{aligned} \tag{3.11}$$

In this equation there are three parameters (constant3, constant4 and constant5) and two variables ($[HbR]$ and $[HbO_2]$). By solving the two linear equations Eqs. (3.8) and (3.11) with two variables, the $[HbT]$ and SO_2 can be calculated using single-wavelength laser illumination.

3.2.3 Experimental Results

The experimental setup is shown in Fig. 3.9, where the optical absorption induced photoacoustic signal is captured by the ultrasound transducer (1 MHz, V303-SU, Olympus), and the residual light signal after attenuation (absorption + scattering) is captured by the photon detector (DET10A, Thorlabs). In the phantom experiment, two ink samples (green and red, Private Reserve Ink) were mixed in various concentration ratios to mimic different levels of SO_2 as pseudo-SO_2. By controlling the total concentration, the mixed samples have comparable optical absorption coefficients to that of blood. The laser has 532 nm wavelength and 2 ns pulse width. During data collection, the mixed solution was injected into a silicone transparent tube with an inner diameter of 3 mm. The ratio of the red ink concentration in the total ink concentration ($[red]/([red] + [green])$) is used to mimic the SO_2, and $[red]$

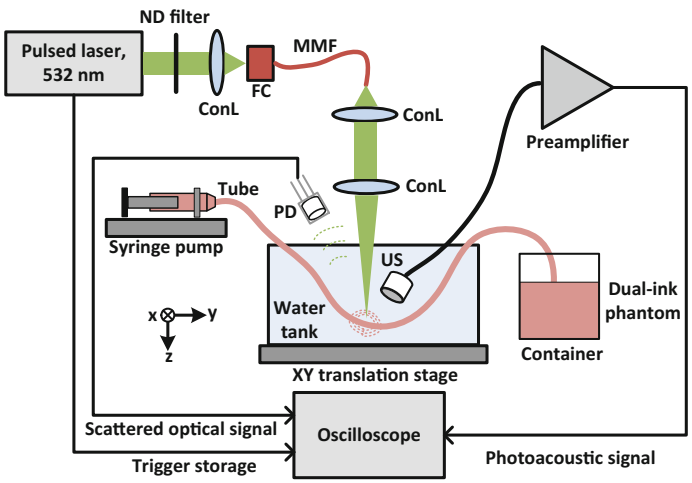

Fig. 3.9 The system architecture with the single wavelength laser source, which is able to collect both PA and optical signals simultaneously. *ConL* condenser lens; *FC* fiber coupler; *MMF* multi-mode fiber; *ND* neutral density; *PD* photon detector; *US* ultrasound transducer. Reprinted from Ref. [12] with permission from Institute of Electrical and Electronics Engineers

Table 3.2 The result of the curve fitting

Constant1	Constant2	SSE	R-square	Adjusted R-square	RMSE
0.05796	0.1006	0.006322	0.9452	0.9373	0.03005

Table 3.3 The result of the curve fitting

Constant3	Constant4	Constant5	SSE	R-square	Adjusted R-square	RMSE
1.097	0.08532	0.09143	7.852e-05	0.966	0.9547	0.003618

and $[green]$ are used to mimic $[HbO_2]$ and $[HbR]$, respectively. So $[HbT]$ is the summation of $[red]$ and $[green]$.

In order to extract $[HbR]$, $[HbO_2]$, $[Hbt]$ and SO_2 using single wavelength, here we use the dual-ink phantom for experiments. Two kinds of dyes made from red and green inks were employed to mimic HbO_2 and HbR, respectively. The original green and red inks were diluted with water in nine ratios range from 9:1 to 1:9. The parameters in two Eqs. (3.8) and (3.11) are obtained using the curve fitting tool in MATLAB to fit the experiment data. The results from the curve fitting tool are showed in Tables 3.2 and 3.3. The statistics results show that the fitting equation matches the data in experiments very well.

In the first experiment, the validity of this method is to be proved by measuring the concentrations and SO_2 using single wavelength light source. Mixed dye solutions with different ratios between [green] and [red] were measured, where the ratio of the concentration of the green ink in the mixer changed from 9:1 to 1:9 with a constant interval of 1, and the ratio of the red ink is versus as the green ink. Figure 3.10a–c present the measured ratio of the concentrations of the green and red ink and total ratio at the preset ratio of the green and red ink and the total concentration ratio. The Y-axis shows the measured ratios and the total dye concentration ratio. These results match well with the preset concentrations on the X-axis seen from Fig. 3.10. The change of the pseudo-SO_2 was calculated from 10 to 90% with a constant interval of 10% from the preset concentration. The measurements results in Fig. 3.10d also match well with the root mean square error less than 6.97%. The experiment results on the phantom samples proved the capability of the proposed single wavelength PA approach to measure the concentrations and pseudo-SO_2 of the dual-ink phantom based on their distinct absorption and scattering characteristics.

To demonstrate the capability of imaging SO_2 using this system, the experiments were performed using the dual-ink phantom. The experimental setup is almost same except employing translation stage to move the sample. The cross-section of the tube filled with the dual-ink phantom is linearly scanned along X axis. Different pesue-SO_2 images at different ratios were showed in Fig. 3.11, obtaining a good agreement with the preset values.

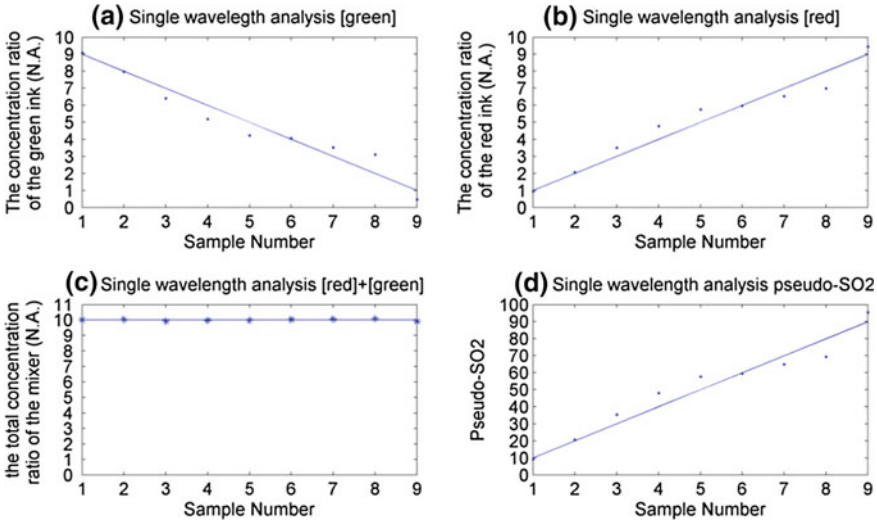

Fig. 3.10 Single wavelength analysis results **a** the concentration ratio of the green ink, **b** the red ink, **c** the mixer ink, and **d** the pseudo-SO_2

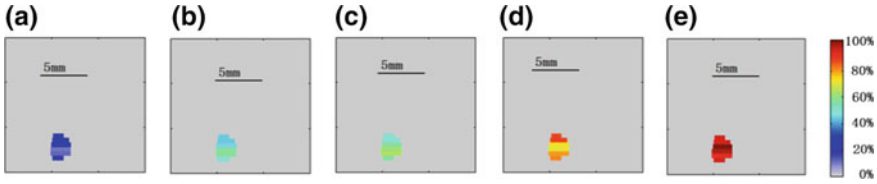

Fig. 3.11 Pseudo-SO_2 images of dual-ink phantom: **a** 20%, **b** 40%, **c** 60%, **d** 80%, **e** 100%

3.2.4 Discussion and Conclusion

To improve the precision of measurement, we find that the location of the photon detector is very crucial to measurement sensitivity. The transmission and reflection modes of the photon detection method are all used and compared in this experiment. The transmission mode has higher sensitivity than the reflection mode, the error may be induced by the different scattering light route of transmission and reflection modes. However, the reflection mode is a more flexible measurement setup and will be optimized in the future work.

In conclusion, a novel approach combining optical absorption and scattering for single wavelength SO_2 detection is proposed and proved experimentally. Compared with conventional multi-wavelength PA and NIR SO_2 detection, our system uses a single laser wavelength to extract the relative concentrations of mixed dual-ink phantom with different absorption and scattering characteristics. This proposed

single wavelength approach may be highly integrated, inexpensive, and much simpler than multi-wavelength approaches, showing significant potential for on-site diagnostics.

3.3 Photoacoustic-Guided Depth-Resolved Raman Spectroscopy for Skin Cancer Detection

Raman spectroscopy is a significantly sensitive tool for material, gas, chemical, pharmaceutical and biological tissue characterization and imaging [13–15]. However, due to the strong diffusion of light inside optically scattering medium, the current Raman spectroscopy is limited to superficial applications within one mean free pass of photon (<1 mm), which cannot resolve depth/spatial information. To overcome the limitations of traditional Raman spectroscopy, we propose a novel PA-guided spatial-resolved Raman spectroscopy to iteratively guide light focusing on the target inside heterogeneous medium by PA depth estimation. The results of this section have been published in *Optics Letters* [16].

3.3.1 Theory

Theoretically from microscopic perspective, Raman scattering is a kind of photon-phonon interactions as shown in Fig. 3.12a, where energy conservation remains related with frequencies:

$$\hbar\omega_P = \hbar\omega_{OP} + \hbar\omega_S \tag{3.12}$$

where ħ is the Planck constant, $\omega_P, \omega_{OP}, \omega_S$ are the frequencies of the pumped light, optical phonon in THz range (electron vibrational mode transfer in Fig. 3.12b) and the Raman scattering photon respectively [17]. The intensity of Raman scattering is determined by the Raman gain:

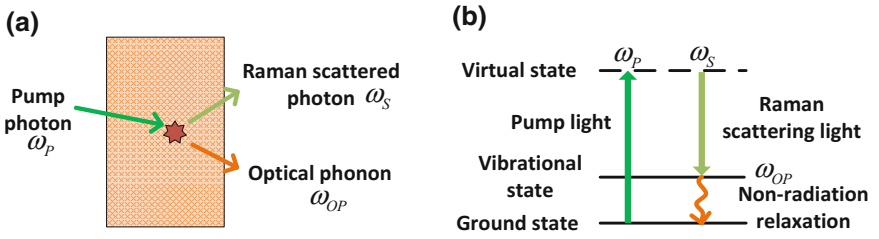

Fig. 3.12 **a** Photon-phonon interaction of Raman scattering; **b** Electron state transition schematic

$$g = \frac{8\pi^2 Nc^2}{\hbar\omega_S^3 \Gamma}\frac{d\sigma}{d\Omega}.I_p \tag{3.13}$$

where N is the density of molecules in the selected object, $d\sigma/d\Omega$ is the differential Raman cross-section for the excited transition, Γ is the line-width of this transition, c is the light speed. On the other hand, the intensity of PA wave is governed by:

$$p = \frac{v_s^2 \beta}{C_p}\mu_a I_p \tag{3.14}$$

where v_s^2 is the acoustic velocity, β is the thermal expansion coefficient, C_p is the specific heat, and μ_a is the optical absorption coefficient. From Eqs. (3.13) and (3.14) we can conclude that both Raman scattering and PA effect are highly correlated and could be enhanced by increasing the pump energy density I_p, equivalently by increasing the optical focusing. Therefore we propose to use PA wave to guide the optical focusing iteratively to achieve maximized responses for both PA signal and Raman scattering. The detailed methodology is shown in Fig. 3.13, and the proposed iterative imaging includes:

1. Use unfocused light to illuminate the sample. The PA signal p_1 is detected by the acoustic transducers, from which the depth d_1 is estimated. The Raman spectrum $R_{a1}(\omega)$ is obtained through a Raman detector (Fig. 3.13a);
2. Use focused light illumination from another angle with focal length d_1 to obtain PA signal p_2. From p_2, a more accurate estimation of depth d_2 can be obtained. Record Raman spectrum $R_{a2}(\omega)$ (Fig. 3.13b);
3. Use focused light illumination from another different angle with focal length d_2 to obtain PA signal p_3. From p_3, a further refined estimation of depth d_3 can be obtained. Record Raman spectrum $R_{a3}(\omega)$ (Fig. 3.13c);
4. Repeat the iterations in steps 2 and 3 until the estimation of depth is unchanged, then both the PA signal and Raman spectrum (related to the corresponding background noise) at the selected depth are statistically maximized.

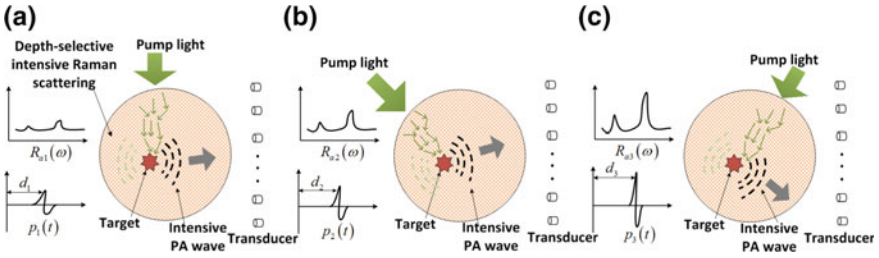

Fig. 3.13 PA-guided depth (spatial)-resolved Raman spectroscopy by illuminating the object from different angles

For each iteration, the PA signal will give a more accurate estimation of depth information than last step to guide the optical focusing for Raman spectroscopy from a more specific location in depth, as shown in Fig. 3.13.

3.3.2 Preliminary Results

3.3.2.1 Phantom Preparation

A highly purified agarose powder (Vivantis, California, USA) was added into distilled water at a concentration of 1% w/w. The mixture was brought to a boil using a microwave oven until the agarose powder melted and dissolved completely. Then, the agar solution was poured into a mould and left for cooling in the room temperature until it was set. A three-layered agar phantom was prepared with trans-Stilbene powder (Sigma-Aldrich, Missouri, USA) being added in between the two agar layers with a dimension of 1 mm × 1 mm × 1 mm. The thickness of the top layer was 1 mm and the thickness of bottom layer was 10 mm whereas the lateral dimension of both layers was made greater than 10 mm in diameter to represent a semi-infinite medium, see Fig. 3.14. A tiny drop of Nigrosin solution, at a concentration of 10 mg/ml, was added to the trans-Stilbene powder layer to enhance the photo-acoustic signal contrast of the middle layer from the top and bottom layers. A piece of plastic wrap was placed between the each layer to prevent the diffusion of Nigrosin into the top and bottom layers.

3.3.2.2 Experimental Setup

The detailed setup of the PA + Raman experiment is illustrated in Fig. 3.15. The PA system and Raman system share the same optical focusing lens with both excitation lasers focused at the same focal point. This ensures that the collected PA signal and Raman signal are emitted from the same location of the sample, and makes it possible to use the real-time PA signal to guide the Raman signal. The

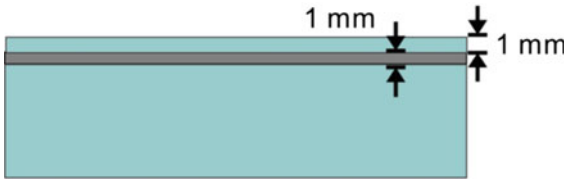

Fig. 3.14 Illustration of the three-layer tissue-mimicking phantom. The first layer and third layer are made of agar model the human skin, and the middle layer is to model the object (e.g. tumor cells) with strong Raman scattering and optical absorption, using mixed trans-Stilbene powder (Sigma-Aldrich, Missouri, USA and Nigrosin solution)

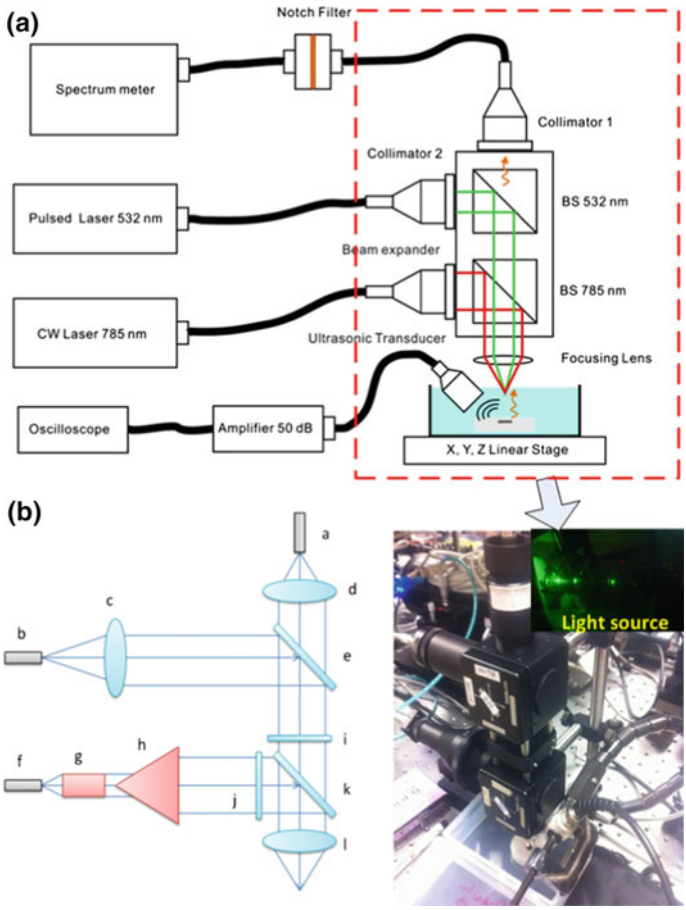

Fig. 3.15 Experimental setup of the PA + Raman system. **a** Overview of the system. **b** Detailed optical setup of the system. Where *a* collection fiber, multimode, 400 um, *NA* 0.22; *b* 532 nm excitation fiber; *c* convex lens, *FL* 35 mm; *d* convex lens, *FL* 35 mm; *e* beam splitter, 50R/50T; *f* excitation fiber, multimode, 100 um, 0.22 NA; *g* 785 nm collimator; *h* beam expander; *i* longpass filter (Semrock, Part Number: LP02-785RU-25); *j* 785 nm bandpass filter (Semrock, Part Number: LD01-785/10-25); *k* 785 nm dichroic mirror (Semrock, Part Number: LPD01-785RS-25); *l* convex lens, *FL* 35 mm

whole system was mounted on a XYZ translation stage, which has a 25 mm translation range in each axis with engraved graduations every 10 µm.

Detail of PA system

The excitation source for PA was a Q-switched, 1064 nm, DPSS laser (1Q 532-2, Crylas), frequency doubled to 532 nm with pulse duration of 1.8 ns and a maximum repetition rate of 10 kHz. The output of the laser was coupled to a multimode with a diameter of 100 um and a numerical aperture of 0.22. Photoacoustic signal is

collected by a wideband ultrasound transducer with 2.25 MHz central frequency (V323-SU, Olympus), followed by an ultrasound preamplifier (Model 5662, Olympus). A digital oscilloscope is used to record the photoacoustic signal at 500 MHz sampling rate.

Detail of Raman system

Fiber 'f' was connected to an infrared diode laser module (FC-D-785, CNI Optoelectronics Tech. Co. Ltd., Changchun, P.R. China) with a maximum output power of 500 mW at 785 nm. The Raman signals collected by fiber 'a' will be coupled to a 303 mm focal length, motorized, Czerny-Turner spectrograph (Shamrock 303, Andor Technology, Belfast, UK) equipped with a 1200 line/mm grating (SR3-GRT-1200-1000, Andor Technology, Belfast, UK) and a research-grade CCD (DU920P-BR-DD, Andor Technology, Belfast, UK), which yields a spectral resolution of 0.07 nm. The acquisition time for each Raman spectrum was 5 s. The power of 785 nm laser measured on sample surface was 75 mW.

Measurement procedures

1. PA measurement was performed first to find the depth information (location) of the tumour. The PA signal p_1 is detected by the acoustic transducer, and based on the acoustic traveling time, the depth information of the tumour d_1 is found. The Raman signal is R_1 is measured as well.
2. Based on the first estimation, the z position of the XYZ stage is adjusted to achieve a better focusing d_2, and the corresponding Raman signal is R_2 is measured.
3. To verify the concept of PA-guided depth-resolved Raman spectroscopy, the PA signal and Raman signal at different focusing planes were recorded simultaneously by scanning along Z direction using the XYZ translational stage.

3.3.2.3 Experimental Results

The preliminary experiment on the PA-guided depth-resolved Raman spectroscopy has been conducted to prove its feasibility using a three-layer tissue-mimicking phantom. Figures 3.16 and 3.17 shows clearly that due to the guidance of PA signals, the Raman spectrum is enhanced step by step to reach the maximum response. In the meantime, the PA signals are achieving larger magnitude and narrower pulse width, which could give more accurate depth information to localize Raman spectroscopy. A detailed verification of the PA-guided depth-resolved Raman spectroscopy method is shown in Fig. 3.17. In the figure, the x axis indicates the relative position of the focusing point with respective to the location of the tumour layer. x is negative when the focusing point is located above the tumour layer, while it is positive when the focusing point is located below the tumour layer. When the focusing point is precisely located at the tumour layer, the relative

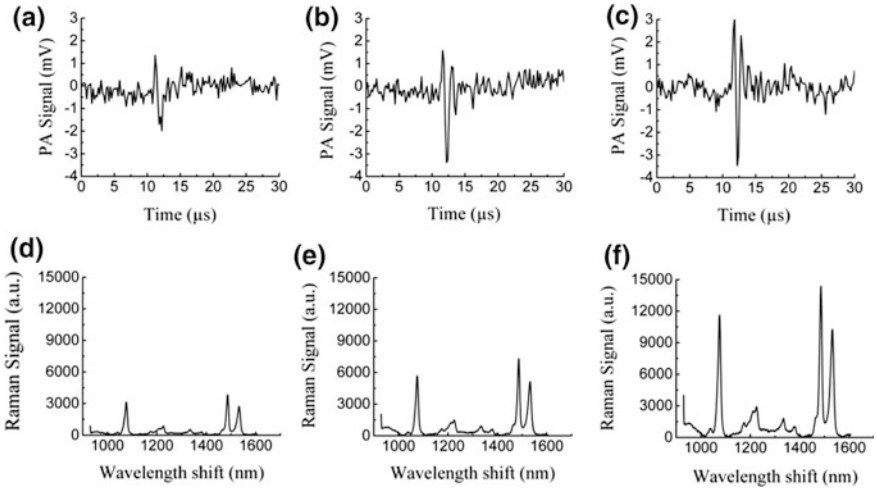

Fig. 3.16 **a**–**c** Photoacoustic signals of three steps to guide the optical focusing; focusing point of the lens is **a** 10 mm; **b** 4 mm, **c** 0 mm above the tumour. **d**–**f** PA-guided Raman spectrums to reach the maximized response; focusing point of the lens is **a** 10 mm; **b** 4 mm, **c** 0 mm above the tumour

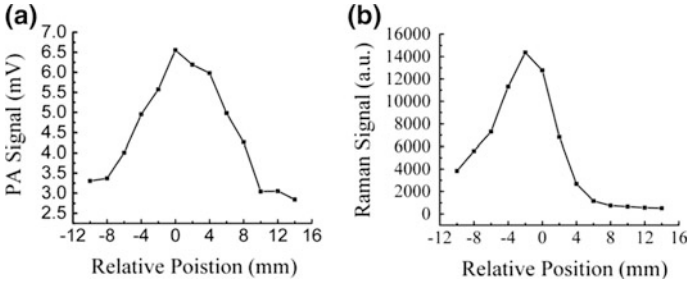

Fig. 3.17 **a** Strength of the PA signal recorded at different depth. **b** Strength of the Raman signal recorded at different depth

position is 0. From the figure, it can be seen that the PA and Raman signal are positively correlated. Both of them have the maximum signal strength when the focusing point is precisely located at the tumour layer.

3.3.2.4 Experimental Results Using Single Laser Source

In this setup, we use only single pulsed laser source (532 nm, 1 mJ) to excite the Raman scattering signal and photoacoustic signal simultaneously. The first layer made of intralipid (μ_s = 42.4 cm^{-1}) is to model the human skin, and the second layer is to model the object (e.g. tumor cells) with strong Raman scattering and

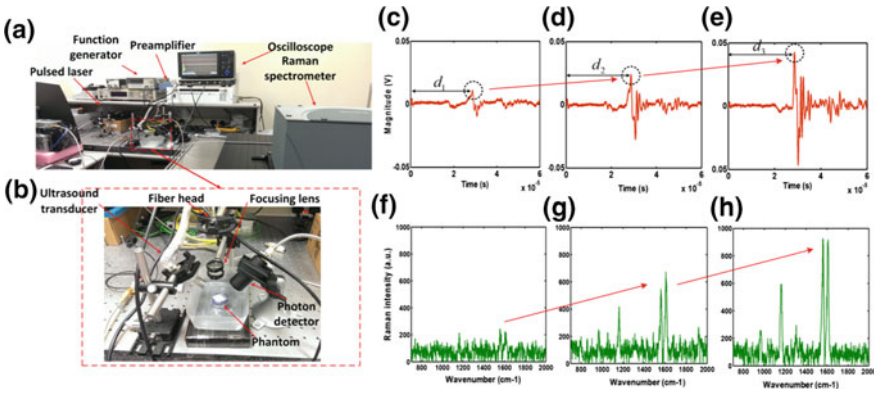

Fig. 3.18 **a**, **b** Photograph of the experiment setup; **c**–**e** Photoacoustic signals of three steps to guide the optical focusing; **f**–**h** PA-guided Raman spectrums to reach the maximized response

optical absorption, using mixed intralipid, t-stilbene powder and blue ink. The photograph of the experiment setup is shown in Fig. 3.18a, b where the sample is illuminated by a pulsed laser, both Raman scattered photons and PA wave are acquired by a Raman spectrometer and oscilloscope respectively. Figure 3.18c, h shows clearly that due to the guidance of PA signals, the Raman spectrum is enhanced step by step to reach the maximum response by the proposed approach. In the meantime, the PA signals are achieving larger magnitude and narrower pulse width, which could give more accurate depth information to localize Raman spectroscopy.

3.3.3 Discussion and Conclusion

Our preliminary result has proven the feasibility of the PA-guided Raman spectroscopy on a phantom study. By nature, 2D PA depth-resolved Raman spectroscopy can be extended to 3D spatial resolved Raman spectroscopy through 3D tomography system. Based on this, the optical time-reversal focusing always can be applied to further improve the sensitivity and resolution of the 3D Raman spectroscopy. An extension to PA-guided 3D spatial resolved fluorescence spectroscopy is also possible using the same method. In brief, based on the proposed novel PA-guided depth/spatial-resolved Raman spectroscopy approach, spatial information of molecular chemical compositions and conformations could be revealed for many promising applications, such as non-invasive epithelial cancer early diagnosis, non-destructive material characterization and industrial chemistry, etc.

3.4 Multistatic Photoacoustic Classification of Tumor Malignancy

Accurate tumor classification to discriminate between malignant and benign tumors is important to achieve high specificity diagnosis, timely cancer treatment and avoid unnecessary biopsy. Photoacoustic tomography (PAT) is an emerging imaging modality, combining optical contrast, ultrasound resolution with deep penetration. However, the capability of PAT to differentiate malignant and benign tumors has not been fully explored, which may be limited due to similar optical absorption of malignant/benign tumors and severe acoustic attenuation in deep tissue. In this section, we report a multistatic photoacoustic based classification approach to distinguish malignant/benign tumors based on their different shape irregularity, which is a well-known feature in clinical diagnosis. In numerical simulation study, we consider three types of tumors with different irregularity to represent malignant, suspicious and benign tumors. Two features are extracted from the multistatic photoacoustic signals in four different scenarios to classify the three types of tumor with high accuracy. On the other hand, state-of-art time-reversal based PAT image reconstruction is also performed to reconstruct the images, which cannot differentiate their malignancy clearly due to strong acoustic distortion. The proposed multistatic photoacoustic classification shows promising results to differentiate malignant/benign tumors, and could be readily integrated with state-of-art PAT system to improve the diagnosis specificity.

3.4.1 Introduction

In cancer diagnostics, the high specificity of medical imaging modalities is strongly preferred to differentiate between malignant and benign tumors. It will improve the cancer treatment strategy, avoid the unnecessary biopsy and increase the survival rate of patient. Clinically it is well known that the shape irregularity could aid in distinguishing malignant tumors from benign tumors. For example in mammography, round-shape with regular boundary tumor is associated with benign masses, while malignant tumors often exhibits irregular shape with ill-defined boundaries [18].

Photoacoustic (PA) imaging is attracting significant research interest in recent years due to its breaking through of optical diffusion limit by “listening to photons”, i.e. detecting optical absorption induced photoacoustic wave. PA microscopy (PAM) and tomography (PAT) have been well developed to achieve multi-scale multi-contrast imaging performance, probing endogenous chromophores (hemoglobin, melanin, etc.) or exogenous contrast agents. Although cancer (e.g. breast cancer) diagnostic by PAT is studied for several years [19], the capability of differentiating malignant and benign tumors by PAT has not been fully explored. Some preliminary studies showed the feasibility to characterize microstructure’s

size based on single ultrasound transducer detection and PA spectrum analysis [20]. However, shape irregularity characterization by PA technique is still an untapped area, which is potential to solve the malignant and benign tumor classification problem mentioned above, enabling the PA imaging to achieve higher specificity and reliability.

In this section, a multistatic photoacoustic classification approach is proposed by collecting PA waves from tumors with different shape irregularity by multiple ultrasound transducers, which is readily available for the state-of-art array-based PAT system. The feasibility of the proposed approach is studied in numerical simulation with four different scenarios, and further validated with experimental results using tumor-mimicking phantom.

3.4.2 Methods

3.4.2.1 Tumor Malignancy Model

To emulate the different malignancy levels of tumor, the shape irregularity needs to be well modelled. It was observed that polygonal approximation of the tumor boundaries could match the hand-drawn diseased tissue boundaries by the radiologist very well. Therefore, a similar elliptical model is utilized here to simulate the shape irregularity of tumor. The baseline ellipse in the polar coordinate is defined below:

$$B(\theta) = \frac{ab}{\sqrt{a^2 \sin^2\theta + b^2 \cos^2\theta}} \tag{3.15}$$

where a and b are the semi-major and semi-minor axes of the ellipse, and θ is the angle indicated in Fig. 3.19. To define different levels of shape irregularity, the elliptical profile is modified by applying the border deviation profile $\beta(\theta_i)$ to the baseline ellipse:

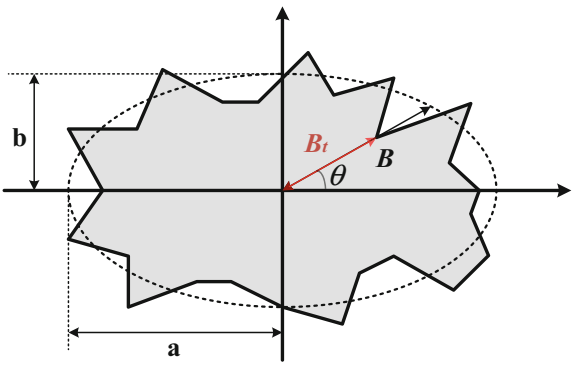

Fig. 3.19 The schematic of the tumor malignancy model

$$B_t(\theta_i) = B(\theta_i)(1 + \beta(\theta_i)), \quad i = 1, 2, \ldots 36 \tag{3.16}$$

where θ_i is one of the uniformly separated 36 angles with step size of 10°. The value of the border deviation profile $\beta(\theta_i) \in [-\Delta B, +\Delta B]$ determines the shape irregularity of the tumor profile $B_t(\theta)$. More specifically, a larger value of ΔB indicates a more irregular shape of the tumor model $B_t(\theta)$.

3.4.2.2 Photoacoustic Numerical Simulation

The photoacoustic wavefield could be simulated by the k-space pseudospectral method, which has been implemented in the MATLAB k-Wave toolbox and utilized in this study [21, 22]. A more detailed description of the k-space pseudospectral method can be found in [21].

Simulation geometry: The region of numerical simulation is shown in Fig. 3.20, which is based on uniform grid of 256 × 256 pixels with a pitch of 46 μm for the 2D simulation study. A perfectly matched layer (PML) with thickness of 20 grid points was employed surrounding the simulation region to avoid acoustic wave reflection at the boundary. The acoustic velocity is set to be 1500 m/s in soft tissue; and acoustic attenuation of the region is set to be 0.75 dB/(MHz cm) that is similar with breast tissue. In Fig. 3.20 of full field-of-view scenario (case 1), 20 acoustic sensors were placed evenly on a circle of radius 4.5 mm to receive the photoacoustic wave. For another 3 cases of limited field-of-view, only 10 sensors were placed evenly on a semi-circle of radius 4.5 mm.

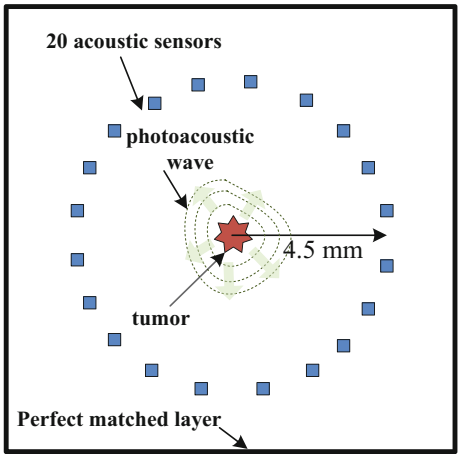

Fig. 3.20 Full field-of-view simulation geometry with 20 acoustic sensors

Table 3.4 Three types of tumor model with different malignancy levels

Malignancy level	ΔB
Malignant	0.4
Suspicious	0.2
Benign	0.1

Numerical phantom: Numerical phantoms of the tumor with different levels of malignancy were generated by incorporating the tumor malignancy model in previous section. The baseline size of the tumor was fixed to be 1 mm in diameter ($a = 0.5$ mm, $b = 0.5$ mm). In this study, three different levels of tumor malignancy was generated by selecting three values of ΔB, which was summarised in Table 3.4. Lastly the generated numerical tumor model is assigned to represent the initial pressure distribution in the 2-D photoacoustic simulation.

Data measurement: Point-like transducer was utilized to receive the pressure data generated from the numerical tumor phantom by use of the k-space pseudospectral method for both full and half point-of-view geometries. Random noise was introduced in the original photoacoustic signal to achieve 40 dB signal-to-noise ratio (SNR). A time-reversal (TR) image reconstruction algorithm was utilized to visualize the tumor for malignance diagnosis, which was compared with the proposed multistatic photoacoustic classification approach introduced in the next section.

3.4.2.3 Multistatic Photoacoustic Classification

As a proof-of-concept study, two simple features are extracted from the photoacoustic signals of the 20 sensors. The first feature F_1 is the accumulated signal amplitude variation, which is expressed as:

$$F_1 = \sum_{n=1}^{20} \max(peak(p_n)) - \min(peak(p_n)) \tag{3.17}$$

The second feature is the accumulated signal amplitude continuity expressed as:

$$F_2 = \sum_{n=3}^{20} (peak(p_n) - peak(p_{n-1})) - (peak(p_{n-1}) - peak(p_{n-2})) \tag{3.18}$$

Qualitatively, higher level of malignancy (larger ΔB) will generate higher fluctuation photoacoustic signals, leading to larger F_1 and F_2 than that of lower level of malignancy (smaller ΔB).

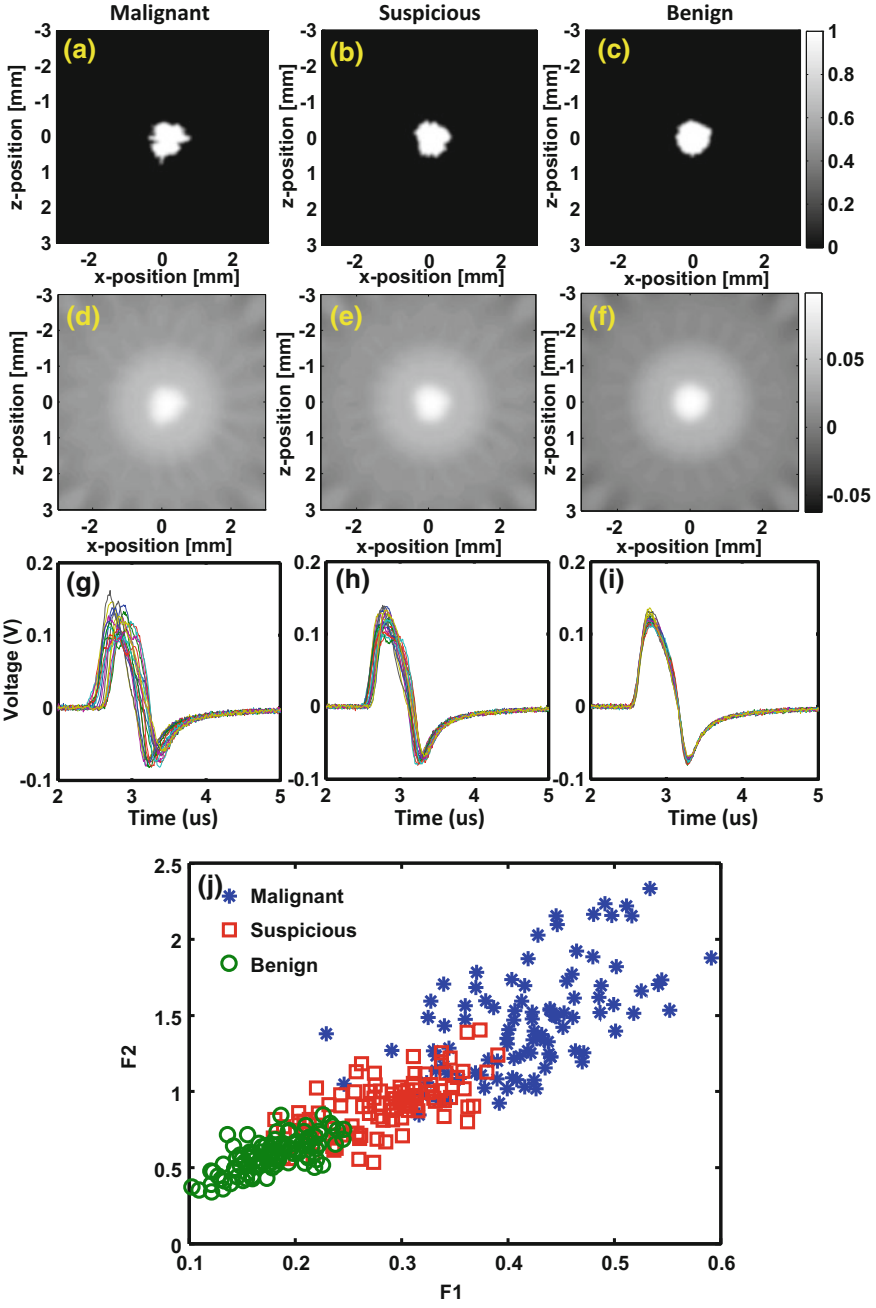

Fig. 3.21 **a**–**c** The numerical phantom of malignant, suspicious and benign tumors. **d**–**f** The time-reversal reconstructed images and **g**–**i** the original photoacoustic signals of 20 sensors. **j** Classification results with 100 training samples for each type of tumor

3.4.3 Simulation Results

3.4.3.1 Case 1: Full Field-of-View with 20 Sensors

In the first case, the numerical simulation is based on the setup in Fig. 3.20 with full field-of-view detection. A typical numerical phantoms of malignant, suspicious and benign tumors are shown in Fig. 3.21a–c with different levels of shape irregularity. The reconstructed photoacoustic images based on time-reversal algorithm are shown in Fig. 3.21d–f, where three kinds of tumors don't show significant difference between each other. An accurate diagnosis is challenging from these images, which may heavily rely on the clinician's experience. On the other hand, the time-domain photoacoustic signals of the 20 sensors are showing obvious difference for the three kinds of tumors, which are shown in Fig. 3.21g–i. It is showing that the useful information to classify these tumors is within the original photoacoustic signals, but is lost after image reconstruction. To verify the tumor classification approach statistically, 100 training examples for each tumor type are simulated for feature extraction. In Fig. 3.21j, these three types of tumors are well differentiated by applying the simple features F_1 and F_2. Malignant and benign tumors are classified with 100% accuracy after applying the linear discriminant analysis (LDA).

3.4.3.2 Case 2: Half Field-of-View with 10 Sensors

In the second case, the numerical simulation setup is based on half field-of-view detection with 10 sensors in Fig. 3.22, which is the common case for real

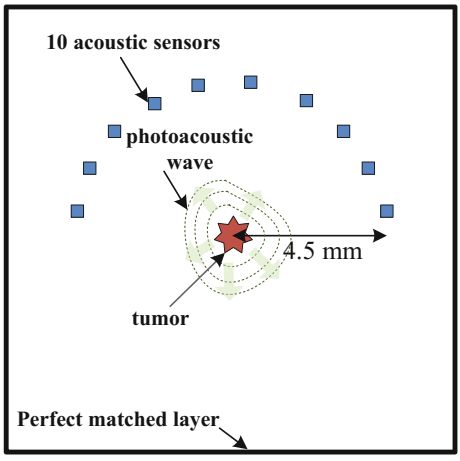

Fig. 3.22 Half field-of-view simulation geometry with 10 acoustic sensors

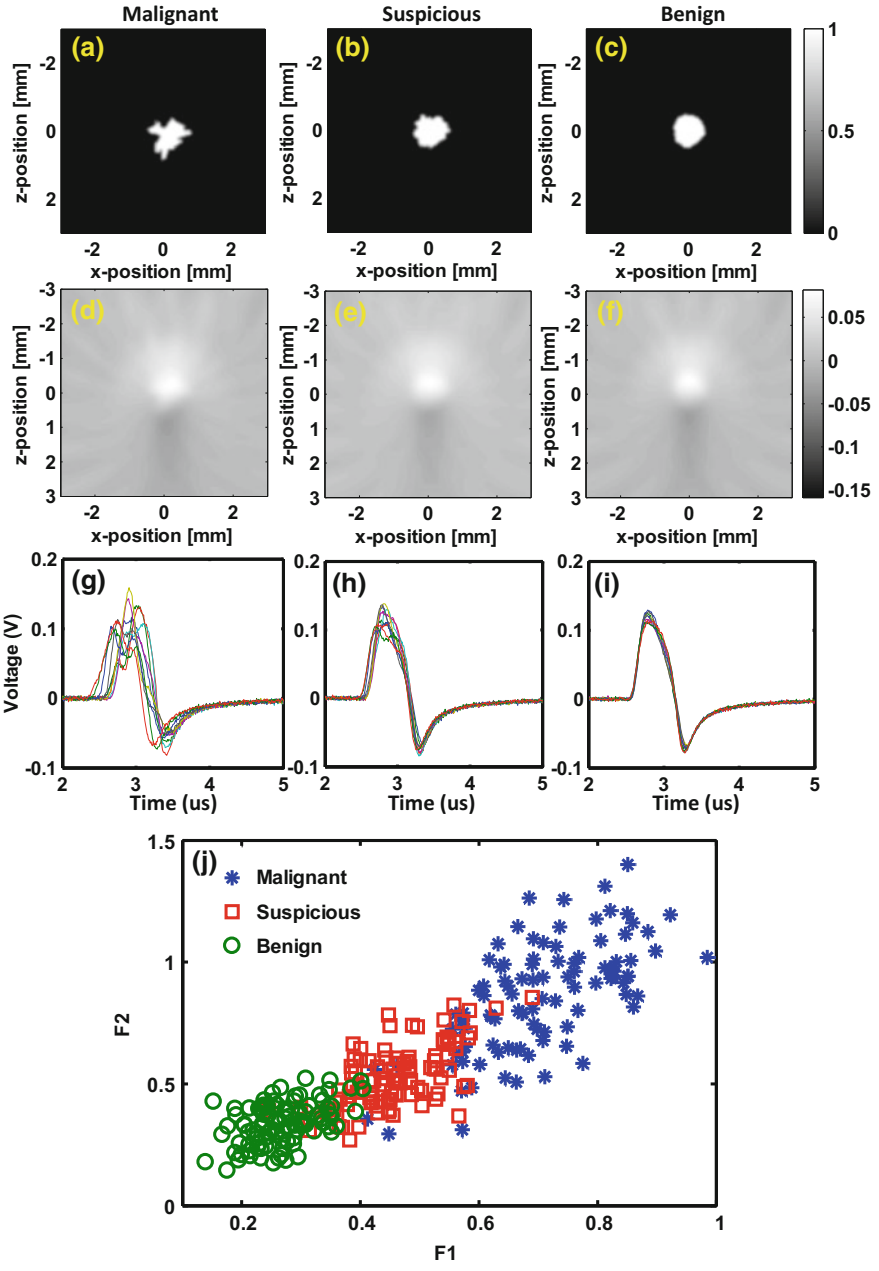

Fig. 3.23 The numerical phantom of malignant, suspicious and benign tumors. **d–f** The time-reversal reconstructed images and **g–i** the original photoacoustic signals of 10 sensors. **j** Classification results with 100 training samples for each type of tumor

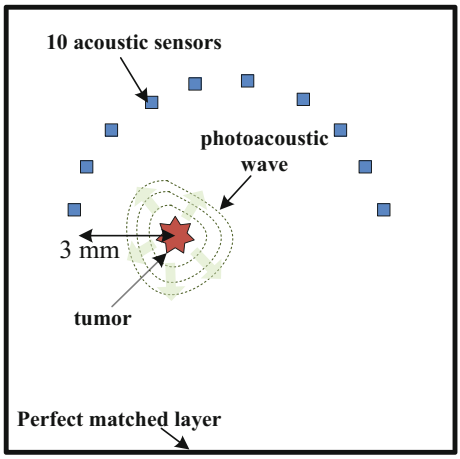

Fig. 3.24 Half field-of-view simulation geometry with non-centred tumor location

applications, where the full field-of-view detection is normally impossible. The tumor is still centred with 4.5 mm diameter.

The numerical simulation results are shown in Fig. 3.23a–i. Again it is showing that the time-reversal reconstructed images don't have much difference (Fig. 3.23d–f) between the three types of tumors, while the original photoacoustic signals from the 10 sensors have obviously different variation properties (Fig. 3.23g–i). After applying the proposed classification approach to 100 training samples for each type, malignant and benign tumors are successfully differentiated with 98% accuracy as shown in Fig. 3.23j.

3.4.3.3 Case 3: Non-centred Tumor Classification

In the third case, the system setup is similar with the second case, except the tumor location. In this case, the tumor is located off the center with 3 mm distance to the left side and 6 mm to the right side as shown in Fig. 3.24.

The numerical simulation results are shown in Fig. 3.25a–i. Again it is showing that the time-reversal reconstructed images don't have much difference (Fig. 3.25d–f) between the three types of tumors, while the original photoacoustic signals from the 10 sensors have obviously different variation properties (Fig. 3.25g–i). After applying the proposed classification approach to 100 training samples for each type, malignant and benign tumors are successfully differentiated with 96% accuracy as shown in Fig. 3.25j.

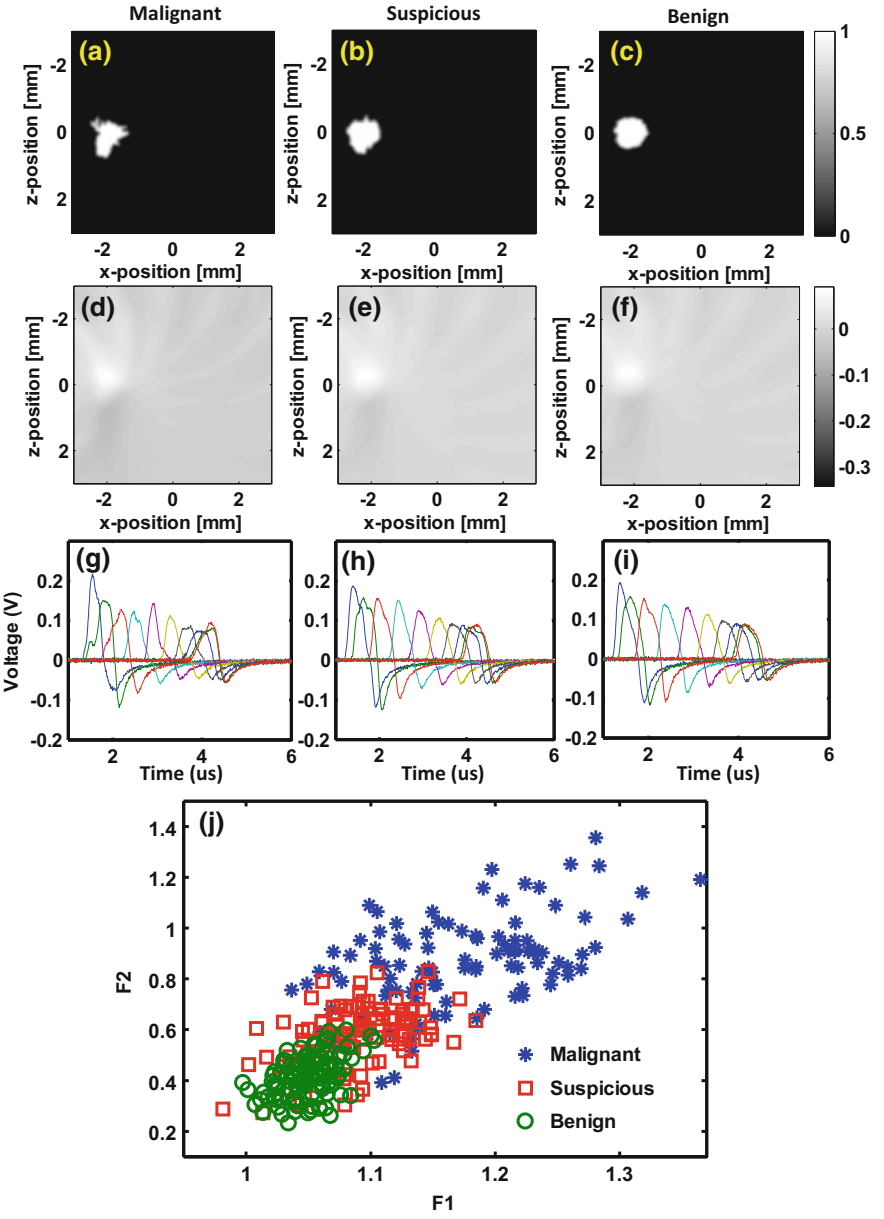

Fig. 3.25 **a**–**c** The numerical phantom of malignant, suspicious and benign tumors. **d**–**f** The time-reversal reconstructed images and **g**–**i** the original photoacoustic signals of 10 sensors. **j** Classification results with 100 training samples for each type of tumor

3.4.4 Conclusion

In this section, a simple classification algorithm is proposed to characterize different tumors with different levels of malignancy. By analyzing the original photoacoustic signals from multistatic sensors rather than the reconstructed images, it provides more reliable and accurate diagnosis results in the numerical simulation. In the future work, more advanced algorithm, such as support vector machine, could be explored for higher reliability.

References

1. Gao F, Zheng YJ (2012) A correlated microwave-acoustic imaging method for early-stage cancer detection. In: 2012 annual international conference of the IEEE engineering in medicine and biology society (EMBC), pp 480–483
2. Gabriel S, Lau RW, Gabriel C (1996) The dielectric properties of biological tissues. 3. Parametric models for the dielectric spectrum of tissues. Phys Med Biol 41:2271–2293
3. Lazebnik M, McCartney L, Popovic D, Watkins CB, Lindstrom MJ, Harter J et al (2007) A large-scale study of the ultrawideband microwave dielectric properties of normal breast tissue obtained from reduction surgeries. Phys Med Biol 52:2637–2656
4. Bond EJ, Li X, Hagness SC, Van Veen BD (2003) Microwave imaging via space-time beamforming for early detection of breast cancer. IEEE Trans Antennas Propag 51:1690–1705
5. Xie Y, Guo B, Xu LZ, Li J, Stoica P (2006) Multistatic adaptive microwave imaging for early breast cancer detection. IEEE Trans Biomed Eng 53:1647–1657
6. Kruger RA, Kopecky KK, Aisen AM, Reinecke DR, Kruger GA, Kiser WL (1999) Thermoacoustic CT with radio waves: a medical imaging paradigm. Radiology 211:275–278
7. Xu MH, Xu Y, Wang LHV (2003) Time-domain reconstruction-algorithms and numerical simulations for thermoacoustic tomography in various geometries. IEEE Trans Biomed Eng 50:1086–1099
8. Kirshin E, Oreshkin B, Zhu KG, Popovic M, Coates M (2011) Fusing microwave radar and microwave-induced thermoacoustics for breast cancer detection. In: 2011 8th IEEE international symposium on biomedical imaging: from nano to macro, pp 113–116
9. Ali MA, Moghaddam M (2010) 3D nonlinear super-resolution microwave inversion technique using time-domain data. IEEE Trans Antennas Propag 58:2327–2336
10. Diao SX, Zheng YJ (2008) An ultra low power and high efficiency UWB transmitter for WPAN applications. In: Esscirc 2008: proceedings of the 34th European solid-state circuits conference, pp 334–337
11. Gao F, Zheng Y (2012) A correlated microwave-acoustic imaging method for early-stage cancer detection. Conf Proc IEEE Eng Med Biol Soc 2012:480–483
12. Gao F, Peng QW, Feng XH, Gao B, Zheng YJ (2016) Single-wavelength blood oxygen saturation sensing with combined optical absorption and scattering. IEEE Sens J 16:1943–1948
13. Kneipp K, Wang Y, Kneipp H, Perelman LT, Itzkan I, Dasari R et al (1997) Single molecule detection using surface-enhanced Raman scattering (SERS). Phys Rev Lett 78:1667–1670
14. Nie SM, Emery SR (1997) Probing single molecules and single nanoparticles by surface-enhanced Raman scattering. Science 275:1102–1106

15. Rao AM, Richter E, Bandow S, Chase B, Eklund PC, Williams KA et al (1997) Diameter-selective Raman scattering from vibrational modes in carbon nanotubes. Science 275:187–191
16. Gao F, Ong YH, Li G, Feng X, Liu Q, Zheng Y (2015) Fast photoacoustic-guided depth-resolved Raman spectroscopy: a feasibility study. Opt Lett 40:3568–3571, 2015/08/01
17. Yakovlev VV, Zhang HF, Noojin GD, Denton ML, Thomas RJ, Scully MO (2010) Stimulated Raman photoacoustic imaging. Proc Natl Acad Sci USA 107:20335–20339
18. Davis SK, Van Veen BD, Hagness SC, Kelcz F (2008) Breast tumor characterization based on ultrawideband microwave backscatter. IEEE Trans Biomed Eng 55:237–246
19. Heijblom M, Piras D, Xia W, van Hespen JCG, Klaase JM, van den Engh FM et al (2012) Visualizing breast cancer using the Twente photoacoustic mammoscope: what do we learn from twelve new patient measurements? Opt Express 20:11582–11597
20. Wang SH, Tao C, Wang XD, Liu XJ (2013) Quantitative detection of stochastic microstructure in turbid media by photoacoustic spectral matching. Appl Phys Lett 102
21. Treeby BE, Cox BT (2010) k-wave: MATLAB toolbox for the simulation and reconstruction of photoacoustic wave fields. J Biomed Opt 15
22. Treeby BE, Jaros J, Rendell AP, Cox BT (2012) Modeling nonlinear ultrasound propagation in heterogeneous media with power law absorption using a k-space pseudospectral method. J Acoust Soc Am 131:4324–4336

Chapter 4
Multi-wave EM-Acoustic Systems

In this chapter, several EM-Acoustic systems for biomedical sensing and imaging will be introduced. In Sect. 4.1, a photoacoustic microscopy system is designed and implemented for 3D imaging, which has been proved on phantom study and will be used for ex vivo and in vivo experiments. In Sect. 4.2, a multi-channel microwave-acoustic imaging system is designed, together with a multi-channel photoacoustic receiver system including a linear-array ultrasound probe and multi-channel data acquisition card. In Sect. 4.3, a miniaturized photoacoustic receiver is designed, prototyped and demonstrated with dramatically reduced compact size in palm.

4.1 NTU Photoacoustic Microscopy System for 3D Imaging

In this section, a prototype of photoacoustic microscopy system is designed, developed and tested using phantom. The overview of the photoacoustic microscopy system will be introduced, followed by the detailed specifications, operation procedure, and an initial phantom experiment to prove the functionality of the system.

4.1.1 System Overview

The system diagram of the photoacoustic microscopy is shown in Fig. 4.1. It includes a computer to synchronize the whole system and perform the image reconstruction; a function generator to trigger the OPO laser firing and oscilloscope data recording; a 3D X/Y/Z motor system to scan the sample along with the water tank; and a set of optical components (ND filter, ConL: convex lens, FC: fibre coupler; MMF: multi-mode fibre) to guide the laser light to focus on the sample.

F. Gao, *Multi-wave Electromagnetic-Acoustic Sensing and Imaging*,
Springer Theses, DOI 10.1007/978-981-10-3716-0_4

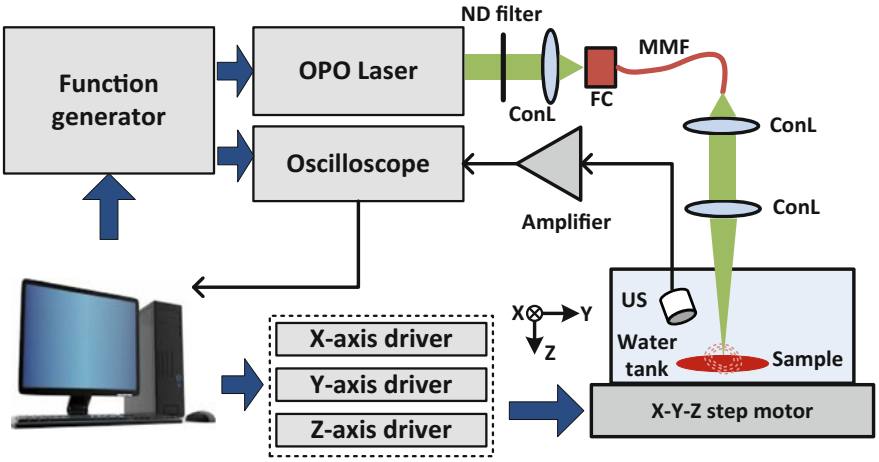

Fig. 4.1 The system diagram of the photoacoustic microscopy system

With 2D raster scanning, a 3D image could be reconstructed after bandpass filtering and Hilbert transformation to extract the envelope of the PA signals.

The custom-designed software is developed based on C++ programming language using Microsoft Visual Studio 2012. The GUI of the software is shown below (Fig. 4.2):

The function of each part in the software is listed below:

Communication: To connect the motor and function generator with PC through series port.
Enable And Disable: To turn on/off the step motor; reset the system if alarm.
Monitor: To show the current position of the scanner.
Homing: To reset the motors moving to the homing positions.
Motion Profile: To set the moving velocity; manually move the scanner for adjustment.

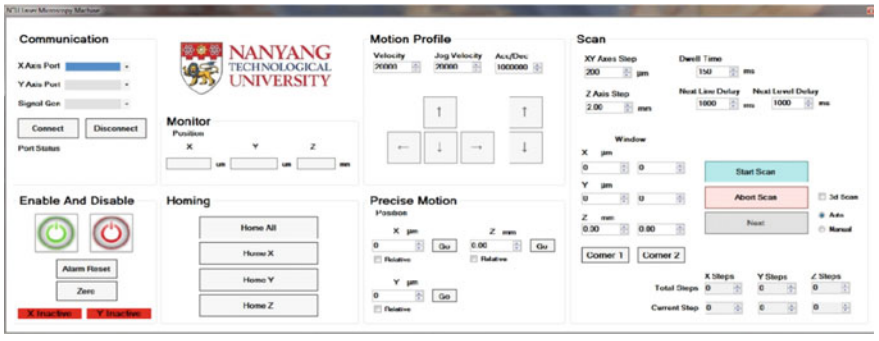

Fig. 4.2 The GUI of the photoacoustic microscopy system

Precise Motion: To move the scanner to accurate position precisely.
Scan: To set the scan step size, delay time, starting and stopping positions; To start and stop scanning in 2D or 3D; To monitor the total scan steps and current step.

4.1.2 System Specifications

The detailed system specification is summarized in the Table 4.1, including the state-of-are photoacoustic microscopy system specification, the limitation of current version, and the potential approaches to improve the system.

4.1.3 System Operation Procedure

(1) Turn on the power of the photoacoustic microscopy system, wait for 15 min to warm up the laser for stable output energy.
(2) Prepare the sample and fix the water tank on the scanner, adjust the laser focusing and ultrasound detection angle to maximize the sensitivity.
(3) Set the scanning start point and end point by manually moving the scanner to confirm the sample are fully covered, record the scan steps.
(4) Set the oscilloscope to record the data for each triggering.
(5) Start the scanning, the oscilloscope will automatically record the PA signals and save as .trc files in binary format.
(6) Download the recorded data from the oscilloscope to PC, perform the image reconstruction in MATLAB.

4.1.4 Photoacoustic Imaging in 3D: A Phantom Study

To prove the feasibility of the 3D photoacoustic microscopy system (Fig. 4.3a), a simple phantom experiment is conducted using a crossed black lines (Fig. 4.3b). The reconstructed image in 3D is shown in Fig. 4.3c, where the two crossed lines are shown clearly. To further optimize the system for ex vivo and in vivo experiments, further system upgrade is needed, such as optical-acoustic confocal design, water tank design, scanning speed increase.

Table 4.1 The specifications of photoacoustic microscopy system

System spec.	Our system	State-of-art	Current limitation	Improvement approach
Resolution	0.5 mm	<10 μm	1. Optical focusing 2. Fibre diameter (~0.5 mm) 3. Ultrasound transducer frequency (<5 MHz)	1. High NA objective lens 2. Single-mode fiber (<10 μm) 3. High frequency transducer (>30 MHz)
Imaging speed	50 Hz	>1 kHz	Repetition rate of laser	Higher repetition pulse laser (lower pulse energy)
Sensitivity	Enough	High	1. Laser and ultrasound not exactly confocol 2. Instrumentation noise	1. Custom designed laser-ultrasound confocol head. 2. Low-noise amplifier is preferred
Wavelength	Tuneable	Tuneable	Good enough	N.A.
Pulse width	1.8 ns	<10 ns	Good enough	N.A.
Pulse energy	~1 mJ	<1 μJ	1. Enough for large-scale imaging 2. Too high for high resolution PA microscopy	1. To achieve maximum energy within safety requirement (20 mJ/cm^2) 2. Use ND filter to tune the energy
Ultrasound frequency	1, 2.5, 5, 10 MHz	Up to 50 MHz	Low frequency, small aperture	Higher frequency for higher axis resolution High aperture for high transverse resolution
Water tank			Not so stable, not ready for in vivo study	A custom designed water tank is need for imaging in vivo animal to make animal outside the water
Sensor head			Separate alignment; not exact confocal	Confocol and co-axis designed sensor head
Scanning range	>20 cm × 20 cm	<5 mm × 5 mm	Large enough	N.A.
Scanning step	Tuneable, 1 cm–1 μm	1 μm	Good enough	N.A.
Data recording			Oscilloscope, bulky and slow data transfer	A high-speed DAQ card is preferred for compact integration

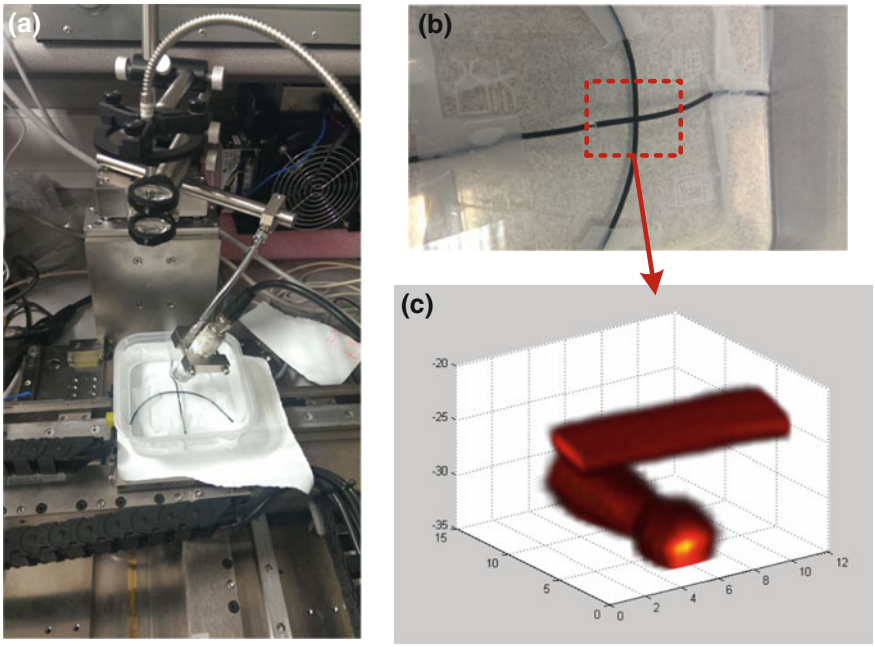

Fig. 4.3 **a** The photograph of the photoacoustic microscopy system. **b** The crossed black line phantom. **c** The reconstructed image in 3D with resolution of 0.5 mm

4.2 Multi-channel EM-Acoustic Imaging System

In this section, the multi-channel EM-Acoustic imaging system including microwave-acoustic and photoacoustic imaging, is designed to receive the PA signals in parallel for potential real-time imaging.

4.2.1 Multi-channel Microwave-Acoustic Imaging System Design

To generate the microwave UWB signal, a circuit board is designed on PCB level, shown in Fig. 4.4. This board mainly include two parts: UWB source and switch bank. UWB source block is able to generate two kinds of microwave pulse signals: modulated pulse and monocycle pulse, both of which will be tested in the experiment. The switch band is employed to switch the antenna array alternately connected with UWB source, which is necessary for image reconstruction. A low frequency oscillator is also built on board for microwave-induced thermoacoustic

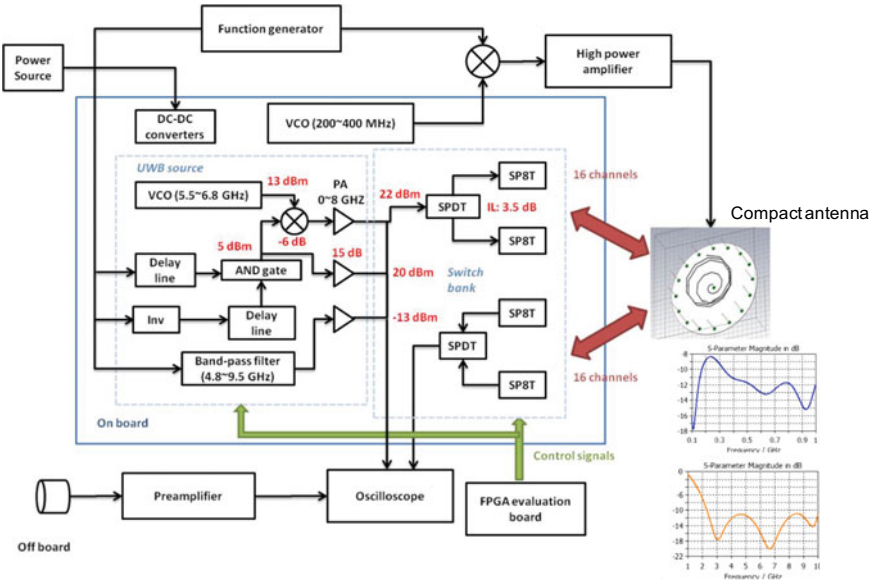

Fig. 4.4 Microwave transmitter board design

signal generation. Off the board, FPGA is used to control the operation of chips on board, both scattering microwave signal and induced thermoacoustic signal are recorded by oscilloscope for CMAI imaging. A compact antenna array is custom-designed with high radiation efficiency in biological environment shown in the S11 graph. PCB design and layout is shown in Fig. 4.5, which will be sent for fabrication in the future development.

4.2.2 Multi-channel Photoacoustic Imaging Prototyping

The system diagram of the multi-channel photoacoustic imaging is shown in Fig. 4.6a. It includes a DC power to power up the 8-channel ADC card (65 MSPS, 12 bits, AFE5809, TI) and high speed data capture card (TSW1400, TI). These two cards will simultaneously trigger the function generator (33250A, Agilent) and laser firing, and record the PA signal from a phase-array ultrasound probe (128 elements, Doppler Inc.). A typical PA signal from one of the channels is shown in Fig. 4.6b. Another solution to receive multi-channel PA signals is based on the Sonix RP ultrasound scanner, which can record the raw PA signals for further image reconstruction.

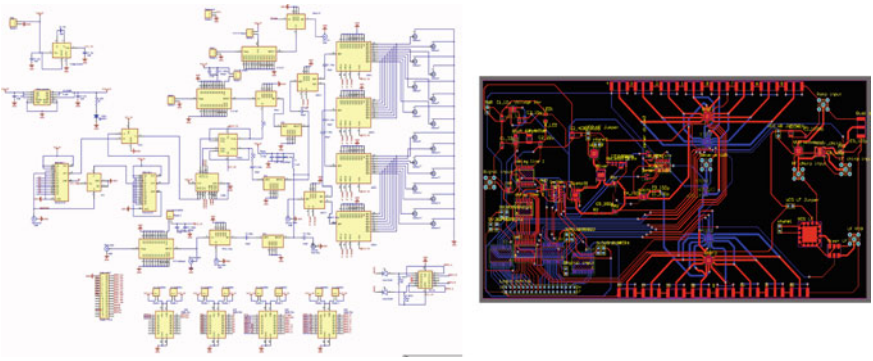

Fig. 4.5 PCB design of microwave transmitter board

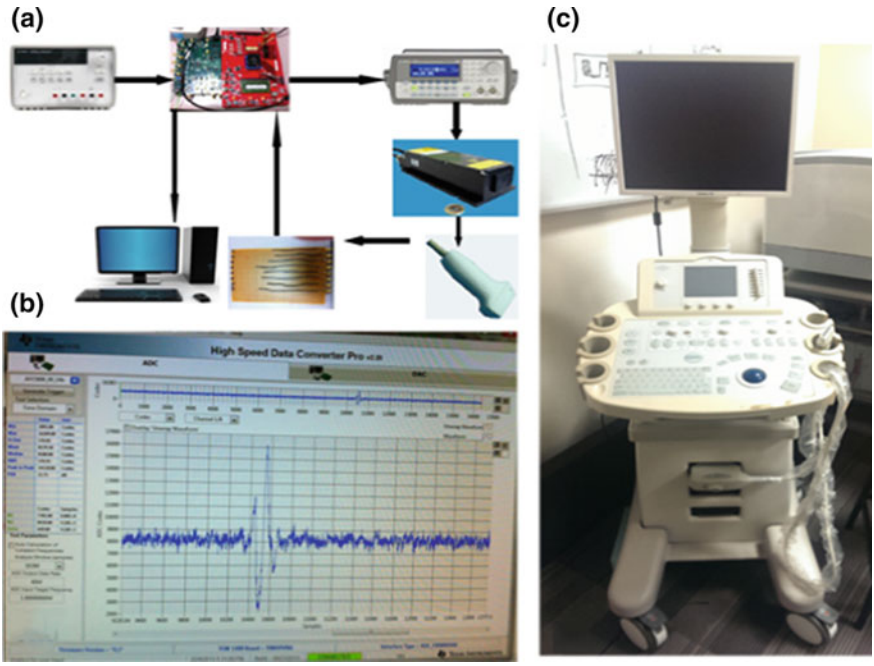

Fig. 4.6 **a** The multi-channel photoacoustic imaging system diagram. **b** A typical detected photoacoustic signal from one of the channels. **c** The Sonix RP ultrasound system to collect the raw photoacoustic signals

4.3 Miniaturized Photoacoustic Receiver in Palm

Photoacoustic sensing and imaging techniques have experienced tremendous research progress, ranging from fundamental physics and methodologies to various biomedical and clinical applications in recent years. However, the state-of-art photoacoustic systems suffer high cost and bulky size, which hinders its applications for low-cost and portable diagnostics. In this section, we will introduce design and prototyping of a palm-size photoacoustic sensor, which may be the world's smallest and cheapest one dedicated for photoacoustic sensing applications, e.g. oxygen saturation, temperature, etc. By converting the high-frequency photoacoustic pulse signal to low-frequency photoacoustic DC signal through rectifier circuit, the proposed photoacoustic receiver utilizes much lower cost ($\times$100 times) and smaller size ($\times$20 times) components, than the conventional high-speed data acquisition card interfaced with computer. Initial testing is demonstrated to show its feasibility for photoacoustic sensing applications. The results of this section have been submitted to *IEEE Trans. on Biomedical Circuits and Systems*.

4.3.1 Introduction

Photoacoustic sensing and imaging techniques have attracted increasing research interest for biomedical applications in recent years, which cover fundamental physics, novel methodologies, and promising clinical applications. On the other hand, several companies (Endra, iThera Medical, Visual Sonics) have also initiated the commercialization of photoacoustic systems for small animal experiments. However, the state-of-art photoacoustic systems developed by both academic community and industrial companies are suffering high cost and bulky size, limiting their applications to lab use and hospital installation only. The development of a portable and low-cost photoacoustic sensor is still an untapped area for point-of-care and on-site patient diagnostics applications. These applications require much lower cost and smaller device size than the existing photoacoustic systems to push the photoacoustic sensing device to enter the small clinics and even homecare. In this section, we will report the first design and prototyping of a portable photoacoustic receiver in palm size, which could achieve >100 times lower cost and >20 times smaller size compared with the conventional photoacoustic systems. The design details and initial testing results will be demonstrated in the following sections.

4.3.2 System Design and Development

As shown in Fig. 4.7a, a typical photoacoustic sensing/imaging system mainly includes two parts: the laser illumination part and ultrasound detection part. This

paper is focusing on the miniaturization of the ultrasound detection part, which includes amplifier to amplify the weak photoacoustic signal, high-speed data acquisition (DAQ) card to sample the photoacoustic pulse signal into digital domain, and personal computer to process the data for display. To miniaturize the ultrasound detection system, the key point is to identify the bottleneck of the current photoacoustic systems.

It is well known that photoacoustic signal is a wideband pulse signal with central frequency ranging from several hundreds of kHz to several tens of MHz depending on different applications. For example, a 50 MHz photoacoustic signal requires a DAQ card with at least 100 MHz sampling rate according to Nyquist criterion, or even higher sampling rate for better signal fidelity. To handle the high sampling rate, a computer is required to interface with the DAQ card, where a low cost, low speed microprocessor is unavailable. Therefore, release of the high-speed sampling requirement is the most important and sufficient way to develop a portable and low-cost photoacoustic sensor.

The prototype of the proposed photoacoustic sensor in palm is shown in Fig. 4.7b, including photoacoustic signal input port, amplifier, rectifier, microprocessor board and LCD screen. The working principle of the device is shown in Fig. 4.8. Firstly, the non-inverting amplifier circuit amplifies the original pulse photoacoustic signal with gain of 100 (*Design tip*: The operational amplifier (LT1226, Linear Technology) should have enough gain-bandwidth (>500 MHz); Resistor value R1 and R2 are selected properly to achieve the gain required based

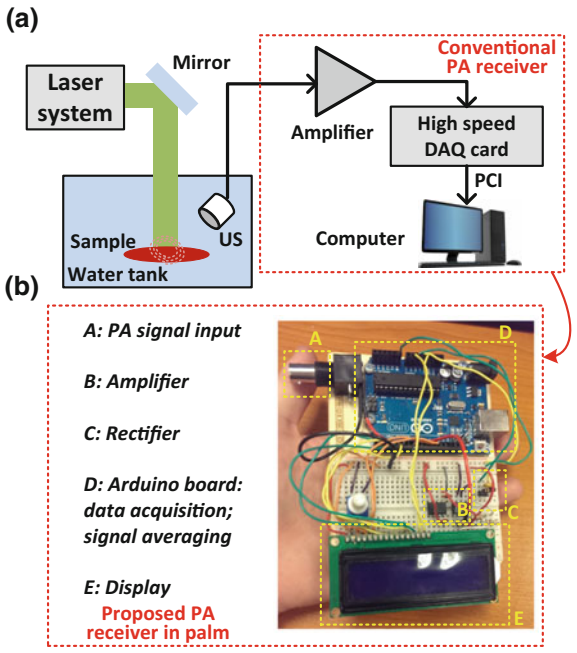

Fig. 4.7 **a** Diagram of the conventional photoacoustic sensing/imaging system. **b** Photograph of the proposed photoacoustic sensor in palm. *US* ultrasound transducer; *DAQ* data acquisition; *PCI* peripheral component interconnect; *PA* photoacoustic

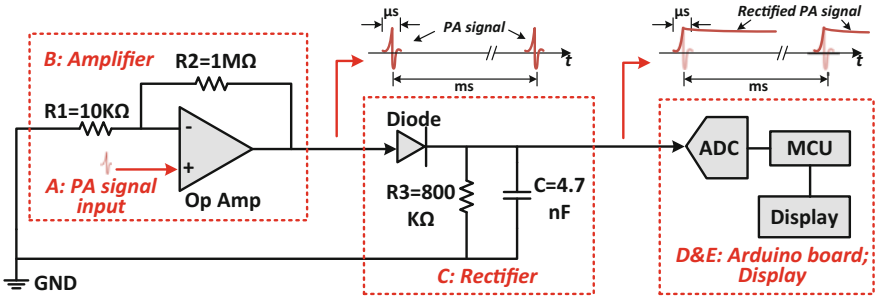

Fig. 4.8 The circuit/system structure of the proposed photoacoustic sensor in palm. *Op Amp* operational amplifier; *ADC* analog-to-digital converter; *MCU* microcontroller unit

on gain = 1 + $R2/R1$). Secondly, the photoacoustic pulse signal is rectified by the half-wave rectifier circuit to be photoacoustic DC signal (*Design tip*: R3 and C are selected properly to guarantee fast response to photoacoustic pulse signal (smaller capacitor) and slow current discharging to maintain photoacoustic DC signal (relaxation time $\tau = R3 \times C \approx$ ms)). Lastly, the rectified photoacoustic DC signal is sampled by the low-speed analog-to-digital converter (ADC) with 10 kHz sampling rate, and processed by the low-cost microprocessor board (Arduino Uno). It is worth noting that the key difference between the proposed palm-size sensor and the conventional photoacoustic system is the usage of rectifier circuit, which converts the high-frequency photoacoustic pulse signal to low-frequency photoacoustic DC signal, enabling the low-speed low-cost acquisition system design. To clearly identify the merit of the proposed palm-size photoacoustic sensor, a comparison table is shown in Table 4.2.

4.3.3 Measurement Results

To prove the functionality of the palm-size photoacoustic sensor, an initial testing was conducted by generating the standard pulse signal (Fig. 4.9a) from function generator (33250A, Agilent) as input to the device. The rectified photoacoustic DC signal was recorded and displayed by an oscilloscope (WaveRunner 640Zi, LeCroy) in Fig. 4.9b. It is showing that the input pulse signal is rectified as a DC signal indicated by the arrow, which could be sampled by low-speed ADC of the palm-size photoacoustic sensor for data averaging and display. Through sweeping the amplitude of the input pulse signal, the recorded photoacoustic DC signal from the palm-size sensor is ploted in Fig. 4.9c as red circled line after proper normalization. As expected, the amplitude from the palm-size photoacoustic sensor is proportional to the amplitude of the input pulse in a non-linear manner, compared with the blue reference line (Output:Input = 1:1). This is caused by the non-linearity of the rectifier circuit components including diode and capacitor. This non-linear

Table 4.2 Comparison between conventional photoacoustic system and palm-size sensor

Specification	Conventional photoacoustic system	Proposed palm-size photoacoustic sensor
Components	Amplifier; high-speed DAQ card; computer	Amplifier; low-speed low-cost MCU board; LCD screen
Sampling rate	>100 MHz	10 kHz
Cost	>5000 USD	<50 USD (*×100 times cheaper*)
Size	Bulky benchtop size	Small palm size (*×20 times smaller*)
Portability	Inconvenient to move	Very convenient to move
Function	Photoacoustic sensing and imaging to almost all the biomedical applications for lab use and hospital installation	Fast, low-cost, real-time, point-of-care photoacoustic sensing applications (no image required) for on-site diagnostics
Application	E.g. whole-body animal imaging, breast imaging, brain imaging, photoacoustic microscopy in 3D	E.g. real-time SO_2, temperature, glucose, lipid-rich plaque monitoring, cytometry, photoacoustic microscopy in 2D (no depth)

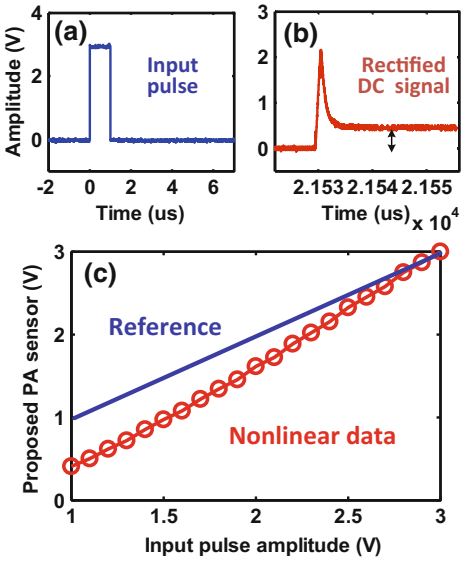

Fig. 4.9 **a** The input pulse signal from the function generator. **b** The rectified DC signal recorded by the oscilloscope. **c** The plot of the amplitude detected by the proposed palm-size sensor versus the increasing input pulse amplitude. *Blue reference line*: Output:Input = 1:1; *Red circled line*: Nonlinear data from the sensor

behavior could be easily calibrated by compensating the detected signal of palm-size sensor towards the reference line.

Next, a phantom experiment was conducted to test the feasibility of the proposed palm-size device for real photoacoustic signal detection. The experimental setup is similar with that in Fig. 4.7a left side. An OPO laser system (Opolette 355, OPOTEK Inc.) was employed to generate pulsed laser light with 532 nm

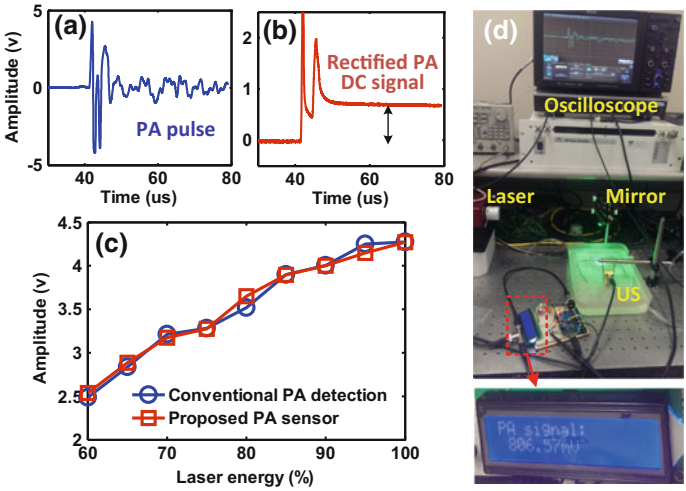

Fig. 4.10 **a** The original photoacoustic pulse signal. **b** The rectified photoacoustic DC signal. **c** The plot of the signal amplitudes detected by the oscilloscope (*blue circle line*) and the proposed palm-size sensor (*red square line*) versus the increasing laser pulse energy. **d** Photograph of the proposed palm-size sensor in operation

wavelength and 7 ns pulse width. The laser beam was guided by a mirror to illuminate the black line phantom, which was immersed in water for optimum optical and acoustic coupling. The ultrasound transducer (1 MHz, 60% fractional bandwidth, V303-SU, Olympus) was hold by a clamp and also immersed in the water tank. The original photoacoustic signal and the rectified photoacoustic DC signal recorded by the oscilloscope are shown in Fig. 4.10a, b. Through sweeping the laser energy, the original photoacoustic signal detected by oscilloscope and its rectified DC signal detected by the proposed palm-size sensor after normalization are in good agreement with <5% error shown in Fig. 4.10c, proving its ability for reliable photoacoustic signal monitoring. The photograph of the experimental setup is shown in Fig. 4.10d, where the proposed photoacoustic sensor is in operation.

4.3.4 Discussion and Conclusion

In this section, the first prototype of the palm-size photoacoustic sensor is reported with dramatically lower cost (×100 times) and smaller size (×20 times). It is demonstrated to monitor the photoacoustic signal reliably compared with the original photoacoustic signal detected by the oscilloscope. It inspires the possibility to develop a portable low cost photoacoustic sensor for point-of-care and affordable

diagnostics in small clinics, especially in developing countries. In the future work, the laser part will also be integrated in the portable photoacoustic sensor by employing low-cost low-power laser diode. The photoacoustic detection part will be further integrated by standard CMOS (Complementary metal–oxide–semiconductor) microelectronics technology and integrated circuits design.

Chapter 5
Conclusion and Future Work

This chapter will conclude the thesis and shed light on the possible improvement and update of the multi-wave imaging techniques for future work.

5.1 Conclusion

This thesis conducted a comprehensive study of the emerging multi-wave sensing and imaging techniques covering fundamental methods, clinical applications and system development:

Fundamental methods: In Sect. 2.1, it introduces an electrical circuit modeling approach of microwave-acoustic interaction with biological tissue for quantitative analysis and bio-circuit co-simulation. In Sect. 2.2, a new concept "phasoscopy" is introduced correlating EM scattering and absorption to achieve super sensitivity and contrast for biological tissue characterization and imaging. In Sects. 2.3 and 2.4, EM-acoustic resonance and oscillation effect are observed, modelled and utilized for tissue characterization and imaging, fusing optical absorption and mechanical resonance. In Sect. 2.5, the coherent correlation between EM-acoustic and ultrasound is explored for super-contrast imaging. In Sect. 2.6, the micro-Doppler EM-acoustic effect is predicted and observed experimentally, which could potentially achieve sensitive EM-Acoustic detection.

Biomedical applications: In Sect. 3.1, a correlated microwave-acoustic imaging approach is proposed by fusing scattered microwave and thermoacoustic image to deliver higher image contrast for early-stage breast cancer detection, which is proved with numerical simulation results. In Sect. 3.2, a novel single-wavelength approach is proposed to detect the blood oxygen saturation (SO_2), where both scattered optical wave and photoacoustic wave are collected and correlated. Phantom studies are performed to validate its feasibility. In Sect. 3.3, a photoacoustic-guided depth-resolved Raman spectroscopy approach is proposed for skin cancer diagnosis, which is experimentally validated on multi-layer phantom. In

F. Gao, *Multi-wave Electromagnetic-Acoustic Sensing and Imaging*,
Springer Theses, DOI 10.1007/978-981-10-3716-0_5

Sect. 3.4, a multistatic photoacoustic classification approach is proposed to characterize malignant and benign tumors, which is challenging for conventional photoacoustic tomography for deep tissue imaging.

System development: In Sect. 4.1, a photoacoustic microscopy system is designed and implemented for 3D imaging, which has been proved on phantom study and will be used for ex vivo and in vivo experiments. In Sect. 4.2, a multi-channel microwave-acoustic imaging system is designed, together with a multi-channel photoacoustic receiver system including a linear-array ultrasound probe and multi-channel data acquisition card. In Sect. 4.3, a miniaturized photoacoustic receiver is designed, prototyped and demonstrated with dramatically reduced compact size in palm for photoacoustic sensing applications.

In summary, this thesis introduced some interesting concepts, which could potentially solve some important biomedical problems and inspire in-depth thought to develop an advanced multi-wave EM-Acoustic imaging system.

5.2 Future Work

Although some progress has been achieved in this thesis, there is still much space to be improved for a better multi-wave imaging system:

Fundamental methods: In this part, a deeper exploration and comprehensive study of the optic-acoustic interaction is required to inspire new imaging modalities in the future work. For example, the intrinsic correlation between photoacoustic generation and Raman/Fluorescence scattering may introduce advanced imaging techniques that combining both merits of Photoacoustic's deep peneration and Raman spectroscopy's molecular specificity. Another example is the intelligent combination of photoacoustic imaging with elastography, which is potentially able to provide dual-contrast deep tissue imaging for challenging clinical applications.

Biomedical applications: In this part, more interesting clinical applications could be explored. To go beyond the phantom and some simple ex vivo study in this thesis, in vivo animal testing and even human trials are expected in the future work to further validate the potentials of the proposed techniques for real clinical applications. For example, these applications could be, but not limited to, SO_2/temperature/glucose monitoring, early-stage cancer detection, brain imaging, early stroke/shock alarming.

System development: In this part, more advanced and integrated multi-wave imaging systems are required for commercialization in the future work. For example, a portable, low complexity and cost photoacoustic imaging device is highly desired to extend its utility to small clinics and developing countries, even homecare. To achieve this, a dedicated photoacoustic imaging system integration employing advanced technologies, such as MEMS, IC design, and silicon photonics could be developed. To develop a truly compact photoacoustic imager, low-cost laser diode should be selected as the light source. To overcome the disadvantages of the laser diode, especially its low peak power, advanced high-sensitivity ultrasound

receiver is required. In addition, frequency-domain photoacoustic technique could be explored based on chirp-modulation.

As most of the works in this thesis are proof-of-concept projects, the proposed methods were tested under simplified conditions at the current stage. In the presence of tissue inhomogeneity, I believe that all the proposed methods are also applicable by including more accurate calibration and compensation steps. For example, in heterogeneous tissue, the elastic oscillation effect may be distorted and interfered by the surrounding tissue. This may induce waveform change at the receiver side. However, the acoustic inhomogeneity could be estimated and calibrated with some algorithm design and prediction. For the micro-Doppler effect, to avoid possible distortion, the biological tissue should be kept constant during the measurement, so that the micro-Doppler frequency shift can be correctly recovered without introducing speckles. To design more realistic in vitro/in vivo experiments, there are a lot of literatures in the photoacoustic research community. We will follow the standard animal model and protocol to design and test our proposed methods for potential clinical translation.

In this thesis, spatial resolution and light penetration are not critically considered under the simple phantom and experiment setup. For potential clinical values, regarding different kinds of clinical applications, the spatial resolution and penetration could be trade-off. Specifically, for surface cancer detection requiring less light penetration, such as skin cancer, finer spatial resolution could be achieved using tight optical focusing and high frequency ultrasound receiver. On the other hand, for deep cancer detection requiring deep light penetration, such as breast cancer screening, the light penetration of >5 cm is usually desired with courser resolution of millimeter range. Utilizing the improved image contrast of the proposed methods, stage 1 or 2 breast cancer could be detected potentially. Compared with the existing technologies such as mammography and ultrasound, the proposed methods are able to utilize multi-contrast mechanism, such as optical absorption and elasticity, to identify potential breast cancer at its early stage.

Author's Publications

Book Chapter

1. Yuanjin Zheng, **Fei Gao**, Zhiping Lin, "Chapter 16: Correlated Microwave Acoustic Technique for Breast Cancer detection", ***Multimodality Breast Imaging: Diagnosis and Treatment***, SPIE Press, 4 Mar., 2013.

Journal Papers

2. **Fei Gao**, Yuanjin Zheng, and Dongfang Wang, "Microwave-acoustic phasoscopy for tissue characterization," ***Applied Physics Letters*** 101, 043702 (2012).
3. **Fei Gao**, Yuanjin Zheng, Xiaohua Feng, and Claus-Dieter Ohl, "Thermoacoustic resonance effect and circuit modelling of biological tissue," ***Applied Physics Letters*** 102, 063702 (2013).
4. Xiaohua Feng, **Fei Gao**, Yuanjin Zheng, "Magnetically mediated thermoacoustic imaging toward deeper penetration," ***Applied Physics Letters*** 103, 083704 (2013).
5. **Fei Gao**, Qian Zheng, Yuanjin Zheng "Circuit Modeling and Analysis of Microwave Acoustic Interaction with Biological Tissues", ***Medical Physics***, 41, 053302 (2014).
6. **Fei Gao**, Xiaohua Feng, Yuanjin Zheng, "Coherent photoacoustic-ultrasound correlation and imaging", ***IEEE Transactions on Biomedical Engineering***, 61, 2507-2512 (2014).
7. Xiaohua Feng, **Fei Gao**, Yuanjin Zheng, "Thermally modulated photoacoustic imaging with super-paramagnetic iron oxide nanoparticles", ***Optics Letters***, 39, 3414-3417 (2014).
8. **Fei Gao**, Xiaohua Feng, Yuanjin Zheng, "Photoacoustic Phasoscopy Super-Contrast Imaging", ***Applied Physics Letters*** 104, 213701 (2014).
9. **Fei Gao**, Xiaohua Feng, Yuanjin Zheng, Claus-Dieter Ohl, "Photoacoustic resonance spectroscopy for tissue characterization", ***Journal of Biomedical Optics,*** 19(6), 067006 (2014).
10. Xiaohua Feng, **Fei Gao**, Yuanjin Zheng, "Photoacoustics Based Close-loop Control for Nanoparticle Hyperthermia", ***IEEE Transactions on Biomedical Engineering***, 62, 1728-1737 (2015).

F. Gao, *Multi-wave Electromagnetic-Acoustic Sensing and Imaging*,
Springer Theses, DOI 10.1007/978-981-10-3716-0

11. Xiaohua Feng, **Fei Gao**, Yuanjin Zheng, "Modulatable magnetically mediated thermoacoustic imaging with magnetic nanoparticles", ***Applied Physics Letters***, 106, 153702 (2015).
12. **Fei Gao**, Xiaohua Feng, Xilin Miao, Yuanjin Zheng, "Photoacoustic sensing in palm", ***X-Acoustics: Imaging and Sensing,*** to appear (2015). **(invited article)**
13. Xiaohua Feng, **Fei Gao**, Rahul Kishor and Yuanjin Zheng, "Coexisting and mixing phenomena of thermoacoustic and magnetoacoustic waves in water", ***Scientific Reports (Nature Publishing Group),*** 5, 11489 (2015).
14. **Fei Gao**, Xiaohua Feng, Yuanjin Zheng, "Photoacoustic elastic oscillation and characterization", ***Optics Express***, 40, 3568-3571 (2015).
15. **Fei Gao**, Yi Hong Ong, Gaoming Li, Xiaohua Feng, Yuanjin Zheng, Quan Liu, "Photoacoustic-guided fast depth-resolved Raman spectroscopy: a feasibility study", ***Optics Letters,*** 40, 3568-3571 (2015).
16. Xiaohua Feng, **Fei Gao**, Chenyu Xu, Gaoming Li, Yuanjin Zheng, "Self temperature regulation of photothermal therapy by laser-shared photoacoustic feedback," ***Optics Letters.,*** 40, 4492-4495 (2015).
17. **Fei Gao**, Xiaohua Feng, Yuanjin Zheng and Claus-Dieter Ohl, "Micro-Doppler photoacoustic effect and sensing by ultrasound radar", ***IEEE Journal of Selected Topics in Quantum Electronics,*** 22, 681806, 1-6 (2016).
18. **Fei Gao**[†], Qiwen Peng[†], Xiaohua Feng, Yuanjin Zheng, "Single-wavelength oxygen saturation detection fusing optical absorption and scattering properties ", ***IEEE Sensors Journal,*** 16, 1943-1948 (2016). ([†]Equal contribution)
19. **Fei Gao**, Xiaohua Feng, Yuanjin Zheng, "Advanced photoacoustic and thermoacoustic sensing and imaging beyond pulsed absorption contrast", ***Journal of Optics***, 18, 074006 (2016). **(invited review)**
20. Rahul, Kishor[†], **Fei Gao**[†], S. Sreejith, X. Feng, Y. P. Seah, Z. Wang, M. C. Stuparu, T.-T. Lim, X. Chen, and Y. Zheng, "Photoacoustic Induced Surface Acoustic Wave Sensor for Concurrent Opto-Mechanical Microfluidic Sensing of Dyes and Plasmonic Nanoparticles", ***RSC Advances***, 6, 50238-50244 (2016). (†Equal contribution)
21. Gaoming Li[†], **Fei Gao**[†], Yisheng Qiu, Xiaohua Feng, Yuanjin Zheng, "Multiple stimulated Emission fluorescence photoacoustic sensing and spectroscopy", ***Applied Physics Letters***, 109, 013701 (2016). (†Equal contribution).
22. Gaoming Li[†], **Fei Gao**[†], Xiaohua Feng, Yuanjin Zheng, "Theory analysis of stimulated Raman Photoacoustics in frequency domain: a feasibility study ", ***Journal of Applied Physics,*** 120, 083105 (2016). (†Equal contribution).
23. **Fei Gao**, Linyi Bai, Xiaohua Feng, Huijun Phoebe Tham, Ruochong Zhang, Yuanyuan Zhang, Siyu Liu, Lingzhi Zhao, Yuanjin Zheng, and Yanli Zhao, "Remarkable in vivo nonlinear photoacoustic imaging based on organic dyes", ***Small***, DOI: 10.1002/smll.201602121 (2016).
24. Ran Ding, …, **Fei Gao**, et al, "Flexible Piezoelectric Nanocomposite Generators Based on Formamidinium Lead Halide Perovskite Nanoparticles", ***Advanced Functional Materials***, doi:10.1002/adfm.201602634 (2016).

25. **Fei Gao**, Linyi Bai, Siyu Liu, Ruochong Zhang, Xiaohua Feng, Yuanjin Zheng, and Yanli Zhao, "Rationally Encapsulated Gold Nanorods Improving both Linear and Nonlinear Photoacoustic Imaging Contrast *in vivo*", ***Nanoscale***, to appear (2017).
26. **Fei Gao**, Rahul Kishor, Xiaohua Feng, Siyu Liu, Ran Ding, Ruochong Zhang and Yuanjin Zheng, "An analytical study of photoacoustic and thermoacoustic generation", ***Photoacoustics***, to appear (2017).
27. **Fei Gao**, Xiaohua Feng, Ruochong Zhang, Siyu Liu, Ran Ding, Rahul Kishor and Yuanjin Zheng, "One laser pulse generates two photoacoustic signals", ***Scientific Reports,*** to appear (2017)

Conference Papers

28. **Fei Gao**, Yuanjin Zheng, "A Correlated Microwave-Acoustic Imaging Method for Early-Stage Cancer Detection." *34th Annual International Conference of the IEEE Engineering in Medicine & Biology Society (**EMBC**)*, San Diego, CA, USA, Aug. 28-Sep. 1, 2012.
29. Chiang Liang Kok, Siek Liter, **Fei Gao**, Yuanjin Zheng, Wei Meng Lim, "An Ultra-Compact Green Bio-Regulator Dedicated for Brain Cortical Implant Using a Dynamic PSR Enhancement Technique." *34th Annual International Conference of the IEEE Engineering in Medicine & Biology Society (**EMBC**)*, San Diego, CA, USA, Aug. 28-Sep. 1, 2012.
30. **Fei Gao**, Yuanjin Zheng, Xiaohua Feng, Claus-Dieter Ohl, "Photoacoustic phasoscopy for tissue characterization", *Photonics Global Conference (**PGC**)*, Singapore, 13-16 Dec. 2012.
31. **Fei Gao**, Yuanjin Zheng, "Photo-acoustic/Microwave-acoustic phasoscopy and coherent correlation for biological tissue characterization and imaging", *Asia-Oceania Top University League on Engineering (**AOTULE**) Student Conference*, Kuala Lumpur, Malaysia, Nov. 24-25, 2012.
32. **Fei Gao**, Xiaohua Feng, Yuanjin Zheng, "Microwave-acoustic correlated imaging and circuit modelling of biological tissues", *IEEE MTT-S International Microwave Workshop Series on RF and Wireless Technologies for Biomedical and Healthcare Applications (**IMWS-Bio**)*, Singapore, Dec. 9-11, 2013. **(invited paper)**
33. Xiaohua Feng, **Fei Gao**, Yuanjin Zheng, "Magnetically mediated thermoacoustic imaging and technical considerations on its coil design", *IEEE MTT-S International Microwave Workshop Series on RF and Wireless Technologies for Biomedical and Healthcare Applications (**IMWS-Bio**)*, Singapore, Dec. 9-11, 2013.
34. **Fei Gao**, Xiaohua Feng, Yuanjin Zheng, "Photoacoustic phasoscopy super-contrast imaging correlating optical absorption and scattering", *SPIE Photonics West (**Photons Plus Ultrasound: Imaging and Sensing**),* San Francisco, California United States, Feb. 1-6, 2014.
35. Xiaohua Feng, **Fei Gao**, Yuanjin Zheng, "Magnetically mediated thermoacoustic imaging", *SPIE Photonics West (**Photons Plus Ultrasound: Imaging and Sensing**),* San Francisco, California United States, Feb. 1-6, 2014.

36. Xiaohua Feng, **Fei Gao**, Yuanjin Zheng, "Scalable magnetically mediated thermoacoustic imaging through coil tailoring", *IEEE MTT-S International Microwave Workshop Series on RF and Wireless Technologies for Biomedical and Healthcare Applications (**IMWS-Bio**)*, London, UK, Dec. 8-10, 2014.
37. Yuanjin Zheng, **Fei Gao**, Xiaohua Feng, "Electromagnetic Acoustics Sensing and Imaging for Biomedical Applications", *IEEE MTT-S International Microwave Workshop Series on RF and Wireless Technologies for Biomedical and Healthcare Applications (**IMWS-Bio**)*, London, UK, Dec. 8–10, 2014.
38. Qiwen Peng[†], **Fei Gao**[†], Xiaohua Feng, Yuanjin Zheng, "A noninvasive single wavelength monitoring of blood oxygen saturation utilizing both photoacoustics absorption and light scattering", *SPIE Photonics West (**Photons Plus Ultrasound: Imaging and Sensing**),* 2015. ([†]Equal contribution).
39. Xiaohua Feng, **Fei Gao**, Yuanjin Zheng, "A self-monitored theranostic platform based on nanoparticle hyperthermia therapy and alternating magnetic field induced thermoacoustic imaging", *SPIE Photonics West (**Photons Plus Ultrasound: Imaging and Sensing**),* 2015.

Patent

40. "The non-invasive phasoscopy photoacoustic based SO2 and glucose monitoring sensor (with temperature calibrated) from using single wavelength to multi-wavelength", ***patent filed, Singapore***.

Miscellaneous Report

41. "3D scanner for correlated microwave acoustic medical imaging", duration: 2'23`` ~ 2'50', ***VIRTUS IC Design Centre of Excellence in NTU.*** URL: http://www.virtus.eee.ntu.edu.sg/Video/Pages/default.aspx, http://www.youtube.com/watch?v=DXZbarO1DaE
42. "Photoacoustic sensing and imaging", ***VALENS Bio-Instrumentation, Devices and Signal Processing Centre in NTU,*** in filming **(invited video).**
43. Magazine report, "Microwave Acoustic Imaging for Cancer Diagnosis Research in NTU", ***In Brief, Innovation Magazine***, Num 3, Vol. 10, 2011.
44. "Multi-wave sensing and imaging: Listening to the sound of electromagnetic wave", ***EEE Annual Research Report***, NTU, 2014.
45. **Fei Gao**, "Multi-wave Photo-acoustic and Microwave-acoustic phasoscopy super-contrast sensing and imaging", *4th VIRTUS Annual Postgraduate Research Workshop*, 1-2 Oct., 2014.
46. **Fei Gao**, "Multi-wave sensing and imaging: Listening to the sound of electromagnetic wave", *VALENS Students Seminar Series VI*, 6 Nov., 2014.